Doped and multi-compound ZnO-based transparent conducting oxides for silicon thin film solar cells

Paz Carreras Seguí

Universitat de Barcelona

DEPARTAMENT DE FÍSICA APLICADA I ÒPTICA

Av. Diagonal, 645, 08028 Barcelona

Doped and multi-compound ZnO-based transparent conducting oxides for silicon thin film solar cells

Paz Carreras Seguí

Memòria presentada per optar al grau de Doctor amb menció internacional

Barcelona, Gener de 2013

Universitat de Barcelona

DEPARTAMENT DE FÍSICA APLICADA I ÒPTICA

Av. Diagonal, 645, 08028 Barcelona

Doped and multi-compound ZnO-based transparent conducting oxides for silicon thin film solar cells

Paz Carreras Seguí

Directors: Joan Bertomeu i Balagueró; Aldrin Antony
Tutor: Joan Bertomeu i Balagueró
Programa de doctorat: Física

Memòria presentada per optar al grau de Doctor amb menció internacional

Barcelona, Gener de 2013

This study was possible, thanks to the economical support from the Generalitat de Catalunya, who provided me the Ph.D. scholarship FI-DGR2010. Moreover, through the programs BE2010 and BE2011, the Generalitat de Catalunya gave me the financial support to do fruitful research internships at the University of South Florida (USA) and at the Forschungszentrum Jülich (Germany).

This work was also supported by the Ministerio de Ciencia e Innovación, the Ministerio de Economía y Competitividad and the European Regional Development Fund through projects CLASICO (ENE2007-67742-C04-03), AMIC (ENE2010-21384-C04-03), MICROSIL08 (PSE-120000-2008-1), INNDISOL (IPT-420000-2010-6) and the European Commission through project HELATHIS (Grant agreement no. 241378).

A mon pare i ma mare.

Contents

Abstract

The objective of the present work is to provide a better understanding of magnetron sputtered transparent conducting oxides based on ZnO in order to use them as electrodes in thin film silicon solar cells at the Grup d'Energia Solar of the Universitat de Barcelona. This thesis presents the properties of magnetron sputtered aluminium and gallium doped ZnO as well as the properties of multi-compound materials deposited by the co-sputtering of zinc oxide and indium tin oxide. The application of ZnO based transparent conducting oxides to the back reflector of *pin* amorphous solar cells is also discussed.

A set of aluminium doped zinc oxide layers were deposited under different substrate temperature and discharge power conditions by radio-frequency magnetron sputtering. The structural, electrical and optical properties were characterised and discussed. The higher substrate temperatures ($\geq 300^{\circ}$C) and discharge powers used during deposition led to highly transparent layers in the visible range (>85%) with lower resistivities. The polycrystalline layers were oriented with the *c*-axis perpendicular to the substrate surface and the crystalline quality of the layers improved at higher temperatures and powers. A remarkable increase in mobility was found for temperatures above 300°C and the carrier concentration also rose with temperature reaching 3.71×10^{20} cm^{-3} at 420°C. The most remarkable feature found at higher deposition power was the increase in deposition rate (from 0.9 to 9 nm min^{-1}).

By means of a high temperature (650°C) annealing process under a capping layer of silicon or alumina, the mobility of aluminium doped zinc oxide layers was considerably raised achieving 68.5 cm^{2}V^{-1}s^{-1}. This process led also to more transparent layers in the near infrared as well as in the ultraviolet part of the spectrum. The influence of annealing in nitrogen, vacuum and air atmosphere was also studied.

Gallium doped zinc oxide was deposited by means of radio-frequency magnetron sputtering in order to investigate the suitability of gallium as a

dopant in zinc oxide layers. Highly transparent layers with higher carrier concentrations but lower mobilities compared to aluminium doped zinc oxide were obtained. The dependence of the layer properties on the pressure, doping concentration, substrate temperature and oxygen volume concentration during deposition were studied in order to find the adequate layer to be applied as electrode in thin film solar cells. 4 wt.% Ga_2O_3 doping concentration was found to be optimal for the production of highly conductive ZnO:Ga layers with a high band gap energy. The incorporation of oxygen gas during the sputter deposition led to more transparent layers at wavelengths longer than 1100 nm, where silicon thin film solar cells do not respond. Moreover, the incorporation of oxygen was found to be detrimental for the electrical properties of the studied layers.

Indium tin oxide layers are widely used as front contact in *nip* solar cells. However, indium is an expensive and scarce material and efforts are made in order to reduce its consumption. Zinc oxide and indium tin oxide were co-sputtered trying to achieve properties as good as indium tin oxide but with reduced indium content. By means of co-sputtering, a set of multi-compound layers formed by Zn-In-Sn-O were deposited and carefully characterised. The resulting layers were studied as a function of the Zn content ratio, which varied between 17.1 to 67.3%. The layers were amorphous in nature but presented embedded nanometric crystals. The incorporation of Zn cations into an indium tin oxide matrix favoured the transmittance but did not modify the mobility. The carrier concentration was found to decrease resulting in an increase in resistivity. The electronic band structure was investigated by means of photoelectron spectroscopy. The measurements showed that, with an increase in Zn concentration, the oxygen vacancy concentration of the surface increased resulting in a degenerately n-doped surface layer. The experiments demonstrated that the work function of the Zn-In-Sn-O surfaces is reduced by about 0.5 eV during ultraviolet photoelectron spectroscopy measurements owing to the photochemical hydroxylation of the surface. Therefore, the work function of the material was determined by low intensity X-ray photoelectron spectroscopy and the values varied between 4.7 and 4.3 eV with the variation of Zn content.

Even though, the majority of this work was focussed on the relation between the deposition conditions and the properties of the resulting materials, the final experiments were focussed on the application of ZnO layers in the back reflectors of *pin* amorphous silicon solar cells. Trials were performed onto *pin* structures deposited at T-Solar Global S.A and the Universitat de Barcelona.

The cells deposited at T-Solar were long exposed to air before a back reflector could be deposited. The interface of the *pin* structure exposed to air for a longer duration was studied, and evidence for the formation of a thin silicon oxide layer was obtained. The oxide layer was removed using acid etching in dilute HF, and the surface was analysed using X-ray photoelectron spectroscopy. The analysis showed that the cleaning step resulted in a huge amount of carbon contamination on the surface. Both, the silicon oxide and the carbon layer led to devices with S-shaped J-V curves, which did not allow us to draw conclusions on the performance of the back reflector. Later, the *n*-type interface was protected by a thin ZnO:Al layer at T-Solar to avoid oxidation during transportation. However, the existence of this thin ZnO:Al protective layer determined the growth of the subsequently deposited layers. Thus, the deposition of ZnO layers under different conditions led to similar results. Finally, different back reflectors were tried over the solar cells fabricated at UB. Aluminium and gallium doped zinc oxide layers were deposited on amorphous silicon *pin* structures, and a clear improvement in performance with respect to devices with only a metal layer as back reflector was observed. Similar performances were observed when Ga doped ZnO or Al doped ZnO was used in the back reflector. It showed that both gallium and aluminium were suitable dopants for the ZnO to be applied in the back reflector.

Resum

L'objectiu d'aquest treball rau en l'estudi i optimització dels òxids conductors transparents basats en l'òxid de zinc. Aquests materials, que s'han dipositat mitjançant polvorització catòdica de magnetró, s'estudiaran amb la finalitat d'emprar-los com elèctrodes en cèl·lules solars de silici en capa prima al Grup d'Energia Solar de la Universitat de Barcelona. En aquesta tesi es presenten les propietats de l'òxid de zinc dopat amb alumini o amb gal·li, així com les propietats de multi-compostos dipositats a partir de la co-polvorització catòdica d'òxid de zinc i d'òxid d'indi dopat amb estany. També es discutirà l'aplicació d'òxids conductors transparents basats en l'òxid de zinc al reflector posterior de cèl·lules solars de silici amorf amb estructura tipus *pin*.

En primer lloc es va dipositar una sèrie de capes d'òxid de zinc dopat amb alumini mitjançant polvorització catòdica de magnetró de radiofreqüència per tal d'estudiar la dependència de les seves propietats amb la temperatura de substrat i la potència. Després del dipòsit es van analitzar i discutir les seves propietats estructurals, elèctriques i òptiques. A altes temperatures de substrat i altes potències, s'han obtingut capes amb una elevada transmitància òptica i una baixa resistivitat. Les capes són policristal·lines i estan orientades amb l'eix c perpendicular a la superfície del substrat. A més, s'ha trobat que la qualitat cristal·lina de les capes augmenta amb la temperatura. Per mostres dipositades per sobre dels 300°C s'observa un augment remarcable de la mobilitat, mentre que la concentració de portadors augmenta al llarg de tot el rang de temperatures de substrat utilitzades, fins assolir 3.71×10^{20} cm^{-3} a 420°C. L'aspecte més significatiu aconseguit amb l'augment de la potència va ser l'increment de la velocitat de dipòsit (de 0.9 a 9 nm min^{-1}).

La mobilitat de les capes d'òxid de zinc dopat amb alumini augmenta considerablement fins assolir 68.5 cm^{2}V^{-1}s^{-1} mitjançant l'aplicació de tractaments tèrmics a alta temperatura previ dipòsit d'una capa protectora de silici amorf o d'alúmina. Aquest procés també ens ha portat a

obtenir capes més transparents en la regió de l'infraroig i l'ultraviolat. A més, s'estudia la influència de l'atmosfera utilitzada (nitrogen, buit o aire) durant el tractament tèrmic.

Posteriorment, es van dipositar capes d'òxid de zinc dopat amb gal·li per tal d'investigar la idoneïtat del gal·li com a dopant. S'ha obtingut una sèrie de capes altament transparents i amb concentracions de portadors superiors a les obtingudes a les capes d'òxid de zinc dopat amb alumini. Per contra, la mobilitat de les capes dopades amb gal·li és molt inferior a la mobilitat obtinguda per les capes dopades amb alumini. Per aquesta sèrie d'òxid de zinc dopat amb gal·li, s'estudia la dependència de les propietats de les capes en funció de la pressió, de la concentració de dopant, de la temperatura de substrat i de la concentració d'oxigen durant el dipòsit amb l'objectiu de trobar les capes més idònies per tal d'aplicar-les com elèctrodes en cèl·lules solars de capa prima. S'ha trobat que una concentració del 4 wt.% de Ga_2O_3 resulta l'òptima per obtenir capes molt conductores amb un valor elevat de l'ample de banda prohibida. L'ús d'oxigen durant el dipòsit millora la transparència de les capes en la regió de l'espectre per sobre dels 1100 nm, on les cèl·lules solars de silici en capa prima ja no responen. D'altra banda, l'ús d'oxigen redueix dràsticament el número de portadors de les capes estudiades.

Les capes d'òxid d'indi dopat amb estany s'utilitzen àmpliament com a contacte frontal a les cèl·lules solars en capa prima amb estructura tipus *nip*. No obstant, l'indi és un material car i escàs i s'estan fent esforços per reduir-ne el seu consum. Per aquest motiu, s'han dipositat capes mitjançant co-polvorització catòdica d'òxid de zinc i òxid d'indi dopat amb estany. La intenció era obtenir capes amb propietats similars a les d'òxid d'indi, tot reduint-ne el seu consum. Al llarg d'aquesta tesi s'ha dipositat i caracteritzat curosament una sèrie de capes del multi-compost format per Zn-In-Sn-O amb diferents composicions de cada element. Els resultats de la caracterització s'han analitzat en funció del contingut de zinc, que varia entre el 17.1 i el 67.3%. Mitjançant microscòpia electrònica de transmissió es va observar que les capes presenten nanocristalls incrustats dins una matriu amorfa. La incorporació del zinc a l'òxid d'indi dopat amb estany afavoreix l'increment de la transmitància, sense que la mobilitat de les capes es vegi afectada. En canvi, la concentració de portadors disminueix, fent que la resistivitat de les capes augmenti. A més a més, s'ha investigat l'estructura electrònica de les bandes mitjançant espectroscòpia fotoelectrònica. Les mesures mostren que, amb l'augment del contingut en zinc, la concentració de vacants d'oxigen a la superfície augmenta, fet que implica l'existència d'una superfície tipus n altament degenerada. Els experiments mostren que la funció de treball de les capes de Zn-In-Sn-O disminueix quan es mesura mitjançant espectroscòpia de fotoelectrons emesos amb llum ultraviolada degut a la hidroxilació fotoquímica de la superfície. Per aquest motiu, la funció de treball dels materials s'ha mesurat mitjançant espectroscòpia de fotoelectrons de rajos X de baixa intensitat. S'han determinat valors de la funció de treball entre 4.7 i 4.3 eV a mesura que s'incrementa el contingut en zinc.

Tot i que la majoria d'aquest treball s'ha centrat en la relació entre les condicions de dipòsit i les propietats de les capes resultants, els experiments finals s'han focalitzat en l'aplicació de capes de ZnO als reflectors posteriors de cèl·lules solars de silici amorf amb estructura tipus *pin* dipositades a T-Solar Global S.A. i a la Universitat de Barcelona.

Les estructures *pin* dipositades a T-Solar van estar exposades a l'ambient durant un llarg període de temps abans que el reflector es pogués dipositar. Per això, s'ha analitzat la interfície de l'estructura *pin* exposada a l'ambient i s'han trobat evidències de la formació d'una capa prima d'òxid de silici. Aquesta capa s'ha eliminat mitjançant un atac químic en àcid HF, i la superfície resultant s'ha analitzat amb espectroscòpia de fotoelectrons de rajos X. L'anàlisi mostra que després del procés de neteja s'elimina la capa d'òxid de silici, però, en canvi, es forma una capa contaminant amb un alt contingut de carboni. Tant les capes d'òxid de silici com la contaminació de carboni que cobreix la superfície de les estructures *pin* han comportat l'obtenció de dispositius amb corbes J-V en forma de S que no ens han permès treure conclusions clares del funcionament de les cèl·lules solars. Posteriorment, per tal d'evitar l'oxidació de la interfície, es va cobrir la capa n amb una capa prima d'òxid de zinc dopat amb alumini a la mateixa fabrica de T-Solar. No obstant, s'ha vist que l'existència d'aquesta capa prima protectora determina el creixement de les capes que s'hi dipositen a sobre. Per aquest motiu, el dipòsit d'òxid de zinc amb condicions molt diverses acaba portant a dispositius amb comportaments pràcticament idèntics.

Finalment, s'han assajat diferents reflectors posteriors sobre cèl·lules fabricades a la Universitat de Barcelona. S'han dipositat reflectors, tant amb òxid de zinc dopat amb gal·li com dopat amb alumini sobre estructures *pin*. S'ha trobat una millora evident del dispositiu si es comparen amb les cèl·lules que utilitzen només el metall com a reflector posterior. D'altra banda, comparant l'ús del gal·li i de l'alumini com a dopants de l'òxid de zinc del reflector posterior, s'ha observat una gran similitud en el comportament dels dispositius. Això ens ha portat a la conclusió que els dos materials són adients per ser emprats com a reflectors posteriors.

1 Introduction

1.1 Framework of this thesis

The global energy scenario is changing owing to the shortage of traditional energy resources (coal, oil, natural gas and uranium). This situation causes an enormous instability as reflected in the rising energy prices and political conflicts in countries with the largest reserves [1]. The world population is growing and has already reached 7000 million [2] implying an increasing demand of energy. In addition, the use of fossil fuels contributes to the accumulation of greenhouse gases in the atmosphere and thus, to the global warming [3]. For these reasons, renewable energy sources are the key given that: they are inexhaustible, environmentally friendly and widely distributed. Energy coming from sunlight, wind, tides, waves or geothermal heat can bring a new energy scenario where different resources spread all over the world will be necessary.

The sun is the most prevalent renewable energy source: it is abundant and worldwide distributed [4]. Energy suppliers can convert solar energy using two techniques, heat generation from thermal collectors [5] and electrical production from photovoltaics. A photovoltaic cell is an optoelectronic device that converts sunlight into electricity. Over the last few years, photovoltaic energy generation experienced an impressive evolution by lowering the cost, leading to an increased installed capacity [4]. In 2011, the photovoltaic industry production increased by almost 40% and reached a worldwide production volume of about 35 GWp of photovoltaic modules [4]. At the end of 2011, the total worldwide solar photovoltaic electricity generation capacity was estimated around 70 GW [4].

Presently, solar modules based on crystalline or polycrystalline silicon have the highest market share (85%) [4]. In laboratories, crystalline silicon solar cell efficiencies as high as 25.0% have been achieved [6, 7]. Despite the huge growth during last years, photovoltaic generation is still a small contributor to the overall energy consumption. To become one of the main providers of energy, a continuous improvement of the technology is needed during the following 10-15 years [8].

An option to reduce the cost of photovoltaic technology is to find a technology where crystalline wafers are not necessary. An alternative is to use thin film based solar cells. In such a case, active layers have only 1% of the thickness of crystalline silicon wafers [9]. A key feature of thin films is that they can be scaled up to be deposited onto low-cost large area glass, and flexible plastic or metal substrates [10].

The investment in thin film modules increased astonishingly between 2005 and 2010 owing to the irruption of turn-key production lines, as well as owing to the temporary shortage of crystalline silicon feedstock [8]. However, because of the current financial and economical constrains and the recent price reduction of crystalline silicon, thin film photovoltaic industries are suffering a lot of difficulties.

The majority of the thin film companies are silicon-based (amorphous and microcrystalline) followed by copper indium gallium selenide and cadmium telluride. However, the dominating thin film technology in the current market is cadmium telluride with a production capacity of 2.1 GW, followed by thin film silicon with 2 GW [8]. Other promising thin film approaches being investigated include dye-sensitised solar cells and organic photovoltaics.

The advantage of using silicon in comparison to other materials for thin film solar cells is the abundance of the raw material, the strong synergy with the flat panel display industry and the large road beyond for further increase in module efficiency [11]. Moreover, thin film silicon solar cells installed in warm climates show a superior performance and energy yield of 15 to 20% compared to crystalline modules of identical nominal power [12]. The highest efficiency achieved in amorphous silicon solar cells is up to now 10.1% [13].

A solar cell device is not only composed of active layers, where sunlight is converted into electricity, but also of electrodes located at each side of the active layers, where the extraction of the photogenerated electrical current takes place. The electrical contact exposed to the sun must be conductive and transparent to the incident photons so that maximum light will reach the absorber layer. This transparent and conducting materials are generally based on metal oxides known as transparent conducting oxides (TCOs). Moreover, at the rear side of the solar cell, a TCO/metal double structure, known as back reflector, is used to collect the photogenerated current.

TCOs constitute an unusual class of materials with wide band gaps ($>$ 3 eV) and high electrical conductivity. These semiconductor materials are not only used as electrodes in solar cells but are present in a wide range of applications in portable and flexible electronics, plasma displays, multifunctional windows, etc. [14]. Among different TCOs, the common n-type inorganic TCOs are Al or B doped ZnO, Sn doped In_2O_3 and F doped SnO_2 [15]. ZnO fulfills the requirements to be a TCO for thin film solar cells: it is transparent over the part of the solar spectrum where solar cells respond, it is conductive enough, can be easily textured to enhance light trapping, it is abundant and it can be easily deposited over a large area. Moreover, ZnO is more resistive to hydrogen plasma compared to SnO_2 and In_2O_3 [16]. The last requirement is necessary when a TCO layer has to be exposed to a highly reducing atmosphere, like that existing when depositing microcrystalline silicon by plasma enhanced or hot-wire chemical vapour deposition.

Most of the applications use aluminium as dopant in ZnO [17–19] and its suitability is extensively proved [20, 21]. Nevertheless, other dopants like B, Ga, In and Sn lead to comparable resistivities of the zinc oxide films [22]. In case of Ga, the slightly smaller bond length of Ga-O in comparison to Zn-O is advantageous since it allows to reduce the deformation of the ZnO lattice even for high gallium concentrations [23].

On top of already deposited active layers, as in the case of the front TCO in *nip* solar cells, Sn doped In_2O_3 (ITO) is widely used. ITO is also used for heterojunction solar cells [24] and organic solar cells [25] owing to the high transparency in the visible range, low resistivity and high work function. Nevertheless, indium is a scarce and expensive element [26] and, moreover, amorphous ITO films deposited at low temperature are degraded under moist heat, and, thus, its conductivity and light transmittance are reduced with time [27].

1.2 Grup d'Energia Solar

The Grup d'Energia Solar (GES) at the Universitat de Barcelona (UB), where this thesis was carried out, is focussed on the development of thin film silicon based solar cells. Within this topic, the group mainly works in three different fields: the development and deposition of thin film silicon layers by means of hot-wire chemical vapour deposition (HWCVD), the study of transparent conducting oxides and light confinement strategies and the monitoring of the performance of photovoltaic modules under real conditions with the aim to elaborate realistic models for thin film silicon modules.

The group is financed by Catalan, Spanish and European public administrations through different research projects. Some projects not only involved other research centers and universities, but also key companies in the thin film photovoltaics sector. Some of the experiments performed during this thesis were part of the milestones of such projects.

Through the MICROSIL08 (*Diseño e industrialización de módulos fotovoltaicos de silicio en capa fina*) project, the magnetron sputtering equipment used in this thesis was acquired, and the first trials to deposit and characterise thin films were done.

Moreover, the group took part in the FP7 European project, High Efficient Very Large Area Thin Film Silicon Photovoltaic Modules (HELATHIS). The coordinator of this project was the company T-Solar Global S.A. (TS), which produces very large area amorphous silicon modules and has an annual production capacity of 72 MWp/year. Other partners of this consortium were the company AGC Flat Glass Europe, Universiteit Utrecht and the Forschungzentrum Jülich (FZJ), where an internship was carried out during this thesis. The HELATHIS project was aimed to optimise module efficiency by improving optical confinement strategies. Light trapping is the key issue for silicon thin film solar cells and the TCOs play a crucial role in enhancing the cell efficiency. This included the optimisation of the properties of TCO layers at the front side and the back reflector for large area deposition. Additionally, methods for the reduction of the reflectance losses at the front glass were developed. This optimisation was done, on one hand, for single junction amorphous silicon modules and, on the other hand, for modules with amorphous and microcrystalline silicon tandem junction. In the latter case, an intermediate reflector is also needed. Some parts of the studies presented in this thesis are related to the fifth work package of HELATHIS project. This work package was focussed on the optimisation of the TCO/metal stack which conforms the back reflector (BR). Along with the front TCO, the BR plays a crucial role in *pin* type silicon solar cells by increasing the optical path of light inside the device, thus resulting in a short circuit current gain.

1.3 Aim and outline of this thesis

The objective of this PhD thesis was to provide a better insight into multi-compound and doped ZnO-based transparent conducting oxides deposited by magnetron sputtering. These materials are used as electrodes in thin film silicon solar cells at the Grup d'Energia Solar. This work presents the properties of magnetron sputtered aluminium and gallium doped ZnO as well as multi-compound materials deposited from the co-sputtering of zinc oxide and indium tin oxide. ZnO-based back reflectors were applied to *pin* amorphous silicon solar cells and the interface between the *n*-layer and the TCO was analysed. The results contributed to the different research activities of the group during the past four years.

The thesis is structured as follows: after this brief introduction, the fundamental knowledge used to discuss the results is presented in Chapter 2. Next, the experimental details of the equipments and characterisation techniques used are detailed in Chapter 3. In Chapter 4, the results on the aluminium doped ZnO are presented. The layers were deposited by varying the substrate temperature and discharge power and the material properties were found to depend on the deposition parameters used. Moreover, the optical and electrical properties of ZnO:Al layers annealed at high temperature are also presented. This experiment was performed at FZJ in order to obtain layers with higher carrier mobilities. Chapter 5 presents the properties of gallium doped zinc oxide, where gallium is explored as an alternative dopant to the conventional aluminium. The layers were deposited by sputtering under different pressures, doping concentration, temperature and oxygen concentration. ZnO was lately co-sputtered with In_2O_3 doped with SnO_2 in order to find a TCO with properties as good as ITO but with reduced indium content. The properties of Zn-In-Sn-O multi-compound layers are presented in Chapter 6. The work function and the surface electronic band structure of these samples were studied during an internship at the University of South Florida (USF), in the United States. Chapter 7 discusses the application of ZnO-based TCOs in solar cells. The experiments in this chapter were performed in the framework of the HELATHIS project. Back reflectors were deposited onto *pin* structures fabricated at TS or UB and the resulting cells were characterised. Finally, a short summary is provided in Chapter 8.

2 Fundamentals on transparent conducting oxides

In this chapter, the basic knowledge used to interpret the results obtained throughout this thesis is presented. The different concepts are briefly described, and references are also cited. The main properties of the transparent conducting oxides, and more specifically of zinc oxide and indium oxide are presented. Afterwards, a growth model which connects the deposition conditions with the structural properties is presented. The electrical properties of zinc oxide and indium oxide are then discussed. Concretely, the Drude model, the doping mechanisms, the transport models and the electronic band structure are presented. Next, the optical features of the two materials used throughout this thesis are briefly explained. Finally, the basics of thin-film silicon solar cells are shortly introduced.

2.1 Transparent conducting oxides

Transparent conducting oxides constitute an unusual class of materials given that they possess a relatively high electrical conductivity and a high transparency in the visible range. TCOs are typically used in devices such as thin film solar cells or flat panel displays given that, in these devices, it is necessary to make the electrical contact, transparent to the incident or emitted photons. TCOs present a band gap larger than 3 eV, transmittances in the visible range above 80% and resistivities as low as $10^{-4}\ \Omega\,\mathrm{cm}$ [15]. The mostly used TCOs have been n-type degenerated semiconductors consisting of metal oxides. The common inorganic TCOs are ZnO, In_2O_3 and SnO_2 [15]. Binary compounds, such as those aforementioned, are easy to manage since their chemical composition is easy to control. Nevertheless, many ternary or multi-compound materials such as Zn-In-Sn-O are transparent and conducting [28].

TCOs are used for a variety of applications including window defrosters;

liquid-crystal, electrochromic, electroluminescent, and plasma displays; solar cell electrodes; infra-red reflectors for energy-efficient windows; touch screens; abrasion- and corrosion-resistant coatings; gas sensors, etc. [15].

This work focusses on improving TCO materials for thin film solar cell applications. In such a case, the layers must be transparent in the region between 350 and 800 nm for hydrogenated amorphous silicon solar cells (a-Si:H) or between 350 and 1100 nm for hydrogenated microcrystalline silicon solar cells (μc-Si:H). They should also present a good electrical conductivity, should be easily textured to enhance light trapping and be chemically stable to hydrogen plasma [29]. TCOs are also used as enhanced back reflector for long wavelength light in combination with a highly reflecting metal at the back contact [30]. For sustainable large scale production of solar cells, the material must fulfill the aforementioned properties, but also must be an abundant, non-toxic and low processing cost material with the possibility of being deposited on a large area.

2.1.1 Zinc Oxide

Doped zinc oxide presents good optical and electrical properties and is considered as one of the most promising TCOs [15]. ZnO is a low cost TCO since it is abundant in the Earth crust [31]. Moreover, it presents a high stability against hydrogen plasma compared to In_2O_3 or SnO_2 [16, 32], which is advantageous for the deposition of thin film silicon solar cells.

ZnO is deposited by a wide variety of methods, and the lowest resistivity of $1.4\times10^{-4}\ \Omega\,\mathrm{cm}$ was reported for a heteroepitaxially sputtered ZnO [33] and a pulsed laser deposited film [34]. Thin film silicon solar cells use either sputtered and etched aluminium doped ZnO [35] or natively textured boron-doped ZnO deposited by low pressure chemical vapour deposition (LPCVD) [36] as the front electrode.

ZnO generally crystalises in a wurtzite structure (see Fig. 2.1). Other crystal structures such as zincblende or rocksalt are found under specific deposition conditions [37]. The wurtzite crystal structure is an example of a hexagonal crystal system, and, thus, it is characterised by two lattice constants: a and c. In case of ZnO, a=0.3250 nm and c=0.5207 nm [38]. The ratio between the lattice constants ($c/a = 1.60$) is close to the ratio obtained for an ideal hexagonal cell ($c/a = (8/3)^{1/2} = 1.63$). ZnO in the wurtzite structure is composed of two (for each kind of atom) inter-

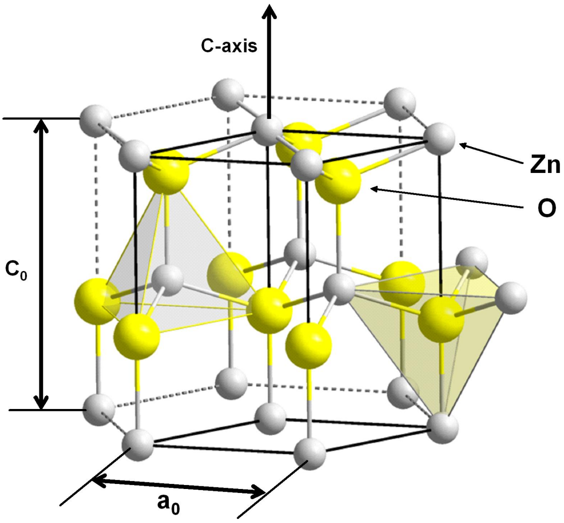

Figure 2.1: Diagram of ZnO wurtzite crystal structure.

penetrating hexagonal sublattices separated by an offset along the *c*-axis [39].

Each Zn or O atom is tetrahedrally bonded to four neighbours of the other type. The wurtzite structure does not have inversion symmetry along the *c*-axis, so the planes are Zn- or O-terminated. Moreover, the Zn-O bond is primarily ionic and thus, it leads to planes of positively charged zinc and negatively charged oxygen perpendicular to the *c*-axis. The lack of symmetry and the polarisation of the ZnO atomic planes implies that the material is piezoelectric.

The electrical and optical properties of ZnO are reported to be stable in ambient conditions at room temperature for long periods of time [40]. However, the exposure of a ZnO sample to high temperatures [41] or to damp heat degradation [42] can lead to the worsening of the electrical properties. However, the degradation depends strongly on the deposition conditions used to obtain the layers [41] and on the atmosphere and temperature used to anneal the samples [40]. In certain cases, thermal treatments can be used to improve the electrical and optical properties of ZnO layers as in case of annealing processes under capping layers [43].

Further details on the electrical properties such as the extrinsic dopants used or the electronic band structure as well as the optical properties of ZnO are detailed in subsequent sections.

2.1.2 Indium oxide

Indium oxide (In_2O_3) is a wide band gap (3.7 eV [44]) semiconductor, which presents excellent properties when it is doped with tin. Among the TCO thin films, indium tin oxide (In_2O_3:SnO_2) known as ITO, is widely used owing to its unique electrical ($\sim 1\times10^{-4}$ Ωcm) and optical (~ 85% in the visible region) properties [14]. Up to now, ITO yields the lowest resistivity of 4.4×10^{-5} Ω cm [45].

Crystalline In_2O_3 exists in two phases, the cubic (bixbyite type) and the rhombohedral (corundum type). The rhombohedral structure is achieved at high temperatures or pressures. The cubic structure (see Fig. 2.2) is commonly found in sputtered layers such as those studied here. The cubic lattice constant is reported to be 1.0118 nm [46].

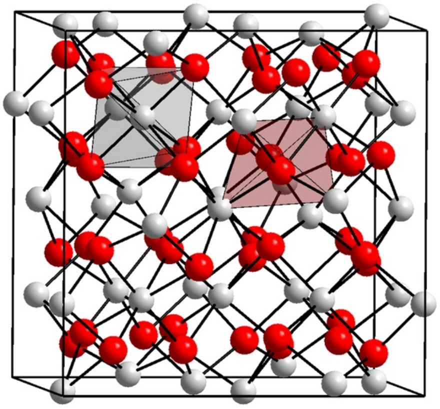

Figure 2.2: Diagram of In_2O_3 bixbyite crystal structure [47].

ITO owes its relatively low electrical resistivity to its high free carrier concentration (1-2$\times10^{21}$ cm^{-3}[14]). However, it also implies a high reflectance in the near infrared part of the spectra. Free carriers in ITO are formed by two different kinds of electron donor sites: substitutional four-valent Sn ions and oxygen vacancies [48]. The mostly used ITO compounds are doped with a 5 to 10 at.% of SnO_2 [14]. ITO layers are quite stable under damp heat degradation tests in comparison to ZnO [49, 50].

The drawback of using In_2O_3 is the difficulty to expand the market owing to the cost and scarcity of indium [26]. Furthermore, the material is not stable under hydrogen atmosphere [16, 32] owing to the reduction of oxide to metallic indium at the film surface. This effect drastically reduces the film transmittance.

Further details on the electrical and optical properties of In_2O_3 are detailed in subsequent sections.

2.2 Deposition and growth of TCO materials by magnetron sputtering

A huge variety of methods can be used to deposit TCO materials including, pulsed laser deposition [51], magnetron sputtering [52], LPCVD [36], spray pyrolysis [53], ink-jet printing [54], etc. Magnetron sputtering was used to deposit the transparent conducting oxides for this thesis. Magnetron sputtering is one of the most suitable techniques since it can yield large area depositions achieving optimal electrical and optical TCO properties. The working process, as well as the equipment description, are detailed in Sec. 3.1.

Sputtered atoms travel between the target and the substrate suffering collisions (deflections) which broaden the angular distribution of the incoming particles. If the particles reaching the substrate have a low kinetic energy, they can be adsorbed (adatoms) and diffuse to find the lowest energy site to bond. Instead, high kinetic energy particles are implanted within the growing film. In such a case, the energy delivered by the collisions may knock other particles from the growing surface and back to the vacuum as vapour. This process is known as resputtering [39].

The distance that a particle can diffuse depends strongly on the mass. Small particles may diffuse along relatively large distances. Sometimes they can even diffuse into the bulk, but the amount of energy required is higher. For even higher energies, the incoming particle may even desorb from the growing surface [39].

The rate at which each growing process occurs depends on the deposition conditions which define the energy of the sputtered particles. For example, the higher the temperature, the higher the ability of the incoming particles to diffuse along the surface, bulk or even desorb. The pressure influences the sputtering rate and mean free path of the incoming particles. Other parameters such as discharge power, target doping, layer thickness or oxygen volume concentration will also influence the deposition process and thus the electrical and optical properties of the resulting layer [39]. Further details on the sputter deposition processes can be found elsewhere [55–57].

Two growth models will be presented to shred up some light into the relationship between deposition parameters and resulting film properties.

2.2.1 Survival-of-the-fastest

The properties of polycrystalline layers depend strongly on the thickness owing to the increase in grain size with the film thickness [58]. Van der Drift attributed the domination of certain crystalline orientations to the *survival-of-the-fastest*, where the fastest growth rate of certain orientations overgrows the slower ones [59].

In case of ZnO, c-axis growth posses the minim surface energy [60] and, thus, in equilibrium, it dominates the growth. The resulting films are (002) oriented, with the c-axis perpendicular to the substrate surface, even if samples are grown at room temperature and low discharge power [61].

In case of In_2O_3, there is not a crystalline orientation as dominant as in ZnO. Instead, varying the temperature [62] and oxygen concentration [63] the preferred orientations also vary. At low substrate temperatures and moderate discharge powers, doped In_2O_3 layers tend to grow amorphous [64, 65]. When increasing the substrate temperature or the energy of the incoming particles, either (100), (111) or (100), among other crystalline orientations can be found [62, 66].

2.2.2 Modified Thornton model

Thornton extended an experimental growth model designed for evaporation to sputtered metal films [67]. Lately, Kluth *et. al.* [68] introduced changes to the model in order to adapt it to magnetron sputtered ZnO films (see Fig. 2.3). Thornton differentiates three different growth zones as a function of the ratio between the substrate temperature T and the materials melting temperature T_m, and the deposition pressure p. Kluth *et. al.* replaced the aforementioned temperature ratio by the substrate temperature and exchanged the pressure and temperature axis. Owing to the high melting point of ZnO [69], Zone 3 of the original Thornton model is not considered by Kluth *et. al.* [68] since that cannot be achieved by sputtering onto glass substrates. However, the general statement of the original Thornton model is maintained: increasing the substrate temperature and reducing the sputter pressure leads to a more compact and dense film structure.

Zone 1 of the modified Thornton model consists of a loosely packed material. Low substrate temperatures lead to low adatom mobility and thus, the incoming particles are deposited next to the absorption site. Therefore, the crystallites grow accordingly to the sputtering flux and voids are formed between small crystals. As pressure is increased, the higher amount of collisions suffered by the incoming particles reduce their kinetic energy and thus, higher temperatures still result in zone 1 material.

Zone 2 is formed by large columnar grains, separated by grain boundaries. Now, the surface mobility is higher, and adatoms can diffuse to preferred bonding sites. In Zone 2, grain boundaries can recrystallise, and bigger grains are formed. Limits between regions are not abrupt; instead stepwise transition zones exhibiting characteristics between each zone can be found (depicted as zone T in Fig. 2.3)

This model is helpful to understand how the layer properties vary with the deposition conditions. Moreover, the model is useful to correlate the morphology of the ZnO layers etched by means of HCl with the deposition conditions. The roughness obtained after HCl etching depends strongly on the compactness of the layers [39, 68] and characteristic features can be found within each zone of the modified Thornton model.

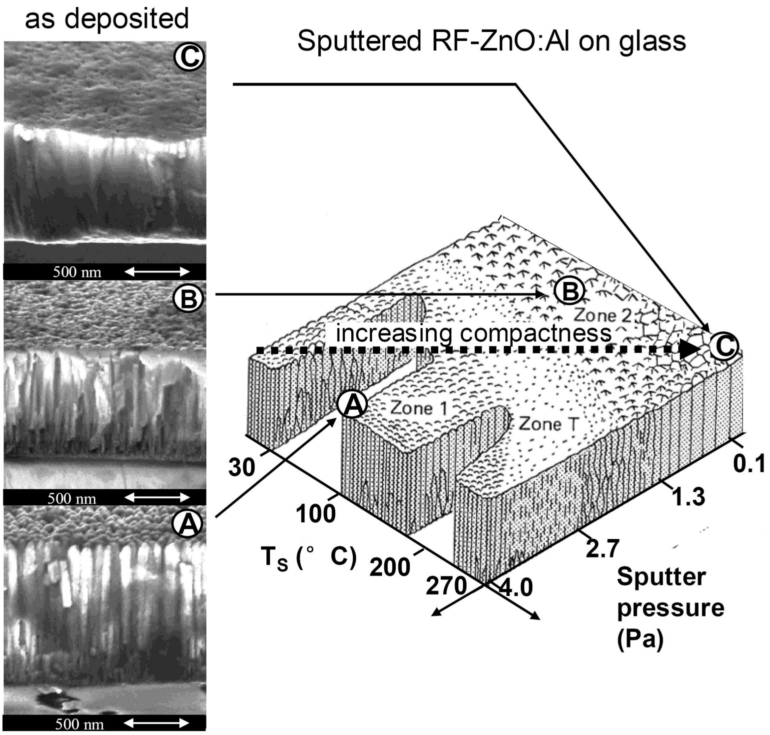

Figure 2.3: Thornton model for the growth of sputtered ZnO:Al layers. Reprinted from Thin Solid Films [68], with permission from Elsevier.

2.3 Optical properties

For a certain wavelength (λ), the incident light on a TCO can be either transmitted, reflected or absorbed depending on the material. By experimentally comparing the total transmittance (T) and reflectance (R) to the initial beam, the absorptance (A) can be calculated as follows:

$$A(\lambda) = 1 - T(\lambda) - R(\lambda) \tag{2.1}$$

The transmittance and reflectance of a material can be described by means of the Drude model, which is a classical model [70] for free electrons in metals. Drude made two assumptions to adapt the free electron model to doped semiconductors. First, he used the effective mass (m^*) instead of the electron mass, to take into account that electrons are moving in the conduction band of a semiconductor. Secondly, the relative permittivity was taken as ε_∞ at the frequency range of interest [71].

The effective dielectric function $\varepsilon(\omega)$ of the Drude model includes both, the dielectric and the free carriers contribution and can be written as:

$$\tilde{\varepsilon}(\omega) = \varepsilon_\infty \left(1 - \frac{nq_e^2}{\varepsilon_\infty \varepsilon_0 m^* (\omega^2 - \mathbf{i}\omega\gamma)}\right) = \varepsilon_\infty \left(1 - \frac{\omega_p^2}{\omega^2 + \mathbf{i}\omega\gamma}\right) \tag{2.2}$$

where, ε_0 is the vacuum permittivity, m^* is the effective mass of an electron in the semiconductor material, q_e the fundamental charge of an electron, n is the charge carrier density, γ is the damping frequency and ω_p is the plasma frequency defined as:

$$\omega_p = \sqrt{\frac{nq_e^2}{\varepsilon_\infty \varepsilon_0 m^*}} \tag{2.3}$$

each frequency can be converted into wavelength using $\lambda = 2\pi c/\omega$. Where c is the speed of light.

Analysing the real part of the effective dielectric function, three different scenarios are found. When the angular frequency of the incoming light is higher than the plasma frequency ($\omega > \omega_p$), then $\varepsilon(\omega) > 0$. In this case, light can be transmitted through the material. On the contrary, when $\omega < \omega_p$, $\varepsilon(\omega) < 0$. Now, the light cannot propagate through the material, i.e. is reflected. At $\omega = \omega_p$ light is partially transmitted and partially reflected. Both, the transmittance and reflectance show a sharp edge next to the plasma frequency.

Polycrystalline materials like those studied throughout this thesis are far from being perfect materials. Therefore, the plasma frequency is not confined to a unique wavelength. Instead, a broad peak can be observed. The width of the peak is also related to the electrical mobility of the layer [72]. The higher the mobility is, the sharper the resonance peak.

TCO materials present three key spectral features as seen in Fig. 2.4. First, the material is quite transparent ($\sim 80\%$) in the visible range where oscillations due to thin film interferences can be found. Second, light is

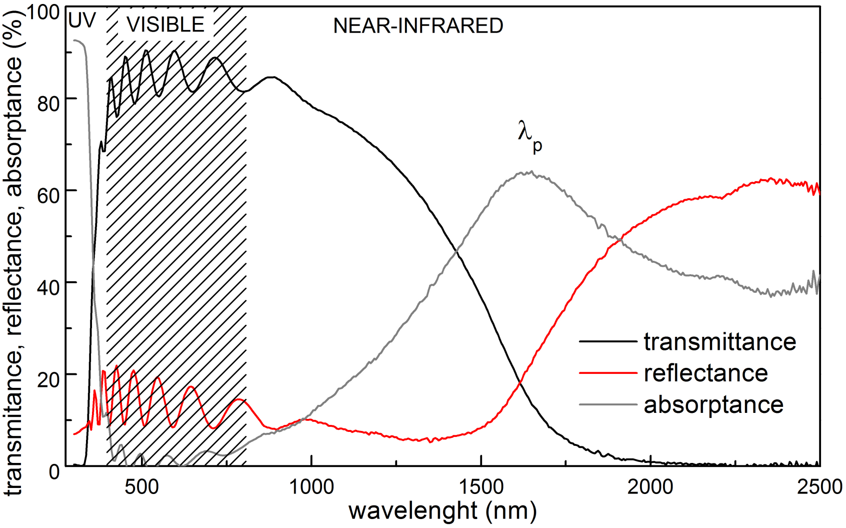

Figure 2.4: Optical spectra of a typical transparent conductor oxide.

strongly absorbed in the ultraviolet part of the spectra due to optical band gap absorption. Third, at long wavelengths, near to the plasma frequency, transmittance gradually decreases and reflectance increases. The different regimes will be detailed below.

2.3.1 Ultraviolet region (300-400 nm)

In the ultraviolet (UV) range, the transmittance drops because the electrons absorb the energy of the incoming photons to transit between the valence and conduction band [14]. If the incoming energy is higher than the band gap of the material, the light is strongly absorbed.

The absorption coefficient (α), for a strongly absorbing medium where multiple reflections are negligible, can be determined from the transmittance and reflectance by means of Eq. 2.4 [73]

$$T \approx (1 - R)^2 exp(-\alpha d) \tag{2.4}$$

where d is the layer thickness, R is the reflectance and T is the total transmittance. For direct transitions, as in case of ZnO and ITO films, the absorption coefficient follows Eq. 2.5 [73]

$$\alpha h\nu = B(h\nu - E_g)^{1/2} \tag{2.5}$$

where $h\nu$ is the incident photon energy, E_g is the band gap energy and B is a constant. The band gap of the TCO films can be estimated from the Tauc plot of $(\alpha h\nu)^2$ against $h\nu$ by extrapolating to zero the linear portion of the $(\alpha h\nu)^2$ curve.

When studying highly doped semiconductors, which present a high carrier concentration, a band gap displacement towards higher energies is observed. This shift was firstly observed by Burstein [74] and Moss [75]. In highly doped semiconductors, the bottom of the conduction band is occupied. Therefore, new states must be at higher unoccupied energies. Assuming a degenerately doped n-type semiconductor, the broadening follows the equation:

$$\Delta E_{BM} = \frac{h^2(3\pi n)^{2/3}}{8m^*} \tag{2.6}$$

where h is Planck's constant, n is the free carrier density and m^* is the effective mass.

2.3.2 Visible region (400-1000 nm)

In the visible (VIS) range and sometimes part of the near infrared range, the material is quite transparent ($\sim 80\%$). This transparent window makes the TCOs suitable to be applied as electrodes in thin film solar cells.

As long as the coherence between the incoming light and the layer thickness of flat layers is maintained, constructive and destructive interferences cause oscillations in the transmittance and reflectance spectra. The maxima, minima and period of the interferences can be used to estimate the thickness of the film [76]. This effect disappears in randomly textured thin films.

2.3.3 Infrared region (1000-2500 nm)

In the near infrared (NIR) region, the transmittance decreases and the reflectance increases owing to a change of the effective dielectric function from positive to negative values as detailed in Sec. 2.3. A prominent absorption takes place around the plasma frequency.

The mobility and the carrier concentration can modify the shape and position of the free carriers absorptance peak. As the density of electrons in the conduction band, n, is increased, the plasma frequency shifts to higher values (shorter wavelengths as $\lambda_p \propto 1/\sqrt{n/m^*}$). Therefore, there is a fundamental tradeoff between carrier concentration and transparency in the long wavelength range. At very high carrier concentrations, the plasma frequency even reduces the transmittance in the visible wavelength range.

2.4 Electrical properties

TCO materials are highly doped semiconductors and their charge carriers partially follow the free electron model developed for metals. Although the conduction is essentially described by quantum mechanics, Drude proposed a model [70] that describes most of the properties of the TCOs. Free electron systems are those in which the electrons experience no restoring force from the medium when driven by the electric field of a light wave [71]. This model was already mentioned in Sec. 2.3 to describe the effective dielectric function. The conductivity in Drude's model can be written as:

$$\tilde{\sigma} = \frac{\sigma_0}{1 + \mathbf{i}\omega\tau} \tag{2.7}$$

where τ is the average time between collisions and σ_0 is defined by:

$$\sigma_0 = \frac{n q_e^2 \tau}{m^*} \tag{2.8}$$

where n is the charge carrier concentration, m^* is the effective mass and q_e is the elemental charge of an electron.

Using Ohm's law and the Drude model, the conductivity σ, or the resistivity ρ for $\omega = 0$ can be written as:

$$\sigma = \frac{1}{\rho} = \frac{q_e n \mu}{1} = \frac{n q_e^2 \tau}{m^*} \tag{2.9}$$

where $\mu = q_e \tau / m^*$ is the mobility. Further details regarding Drude model can be found in [71, 77].

To understand the electrical properties that characterise a TCO material, further concepts have to be taken into account. Therefore, the different doping mechanisms that confer a degenerate character to the semiconductors are presented. Afterwards, the different transport mechanisms that may affect the layers are described. Finally, the electronic band structure of the TCO materials used throughout this thesis is presented.

2.4.1 Doping mechanisms

Stoichiometric ZnO or In_2O_3 are not degenerately doped materials and, thus, they do not behave like metals. Nevertheless, they can be easily n-type doped and their carrier concentration can increase orders of magnitude. Different mechanisms can be used to raise the charge carrier concentration and will be detailed below.

2.4.1.1 Intrinsic doping

When depositing a material it can grow intrinsically doped owing to defects within the crystal structure. In ZnO and In_2O_3, the slightly non-stoichiometric growth results in oxygen vacancies or metal interstitial lattice sites. In such cases, some metal to oxygen bond is missing, and the resulting metal to metal bond is weaker and thus, smaller energies than the band gap can excite electrons from the valence to the conduction band. Interstitial metal atoms are shallow donors. Instead, defects like O vacancies are deep level donors [14].

Carrier concentrations higher than 10^{20} cm^{-3} and up to 10^{19} cm^{-3} have been respectively reported for intrinsic ZnO [78] and In_2O_3 [79]. However, intrinsically doped films are not stable at ambient conditions and especially at higher temperatures, because of the filling of the oxygen vacancies [80].

2.4.1.2 Extrinsic doping

TCO materials can be doped by introducing a foreign element into the crystal structure. Such elements normally have one extra valence electron in the outer shell in comparison to the atoms of the original matrix.

There are three requirements to dope a material successfully: the dopant should be soluble in the intrinsic material lattice, the dopant level should be shallow and the dopant should not be compensated by intrinsic defects [14].

In case of ZnO, the most common dopants are Al [81], Ga [82], B [83] and In [84]. When using In_2O_3 as a TCO it is usually doped with Sn [85].

Foreign elements are added during deposition and substitutional doping may be achieved. In such a case, the dopant (Al^{3+}, Ga^{3+}, Sn^{4+}, etc.) occupies the metal ion site in the crystalline lattice providing the material with a weakly bonded extra electron [22]. The energies required to release the extra electron (binding energy) of the aforementioned dopants are between 50 and 70 meV, depending on the element. These energies are much smaller than the band gap energy and thus, it is easier to excite a dopant electron rather than an intrinsic electron from the valence to the conduction band.

Dopant species may also segregate and deposit at the grain boundaries complicating the conduction within the grains.

2.4.1.3 Hydrogen doping

Hydrogen can be easily incorporated in the crystal lattice and act as a shallow donor or acceptor. It can play a role in extrinsic and intrinsic doping processes given that its incorporation during deposition is unavoidable. The concentration of hydrogen depends strongly on the deposition method used. In case of magnetron sputtered polycrystalline layers, concentrations as high as 10^{20} cm^{-3} have been reported [37].

In most semiconductors, hydrogen is amphoteric, acting as donor and acceptor. In such a case, it cannot be the cause of conductivity since it self-compensates. ZnO and In_2O_3 belong to the few oxides, in which hydrogen acts exclusively as a donor [86, 87].

Recently, high mobilities (90-130 $cm^2V^{-1}s^{-1}$) and high transparency have been achieved for In_2O_3 layers intentionally doped with hydrogen. These films are deposited by sputtering from an In_2O_3 target in a water vapour atmosphere at room temperature. After an annealing process at 200°C, the amorphous samples become polycrystalline and the mobility and transparency of the layers are drastically improved [88].

2.4.1.4 Degenerately doped materials

Once the material is highly doped, and the Fermi level lies into the conduction band, the semiconductor is said to be degenerate. Then, little energy is needed to free the carriers from the weak bonds. The material behaves like a metal having no band gap. Nevertheless, the optical band gap still exists, and the material is transparent to the incident photons with energies lower than the band gap. The critical carrier concentration needed to have a degenerate semiconductor is given by the Mott criterion [89]:

$$n_{critical}^{1/3} a_0 \approx 0.26 \tag{2.10}$$

where a_0 is the effective Bohr radius given by,

$$a_0 = \frac{h^2 \varepsilon_r \varepsilon_0}{\pi q_e^2 m^*} \tag{2.11}$$

h is Planck's constant, q_e the fundamental electrons charge, ε_0 the vacuum permittivity and ε_r the relative permittivity, also known as static dielectric constant. ε_r is 8.75 and 8.9 for ZnO and In_2O_3 respectively [14] and thus, the critical carrier concentration is in both cases around 10^{18} cm^{-3}. This critical carrier concentration is far below the carrier concentrations found in this thesis for all the deposited layers. Therefore, all the materials presented throughout this work can be considered degenerated semiconductors.

2.4.2 Electrical transport

The electrical transport in polycrystalline materials is much more complex than in single crystals [90]. The limiting electrical transport mechanisms that microscopically affect the degenerately doped materials studied in this thesis are the ionised impurity scattering and the grain boundary potential barrier. Other limiting mechanisms may affect the electrical mobility of TCOs but are not deeply discussed since they did not influence the polycrystalline and degenerate layers described here.

The mobility resulting from Hall effect measurements is affected by many limiting mechanisms and cannot be higher than any of them. The resulting mobility can be expressed as the reciprocal sum of every single limiting process [91]:

$$\frac{1}{\mu} = \sum_i \frac{1}{\mu_i} \tag{2.12}$$

2.4.2.1 Ionised impurity scattering

This scattering mechanism takes place because of the deflection of free carriers by the Coulomb potential of charged doping impurities (for instance Sn^{4+} or Al^{3+}). The higher the carrier concentration the lower the mobility that will be obtained when ionised impurity scattering is the limiting mechanism. It has been stated [80, 92, 93] that this scattering mechanism can limit the mobility in TCO materials for carrier concentrations above 10^{19} cm^{-3} [94].

An empirical model for the mobility as a function of the carrier concentration was adapted from silicon to zinc oxide by Ellmer and Mientus [94]. For a degenerately doped semiconductor, the mobility owing to ionised impurities μ_{ii} is proportional to the squared ratio of its relative permittivity, ε_r and the effective mass of the charge carriers m^* [95]: $\mu_{ii} \propto (\varepsilon_r/m^*)^2$.

2.4.2.2 Grain barrier limited transport

Depending on the size of the grains in polycrystalline layers, the potential barriers existing at grain boundaries can play a major role in scattering the carriers. Ellmer *et al.* adapted a grain barrier limited transport model of Seto [96] from polycrystalline silicon to polycrystalline zinc oxide and indium tin oxide [37, 94]. The polycrystalline layer is assumed to be an array of grains of identical lateral size L. The basics of this model states that the majority of the defects are at the grain boundaries, which are crystallographically disturbed regions full of defects with energies within the band gap. Those defects trap free carriers that at the same time cause a charge depletion or accumulation zone at both sides of the grain boundary. For a charge carrier to account for conduction in a polycrystalline layer, it must overcome the potential barrier at the grain boundaries E_b (see Fig. 2.5).

The model adapted from Seto yields an effective mobility μ_{gb} dominated

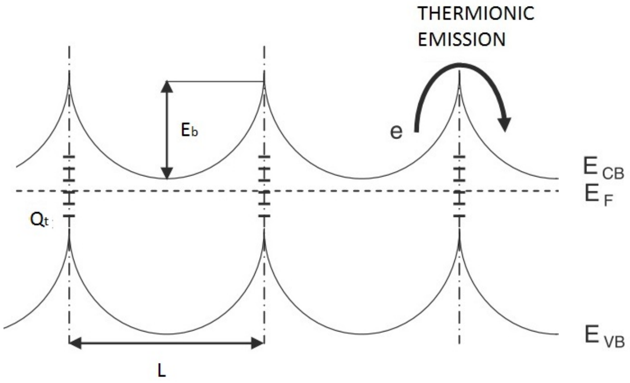

Figure 2.5: Energy diagram of a linear row of grains of identical lateral length L, with grain barriers of height E_b, caused by a continuous electron trap density, Q_t [37] with kind permission from Springer Science+Business Media B.V.

by thermionic emission, i.e. heat induced flow of charge carriers over a potential energy barrier E_b.

$$\mu_{gb} = \mu_0 \exp\left(\frac{-E_b}{k_B T}\right) \tag{2.13}$$

where k_B is Boltzmann's constant and T the absolute temperature. μ_0 can be thought as the mobility within a grain [96] and it is given by:

$$\mu_0 = \frac{q_e L}{\sqrt{2\pi m_e^* k_B T}} \tag{2.14}$$

Here, L is the lateral grain size, q_e is the electron charge, and m^* is its effective mass. From Eq. 2.13 and 2.14, it is deduced that a higher lateral grain size implies a higher grain boundary effective mobility. In a sample with a carrier density within a grain n, and a trap density Q_t at the grain boundary, the potential energy barrier is given by:

$$E_b = \frac{q_e^2 Q_t^2}{8\varepsilon_r \varepsilon_0 n} \quad for \;\; Ln > Q_t \tag{2.15}$$

and

$$E_b = \frac{q_e^2 L^2 n}{8\varepsilon_r \varepsilon_0} \;\; for \;\; Ln < Q_t \tag{2.16}$$

Three different relationships between the number of carriers within a grain, the lateral grain size and the trap density affect the barrier height. When the number of carriers is greater than the number of traps $Ln > Q_t$, the traps are entirely full, and the potential energy barrier decreases as the inverse of the increase in carrier concentration (Eq. 2.15). Instead, when the number of carriers within a grain is lower than the number of traps at the grain boundaries $Ln < Q_t$, carriers are entirely depleted, and the potential energy barrier increases linearly with the increase in carrier density or quadratically with the increase in grain size (Eq. 2.16). The maximum barrier height E_b and, thus, the lowest mobility occurs when $Ln = Q_t$.

For comparable deposition conditions, doped ZnO presents a higher trap density than ITO [94]. Whereas for ZnO, Q_t was estimated to be between $5{\times}10^{12}$ and $3{\times}10^{13}$ cm^{-2}, for ITO it was estimated around $1.5{\times}10^{12}$ cm^{-2} [94]. Grain boundary scattering will be more influencing in case of polycrystalline ZnO rather than in ITO.

Within this work, the carrier concentrations found for ZnO:Al and ZnO:Ga were between $6{\times}10^{19}$ and $9{\times}10^{20}$ cm^{-3}. Lateral grain sizes were not measured here, but for sputtered zinc oxide, values between 20 to 150 nm were reported [97–99]. Thus, $Ln \approx 1{\times}10^{14} - 1{\times}10^{16}$ cm^{-2}, which is larger than the trap density at the grain boundary. In such a case, the potential energy barrier is given by Eq. 2.15 and, thus, is expected to decrease (effective mobility increase) with the increase in carrier concentration or decrease in trap density. Moreover, as already stated, from Eq. 2.13 and 2.14, it is deduced that a higher lateral grain size also implies a higher grain boundary effective mobility. The layers containing Zn-In-Sn-O appeared to be amorphous and, thus, grain boundary scattering did not influence the electrical transport.

2.4.2.3 Other limiting mechanisms

Other scattering mechanisms that mainly affect the bulk of crystalline samples are detailed below.

Phonon scattering Phonon scattering is a limiting mechanism caused by the vibration of the crystal lattice. On the one hand, the high frequency (optical) oscillations of neighbouring ions against each other induce the creation of an electric field that scatters the charge carriers. On the other hand, lower frequency phonons (acoustic) distort the crystal lattice causing pressure waves that scatter the charge carriers. In ZnO, optical phonon scattering is much higher than acoustic phonon scattering. However, phonon scattering is negligible compared ionised impurity scattering [29, 80]. Further information can be found elsewhere [37].

Piezoelectric scattering This phenomenon occurs only in piezoelectric materials, i.e. in crystals without inversion symmetry, and is caused by the interaction of electrons with the electric field associated with acoustic phonons in the crystal [14]. Especially remarkable is the piezoelectricity of ZnO along the c-axis [94]. However, sputtered ZnO grows with the c-axis perpendicular the sample substrate. The electrical transport is measured laterally and occurs in almost all cases perpendicular to the c-axes of the crystallites [37]. Therefore, this mechanism did not affect the results obtained here. The cubic In_2O_3 lattice presents inversion symmetry and is not affected by piezoelectric scattering.

Neutral impurity scattering This scattering process is caused by the interaction of electrons with uncharged impurity atoms. In case of ZnO or In_2O_3, the scattering by neutral impurities is small since most of them are already ionised at room temperature because extrinsic dopants are shallow donors with low activation energies [37].

Dislocation scattering Dislocation scattering is the process caused by crystallographic defects found within the grains. As it happens at the grain boundaries, crystallographic dislocations lead to defects with energies within the band gap and thus they can trap and scatter charge carriers. Nevertheless, two-dimensional grain boundary scattering effects are much higher than one-dimensional dislocation scattering effects. Further information can be found elsewhere [14].

2.4.3 Electronic band structure

The optical and electrical performance of TCOs are intimately tied to the fundamental band structure of the material [100]. Transparent conducting materials are wide band gap semiconductor materials. As discussed, ZnO and In_2O_3 can easily become n-type conductors thanks to the presence of shallow donors, like crystal defects and extrinsic dopants. Owing to the high electron densities generally achieved, the Fermi level lies in the conduction band. The electronic band structure of ZnO and In_2O_3 is briefly presented below.

Zinc oxide is a direct semiconductor with a band gap energy of 3.4 eV [44, 101]. The low lying valence bands belong to Zn $3d$ states, whereas the upper valence bands are composed of O $2p$ bonding levels. The conduction band minimum is a single broad minimum formed from Zn $4s$ states [44].

The In_2O_3 band structure is comparable to ZnO. It also has a single free-electron-like conduction band minimum formed by In $5s$ states. On top of the valence band, the O $2p$ states are found followed by the In $4d$ and O $2s$ states. The minimum band gap of In_2O_3 is 2.9 eV, but it is direct and forbidden [102]. The first allowed optical transition is 0.8 eV below the valence band top [102]. Therefore, the measured optical band gap is found at 3.7 eV [44].

The n-type TCOs discussed here consist of the oxides of post-transition metals. As we have just described, the conduction band minima of these oxides are free-electron-like states localised on the metal s states. One of the main characteristics of these metal oxides is that they can be made amorphous [103] and still present good electrical and optical properties. The effect of disorder on s states is rather weak compared to p states, because of their spherical symmetry. Thus, the only source of disorder is the variation of the metal-metal distance, and angular disorder has no effect on s states. Thanks to the s-like conduction band minima, higher electron mobilities can be achieved, in comparison to other amorphous materials such as silicon.

The work function (Φ) of a material is the energy difference between the Fermi energy and the vacuum level (see Fig. 2.6). This energy corresponds to the minimum amount of energy needed to remove an electron from the material. The work function strongly depends on the surface conditions. The presence of contamination or the occurrence of surface reactions can

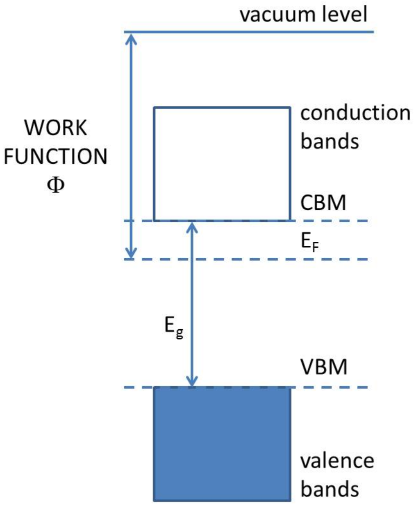

Figure 2.6: Schematic energy diagram of a semiconductor.

considerably modify the work function. These modifications are a result of the formation of electric dipoles at the surface. These dipoles lower the energy that an electron needs to leave the sample, i.e. the work function.

The work function of the TCO films plays a crucial role in determining the electron (or hole) injection energy barrier height between the TCO film and the semiconductor [104, 105]. In case of organic photovoltaics, high work functions are needed to optimise the open circuit potential and to facilitate the charge injection by the organic layer [100].

2.5 Application: silicon thin film solar cells

One of the goals of developing TCOs is to improve the performance of thin film silicon solar cells. In this section, the operation principle and the role of the TCO into the different kinds of configurations will be briefly described.

A solar cell is an optoelectronic device that converts sunlight into electric power. A semiconductor device receives a photon and uses its energy to excite an electron from the valence to the conduction band leaving a hole

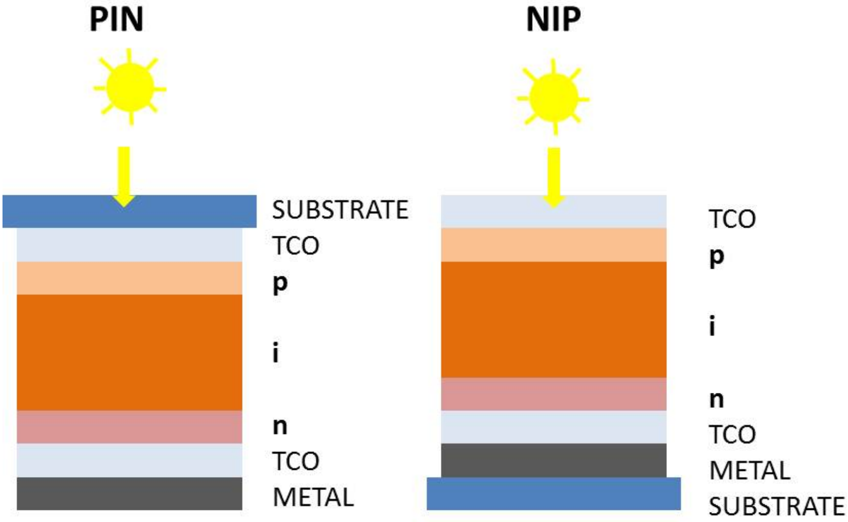

Figure 2.7: Schematic diagram for a single junction thin-film solar cell in *pin* and *nip* configuration.

behind. The electron-hole pair is separated by means of an electric field. Afterwards, the electron and the hole have to be collected by means of two selective electrodes before they recombine. The electrode located at the front side of the device has to be transparent to allow the sunlight to go through it. Besides, it should be a good conductor to avoid electrical losses. Whereas the active part of the device is the one converting sunlight into electric power, the electrodes are considered a passive part.

Thin film silicon solar cells are a low-cost alternative to crystalline silicon (c-Si) since the cost to produce a device is much lower. Thin film solar cells are fabricated from the beginning by the random nucleation and growth process of individually condensing/reacting atomic/ionic/molecular species on a substrate [106]. Not only the deposition methods are simpler but also the thickness of the active layers is drastically lower. However, the conversion efficiencies of single-junction devices achieved so far are below those of c-Si as pointed out in the introduction of this thesis.

Two different configurations are used when a thin film silicon solar cell is fabricated: the *pin* and the *nip* (See Fig. 2.7). The difference between them is the order used to deposit the layers. In both cases, the light enters the bulk of a solar cell through the *p*-type layer. Given that most of the carriers are photo-generated at the front part of the cell and that the hole mobility is lower in comparison to the electron mobility, the *p*-layer is preferably located at the front side and, thus, holes travel shorter distances before they reach the electrode.

In case of *pin* solar cells, a transparent front contact is necessary, and it is firstly deposited over the glass. The TCOs generally used are boron [107] or aluminium doped ZnO [108] and SnO_2 doped with fluorine [109]. On the contrary, the *nip* solar cells transparent contact is deposited on top of the whole device. In such a case, ITO is generally used. The Zn-In-Sn-O multi-compound studied throughout this thesis could replace the front contact ITO in *nip* solar cells. When the TCO is deposited over a device, higher restrictions appear given that the temperature can not be freely risen, and the deposition conditions should not damage the underlying layers.

Furthermore, another TCO is generally used at the back side of the device to enhance the reflectance when not absorbed light reaches the rear contact. The existence of a reflector allows the fabrication of even thinner active layers. The back reflector TCO will be deposited on top of the device in *pin* structures but will be the first deposition step after the metal layer in *nip* configurations. In this thesis, only the *pin* configuration was used and the suitability of ZnO:Al and ZnO:Ga were proven.

Although Fig. 2.7 shows a stack of flat layers, solar cells are generally deposited on rough electrodes [108] to enhance light trapping and, thus, increase the photogenerated current.

Thin film silicon solar cells are divided into two categories: the amorphous and the microcrystalline silicon type. The difference lies in the structure of the material. In case of amorphous silicon, there is a lack in long range order but in microcrystalline silicon, crystalline grains of the order of several nanometers are embedded in an amorphous matrix. This difference also results in distinct band gaps of the material which implies that a different part of the solar cell spectrum can be absorbed. Whereas amorphous silicon has a quasi-direct band gap of 1.7-1.8 eV, μc-Si:H has an indirect band gap of 1.1 eV, similar to that of c-Si. The smaller band gap of μc-Si:H allows the absorption of a larger portion of the solar spectrum down to 1100 nm.

The advantage of using a-Si:H is the high absorption coefficient, which allows the use of thin layers. Hydrogen is used to passivate the large amount of dangling bonds present in an amorphous silicon layer. Some of these bonds degrade under illumination and the efficiency of a-Si:H devices decreases. This effect is known as Staebler-Wronski [110]. On the contrary, μc-Si:H does not present such a big effect since the amorphous fraction is smaller. The drawback of μc-Si:H lies in the indirect band gap of the material that leads to lower absorption coefficients in comparison to a-Si:H and thus, thicker layers (1.5 μm) are necessary.

The combination of a top cell of a-Si:H with a band gap of 1.7 eV and a bottom cell of μc-Si:H with a band gap of 1.1 eV leads to an optimum stacked tandem solar cell [111]. This *micromorph* concept allows to achieve thin film silicon solar cells with higher conversion efficiencies. The challenge with this structure is to increase the photogenerated current in both cells while keeping the top absorber thin to avoid light induced degradation. Moreover, the current of both cells should match with each other given that they are connected in series, and the lowest current limits the device performance.

3 Experimental

In this chapter, the experimental details used for the development of the thesis are detailed. Firstly, in Sec. 3.1, the working principle of magnetron sputtering, which is the deposition technique mostly used throughout this thesis, is carefully described. The equipment, the power sources used and the homogeneity of the resultant layers are detailed. Given that other deposition techniques were used for the fabrication of solar cells and post deposition treatments were performed on TCOs to improve their properties, the working principle and equipment details are briefly pointed out in sections 3.2 and 3.3 respectively. To study the morphology, structure or the optical and electrical properties of the resulting layers and devices, diverse characterisation techniques were needed. In Sec. 3.4 the systems used are enumerated and shortly described.

3.1 Magnetron sputtering

Magnetron sputtering was the technique used throughout this thesis to deposit the different transparent conducting oxides. Sputtering refers to the deposition by means of ejecting atoms from a solid target owing to the impact of high energy species [57]. A schematic diagram of the process is given in Fig. 3.1. A radio-frequency (rf) or direct current (dc) glow discharge is ignited between a cathode (the target) and an anode (substrate and chamber walls) in a vacuum environment where a noble gas, like argon, has been introduced. The process starts with the ionisation of Ar atoms (Ar^+). The electrons are accelerated towards the anode whereas the positively charged ions are accelerated towards the cathode colliding with other neutral atoms on its way. If their kinetic energy is greater than the gas ionisation energy, new ions are formed. Then, the atmosphere consists of a mixture of ions, electrons and neutral gas atoms. A self-sustaining plasma glow discharge is formed as long as the pressure and electric potential are maintained in an appropriate range, which varies

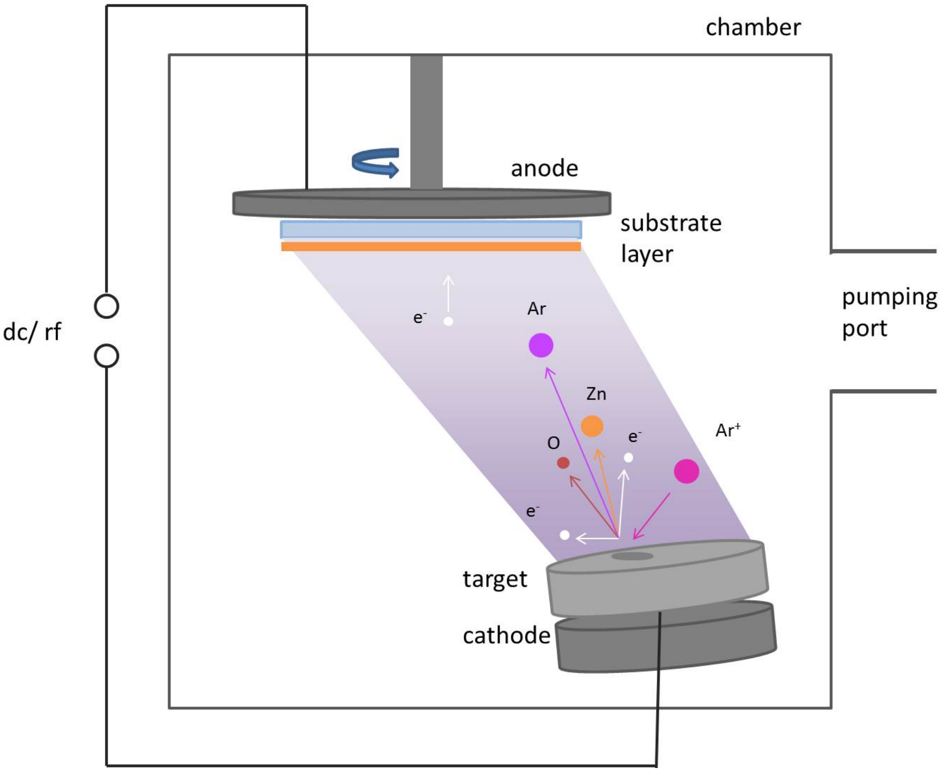

Figure 3.1: Schematic diagram of the sputtering process.

depending on the kind of power source and target used. If the ions colliding the cathode (target) have enough momentum, target atoms are ejected in vapour phase. In this low pressure environment, condensation occurs under concurrent bombardment by energetic species, which promotes nucleation, compound formation and film growth onto the substrate and the chamber walls [112, 113].

The efficiency of this process was dramatically increased by the magnetic confinement of charged plasma particles next to the target when the *magnetron sputtering* [114] was applied. A higher amount of collisions take place and, thus, more argon ions are created. As a result, higher deposition rates are achieved. With a higher localised plasma density, the chamber pressure can be reduced, and the mean free path of the neutral particles also increases.

For metal oxides, thin films can be prepared either by sputtering from a metallic target in an oxygen rich environment (reactive sputtering) or directly from ceramic targets. Although it is cheaper to deposit TCO layers by reactive sputtering, this work was developed by using ceramic targets, which was a simpler process given that the metal-to-oxygen ratio was defined by the target stoichiometry.

3.1.1 Description of the equipment

The balanced magnetron sputtering equipment used was a commercially available *ATC-ORION 8 HV* system from *AJA International, Inc.*, which handles samples up to 10 × 10 cm^2. It consisted of a 34.7 cm in diameter and 39.8 cm height chamber with 3 different magnetron guns. A schematic diagram of the sputtering system can be found in Fig. 3.2.

The chamber was pumped down and reached a base vacuum as low as 1×10^{-5} Pa, by a dry primary pump and a high vacuum turbomolecular pump ($500\,\mathrm{l\,s^{-1}}$). Nevertheless, the base pressure normally reached before each deposition was between 1×10^{-3} Pa and 5×10^{-4} Pa. It should be taken into account that no load lock chamber was used.

Each magnetron sputter gun can host targets of 7.62 cm (3 inch) in diameter. The guns are 3^o tilted and located 10 cm off-axis of the substrate. Substrate holder can rotate between 0 and 20 rpm in order to obtain homogeneous layers. The composition of the different targets used and their purity is described in each corresponding section. The distance between the substrate and the targets could be varied between 11.7 and 18 cm.

Either rf (300 or 600 W) or dc (750 W) adjustable power sources could be applied to the cathodes through three magnetron sputtering sources. It is worth noting that the dc source was acquired during this thesis and could not be used for most of the studies presented here. By using two sources simultaneously, co-sputtering could also be performed as shown in Fig. 3.2.

Substrates were heated from the backside of the substrate holder by three halogen lamps, which can reach a maximum temperature of 800°C. Ar and O_2 gas flows were adjusted by two different mass flow controllers limited to 20 sccm. During the sputtering process, the pressure was regulated by

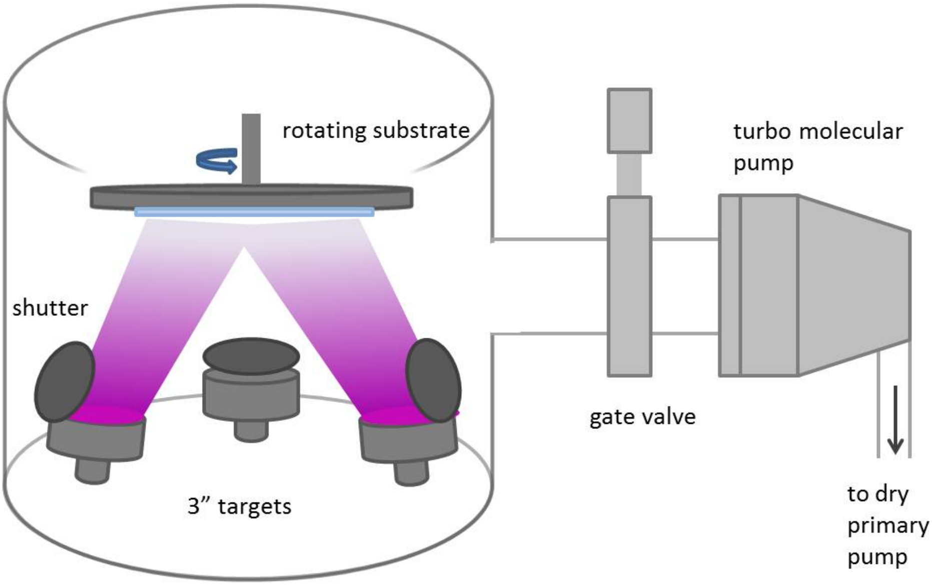

Figure 3.2: Schematic diagram of the sputtering chamber.

a three position gate valve.

The targets were protected by metallic chimneys and shutters to avoid cross-contamination when using neighbouring targets. In order to avoid arc discharges caused by the detachment of material deposited at the chimney walls, it was very important to keep them clean. After several depositions or before changing the target material, the chimneys were removed and cleaned by sand blasting. Before using them again, they were rinsed with acetone and isopropanol and heated in an oven at temperatures above 100ºC.

The chamber was also periodically cleaned, specially after sputtering of metallic targets, which enhanced the detachment of the material deposited at the walls. In this case, the chamber was rinsed with diluted hydrochloric acid, acetone and isopropanol in a tedious and time consuming process followed by a baking process at high temperature.

The process conditions used at UB varied for each material and each series of samples. Therefore, they are detailed in the corresponding section.

During the internship at FZJ, the layers were deposited by rf magnetron sputtering from planar ceramic targets in an in-line sputtering system *VISS 300* by *VAAT*. The dimensions of the planar targets were 75 × 10 cm^2 and consisted of ZnO:Al_2O_3 with 1 wt.% Al_2O_3. Depositions were always performed at a substrate temperature, pressure, discharge power and argon flow of 330°C, 0.1 Pa, 1.5 kW, and 50 sccm, respectively. The layers presented a thickness around 800 nm and a sheet resistance between 3.0 and 3.4 $\Omega/\square$. Further details on the equipment used at FZJ can be found in [115].

3.1.2 Direct current and radio-frequency sources

Both dc and rf sources were used for the deposition of TCO layers. In case of dc sputtering, positive gas ions are deposited on the target surface. When the target is conductive, the positively charged ions are neutralised by electrons at the cathode. If not, a charge that counteracts the electric field would be build causing arcing or even a plasma stop because charged particles are no longer accelerated by the electric field. Alternating the electric field, like in rf, makes the electrons to be drown to the cathode neutralising the charged ions. Moreover, the rf voltage can be coupled through any kind of impedance so that electrodes do not need to be conductors [57]. The rf target self-biases to negative potentials and it behaves like a dc target given that electrons are more mobile than ions and can easily follow the periodic change in the electric field [57].

In the past, rf sources were needed for dielectric targets such as ZnO:Al, but since high density and homogeneously conductive targets are fabricated, dc sources can also be used for TCO deposition. When targets presenting nonconductive inclusions are used, arcing and nodule growth appear on the target surface. Low density targets exhibit worse film properties due to contamination with different species [37].

Both dc and rf excitation modes lead to different ionisation mechanisms and thus, to different potential discharge distributions. Therefore, each excitation mode implies a different energy of the ions and sputtered species. The discharge voltage, i.e. the negative dc voltage measured at the target, is lower for rf compared to dc [116]. The dc sputtering is based on the generation of ion-induced secondary electrons ejected from the target. Then, large target voltages are needed to sustain the plasma given that to obtain high electron emissions, high ion velocities are needed. Instead, rf sputtering is driven by ionisation due to electrons which perform oscillations in the plasma body. Whereas electrons follow the rf, ions cannot owing to the higher inertia. Although the excitation is much more effective for rf mode, the movement of the electrons also hinders the magnetic confinement and then, lower deposition rates are obtained. Moreover, in case of rf, a higher plasma density is found next to the substrate [55]. Such a plasma density may cause some trouble when sputter deposition is done over a solar cell structure.

3.1.3 Homogeneity of the deposited films

The films deposited with the sputtering equipment showed quite a good thickness homogeneity (5-10% variation from centre to border) onto 10 × 10 cm^2 substrates for such a small (3 inch) off-axis targets. The equipment was prepared to use relatively large target to substrate distances (between 11.7 and 18 cm), which allowed the deposition of these highly homogeneous layers. Adjusting the distance, in between the allowed range, could improve the homogeneity for each deposition condition.

In Fig. 3.3, the relative thickness variation from center to border of 10 × 10 cm^2 layers deposited under the same conditions but different target to substrate distances is shown. The substrate position which showed the least variation was the 15.5 cm. Therefore, this distance was generally chosen for the layer deposition unless otherwise specified.

3.2 Other deposition techniques used

3.2.1 Plasma enhanced chemical vapour deposition (PECVD)

PECVD is the most commonly used technique for the deposition of hydrogenated amorphous and microcrystalline silicon thin film solar cells. It is a glow discharge technique in which a plasma of the reactive gases is created between two parallel discharge plates at an excitation frequency of 13.56 MHz. The gases react within the plasma, and some of the resulting species condensate on the substrate forming a film.

Amorphous silicon solar cells fabricated at UB were deposited in a multichamber reactor in cluster configuration from *Elettrorava*. The equipment

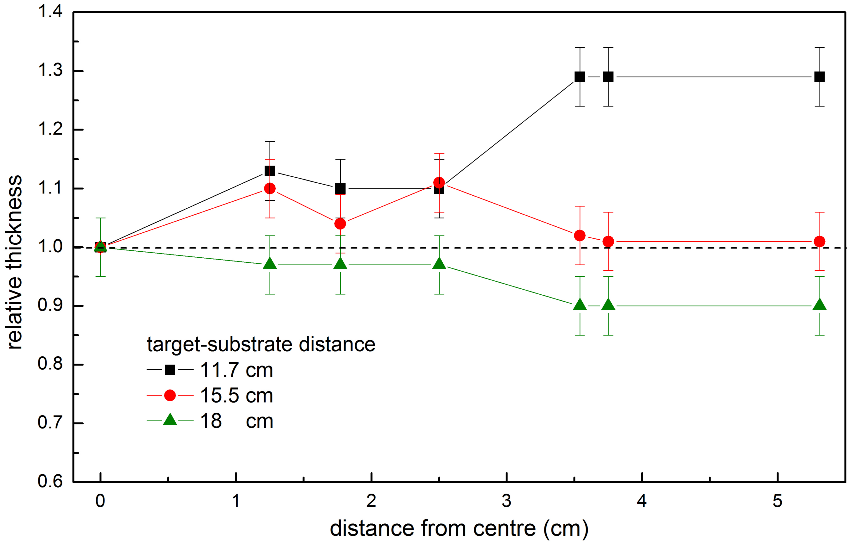

Figure 3.3: Relative thickness variation from center to border of 10 × 10 cm^2 layers deposited under the same condition but using different target to substrate distances.

consists of two chambers for PECVD and a loading and transfer chamber. Information about the deposition of thin film solar cells by means of PECVD can be found elsewhere [117].

Amorphous silicon layers were also deposited on top of ZnO:Al before annealing at FZJ. The deposition conditions of silicon were as follows: a power of 4 W for an electrode area of 35 × 35 cm^2, a substrate temperature of 200°C, a deposition time of 5 min (3.3 min in case of i-layer), an electrode to substrate distance of 12 mm and a pressure of 160 Pa. The flows used to deposit the n-type layer of hydrogen, silane and phosphine were of 100, 50 and 20 sccm respectively. For the p-type layer, the flows of hydrogen, silane, trimethylboron and carbon dioxide were of 90, 9, 5 and 5 sccm respectively and for the i-type layer the flows of hydrogen and silane were of 200 and 20 sccm respectively. Additional details on the deposition system can be found in [118].

3.2.2 Thermal Evaporation

A thermal evaporation equipment (*Veeco VE-400*) was used for the deposition of metal layers, at the back reflector of *pin* type solar cells. Aluminium rods were put into tungsten helical filaments and silver rods into tantalum or molybdenum boats. Current flowed through the containers achieving temperatures above the material melting point (660°C for Al, 961°C for Ag). The substrate holder was 15.5 cm above the boat or helical filament, and the pressure was kept below 10^{-2} Pa preventing the substrate temperature to rise dramatically and the melted material to collide with air particles before reaching the substrate where the material condensates. Quartz crystal thickness monitor was used to control the thickness during deposition. To define the size and shape of the contacts, specific metallic shadow masks were used.

3.3 Post deposition treatments

3.3.1 Reactive ion etching (RIE)

Before depositing back reflectors on amorphous silicon structures not deposited at UB, the removal of the native oxide layers was tried by means of RIE. Moreover, the etching of amorphous silicon capping layers used to anneal ZnO:Al at high temperatures was needed in order to characterise the layers optically. In both cases, a dry reactive ion etching process was performed using different gases.

The RIE technique is an etching method performed using a rf plasma and specific etchant gases. The plasma is generated with an electromagnetic field under low pressure conditions, and the high energy ions etch the surface. The physical bombardment caused by the ions sputters any material. By choosing a proper etch gas, a chemical reaction takes place on the sample surface increasing the etch rate and thus achieving a higher selectivity for a certain substance [119].

The RIE was performed with a *Plasmalab 80* from *Oxford Instruments* which allows using gases like Ar, O_2, Cl_2, HBr, BCl_3 and CHF_3.

3.3.2 Thermal annealing

Thermal annealing of ZnO layers was performed in order to modify the electrical and optical properties of the TCO layers. Therefore, a pipe oven that allowed the annealing of samples up to 10 × 10 cm^2 was used at Forschungszentrum Jülich. The cylindrical oven (50 cm long, 15 cm in diameter), which was a *FRH 150/250/1100 Linn high term GmbH*, was able to work in vacuum, air or nitrogen atmosphere reaching temperatures as high as 1100°C.

The annealing procedure under vacuum consisted in introducing the layer in a quartz oven and pumping it down to 10^{-3} Pa. In the case of nitrogen annealing, the chamber was first evacuated, then, a flow of 5 $\mathrm{l\,min}^{-1}$ was established until 1×10^5 Pa was reached, and finally nitrogen was pumped down again before annealing started. In the case of air annealing the samples were directly introduced into the oven.

3.4 Characterisation techniques

3.4.1 Thickness measurements using a surface profiler

A mechanical surface profiler (*Dektak 3030, Veeco*) equipped with a 25 μm diameter stylus was used for the film thickness determination. A simple lift-off technique combining ink and acetone was used to create steps on the deposited films. The steps could be lately measured using the stylus profiler. The vertical resolution of the equipment was of 1 nm. The associated error was of ± 10 nm, which was the standard deviation of a set of measures taken at the same point.

3.4.2 Structural analysis

3.4.2.1 X-ray diffraction (XRD)

The crystallographic orientation of the layers was measured by XRD technique. The principle consists in focussing an X-ray beam on the sample with an angle θ and measuring the angles of diffraction of the scattered beam (see Fig. 3.4). The atoms cause the incident beam of X-rays to diffract into many directions. When Bragg's law is verified (Eq. 3.1), constructive interferences are formed, and an intensity peak is measured [120].

$$2d_{hkl}\sin\theta = n_x\lambda \tag{3.1}$$

In Bragg's law, d_{hkl} is the distance between the lattice plane, λ is the X-ray wavelength, n_x is the diffraction order and θ is the angle between the X-ray beam and the samples surface.

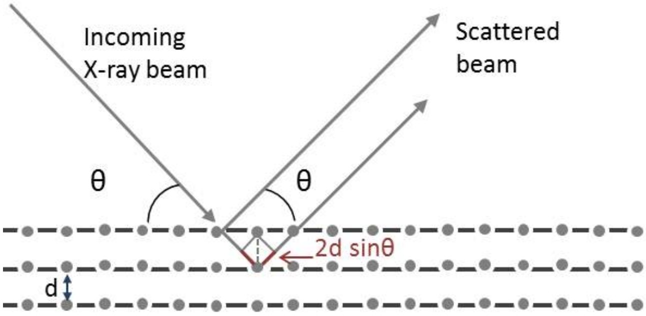

Figure 3.4: Schematic diagram of the θ-2θ configuration for XRD measurements.

The X-ray diffractometer employed during this study was a *PANalytical X'pert PRO MPD Alpha1* used in Bragg-Brentano geometry ($\theta - 2\theta$ scans).

By analysing the diffraction patterns, the crystallographic orientation and axis lengths can be estimated from the resulting peaks positions (2θ). The full width at half maximum (FWHM) can be directly obtained from the peak profile. The crystallite size (D) and the average width of the microstrain distribution (e) can be semi-quantitatively deduced from the broadening of the adjusted pseudo-Voigt function to the diffracted peaks. The simple, single-line approach used in this thesis to obtain D and e, was first presented in [121], and it is reviewed in [122]. In this approach, the diffraction line is conceived as a convolution of a gaussian and a lorentzian (also called Cauchy) function, i.e. as a Voigt function, where the gaussian component is related to microstrain, and the lorentzian component is related to the finite crystallite size [122]. The estimation of the crystallite size D (volume-weighted domain size in the direction perpendicular to the diffracting lattice planes) and of the width of the microstrain distribution

e in the diffracting volume is possible using the following equations:

$$\beta_L = \frac{\lambda}{D\cos\theta} \tag{3.2}$$

$$\beta_G = 4e\tan\theta \tag{3.3}$$

where λ is the X-ray wavelength, 2θ is the Bragg angle, β_L is the breadth of the lorentzian component and β_G is the breadth of the Gaussian component. β_L and β_G were obtained by XRD peak profile fitting with *WinPLOTR* [123] software.

It should be taken into account that the method used is a qualitative approach useful to compare different samples within a series. Absolute values cannot be taken into account since XRD is sensitive to any crystallographic defect. Most of the studies performed onto similar samples by other authors attribute the whole breadth of the diffracted peak to the existence of a finite grain size. They calculate the grain size by means of the Scherrer formula [29, 124]. Here, a second assumption has been taken into account by attributing part of the breadth of the diffracted peaks to microstrain. Further details can be obtained in [121].

Once the distance between adjacent lattice planes (hkl) is obtained from the diffracted peak position (Eq. 3.1), the lattice constants can be calculated taking into account the crystal system. When a hexagonal crystal system is observed, such in the case of ZnO, the lattice parameters a and c can be calculated following Eq. 3.4. The unique diffracted peak measured for the sputtered ZnO samples studied in this work corresponded to (002) planes, where h=0, k=0 and l=2. Therefore, only c (twice d_{hkl}) could be obtained as deduced from the following equation:

$$\frac{1}{d_{hkl}^2} = \frac{4}{3}\left(\frac{h^2+hk+k^2}{a^2}\right) + \frac{l^2}{c^2} \tag{3.4}$$

A change in the diffracted peak position implies a change of the lattice parameter (Eq. 3.1). When the calculated lattice parameter is compared to the standard lattice parameter of the material, the deformation (also referred to as strain) of a crystal lattice in a macroscopic scale can be qualitatively deduced. In case of ZnO, by comparing the obtained c parameter to the standard reported value [38], it can be determined whether the lattice suffers a compressive (bigger c) or tensile stress (smaller c) [120, 125].

3.4.2.2 Transmission electron microscopy (TEM)

TEM is a microscopy technique whereby an electron beam is transmitted through an ultrathin layer. High resolution TEM (HRTEM) is an imaging mode of TEM that is used to obtain an image of the crystallographic structure of a layer at an atomic scale.

In this technique, electrons interact with the specimen and are afterwards focussed and magnified forming a high resolution image [126]. In order to obtain ultrathin layers of TCO material for cross section images, two pieces of the sample were sandwiched by the sample side facing each other with a glue. Then it was mechanically polished until the stack was 30 μm thick and finally slimmed with an ion bombardment system. The tedious and time consuming preparation procedure had to be carefully done to avoid breaking the sample. The equipment used was a high resolution transmission electron microscopy *JEM JEOL 2100*. The selected area electron diffraction patterns and high resolution images of the samples were analysed with *DIFPACK* and *Digital Micrograph* softwares.

3.4.3 Compositional analysis and chemical state

3.4.3.1 X-ray photoelectron spectroscopy (XPS)

The XPS technique consists in focussing an X-ray beam onto a material surface and counting the emitted electrons as a function of their kinetic energy. The electrons proceed from the outer layers of the different atoms which form the material and the kinetic energy can easily be converted into the corresponding binding energy of the material. Given that it is a quantitative technique, it allows to determine the elemental composition of the studied material, i.e. identifies the species and its stoichiometry. Furthermore, the kinetic energy of the emerging electrons gives information about the chemical state of the bonded species when comparing the values with standard data sheets. Further explanations about the technique as well as binding energy data can be found in reference [127].

The equipment used was a *PHI 5500 Multitechnique, Physical Electronic* at UB and a *SPECS GmbH* at the University of South Florida. The position of the carbon 1s peak is taken as a standard (binding energy, 284.8 eV) to compensate for any charge-induced shifts. The *Multipak*, *IGOR pro* from *(Wavemetrics, Inc)* and *Origin 8.0* softwares were used to treat the resulting data.

3.4.4 Optical characterization

3.4.4.1 UV-VIS-NIR spectrophotometer

The transmittance and reflectance of the samples were measured with either a *Perkin Elmer lambda 19* or *Perkin Elmer lambda 950.* Both systems were equipped with an integrating sphere, which enabled the distinction between the specular, total (T) and diffused (T_d) transmittance and reflectance (R) by means of using different configurations (see Fig. 3.5). The system, equipped with a deuterium and a halogen lamp, was able to measure the transmitted or reflected light between 200 and 2500 nm. For all the measurements, unless otherwise specified, samples were oriented with the glass facing the incident light as it would happen in a solar cell.

3.4.5 Electrical characterisation

3.4.5.1 Four point probe

The resistivity of thin films was obtained by means of a *JANDEL RM3* four point probe station. The system was used to measure the sheet resistance (R_s) of the layers, and it consisted of four in-line probes of tungsten carbide spaced 1 mm apart. Only very thin films (from 10 up to 1000 nanometre thick) can be measured with this equipment.

The station was first laid onto the surface of the sample, and then, a small electric current I was applied between the two external probes whereas the resulting voltage drop V was measured between the two internal probes. The current could be adapted between 10 mA and 1 μA. This range allowed to measure samples with sheet resistances between 1 and 10^7 $\Omega/\square$.

From the applied current and measured voltage, the sheet resistance can be calculated according to equation:

$$R_s = \frac{V}{J}\frac{\pi}{ln2} \tag{3.5}$$

Afterwards, the resistivity can be obtained by multiplying the sheet resistance by the film thickness.

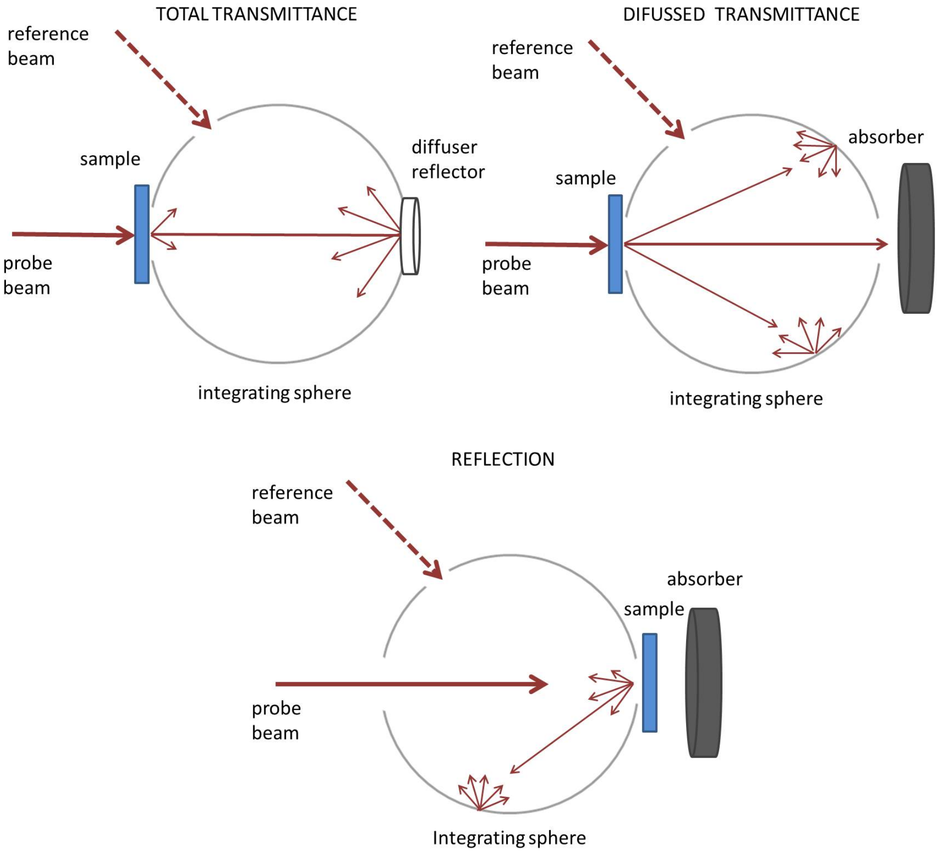

Figure 3.5: Schematic diagram of the spectrophotometer configurations used to measure the transmittance, diffused transmittance and reflectance with an integrating sphere.

3.4.5.2 Hall effect measurement

Hall effect measurements were performed to determine the mobility (μ), carrier concentration (n) and resistivity (ρ) of the deposited layers. Samples were cut into 0.5 to 1 cm squared pieces and small metallic contacts were soldered by means of an ultrasonic soldering system (*MBR Electronics USS-9210*) using *Cerasolzer 186* alloy. The four contacts were located at the edges of the sample.

The Hall effect refers to the appearance of a voltage V_H that is established along the y-axis when an electrical current I, flows through the sample in the x-axis direction while a magnetic field B, is applied perpendicularly along the z-axis. Because of the B, the moving charge carriers will be deflected towards the sides by the induced Lorentz force. As a consequence, the majority charge carriers will accumulate at one side of the sample, creating a potential difference between the two opposite sides. This Hall voltage can be expressed as:

$$V_H = \frac{IB}{nq_e d} \tag{3.6}$$

where I denotes the current thorough the sample, B the magnetic field strength to which the sample is exposed, n the free carrier concentration, q_e the elementary charge and d the thickness of the layer. By using the Van der Pauw configuration, it is possible to determine μ, n and resistivity ρ, irrespectively of the samples geometry [128]. During Hall effect measurements, the sample holder was placed in a magnetic field of 0.3 T generated by two parallel coils. The electric current intensity used was always the lowest one which ensured measuring the Hall voltage difference with three significant figures. If the film thickness is known, n can be determined by measuring the Hall voltage. The resistivity can also be found by using the Van der Pauw method as described in [128]. From the measured resistivity and free carrier concentration, the mobility can be calculated according to:

$$\mu = \frac{1}{q_e n \rho} \tag{3.7}$$

3.4.5.3 Electronic band structure measurements

Work function (WF) and valence band maximum (VBM) were measured by means of photoemission spectroscopy at the University of South Florida in a commercial ultra high vacuum multi-chamber system *(SPECS GmbH)*. The analysis of the photoelectrons was performed with a *SPECS Phoibos 100* hemispherical analyser.

Ultraviolet photon spectroscopy (UPS) measurements are the standard way to characterise the work function of surfaces since absolute values can be obtained with this technique. UPS refers to the measurement of the

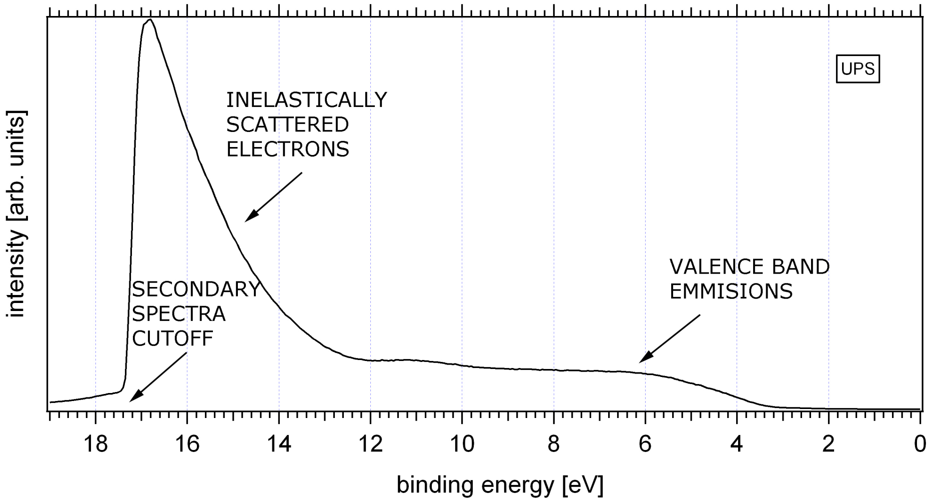

Figure 3.6: Typical UPS spectra of an ITO layer.

kinetic energy spectra of photoelectrons emitted from the surface of an UV irradiated material. The kinetic energy (KE) of the emitted electrons is given by:

$$KE = h\nu - BE - \Phi_S \tag{3.8}$$

where $h\nu$ is the energy of the incident photon, BE is the binding energy of the atomic orbital from which the electron originates, and Φ_S is the spectrometer work function.

Fig. 3.6 shows a typical UPS spectrum of an ITO sample. The Fermi level is located at 0 eV binding energy, just when photoemission begins given that the first occupied levels appear. The slope that starts at around 3 eV corresponds to the valence band maximum. Further to the left, the emissions correspond to the valence bands. At binding energies of 12 eV onwards, it can be observed the inelastically scattered electrons, which were initially emitted from the valence bands states, but lost energy through scattering processes on their way to the sample surface. Then, the high binding energy cutoff (or secondary edge) can be found. The electrons, which are close to the edge, are the slowest ones of the spectrum. Concretely, after leaving the sample surface they have zero kinetic energy. They just had the energy needed to overcome the work function of the material [129]. Given that we know the binding energy of the electrons at the secondary edge, we can determine the WF, which is just the difference between the energy of the UV photons (21.21 eV for He I radiation) and the binding energy of the secondary edge [129].

Recent research demonstrated that UPS measurements on metal oxide surfaces can result in a lowering of the work function caused by the measurement itself [130–133]. Therefore, the samples were also characterised with low intensity X-ray photon spectroscopy (LIXPS), which was performed before and after each UPS measurement to obtain the work function and to investigate the occurrence of UV induced work function lowering during UPS measurements.

During LIXPS measurements, the X-ray gun is operated in stand-by mode resulting in a photon exposure orders of magnitude lower compared to XPS or UPS, while still allowing the measurement of a well resolved secondary edge for the work function determination. This enables the determination of the work function of the sample prior to UV exposure during UPS measurements. During UPS and LIXPS measurements a -15 V bias voltage was applied to separate sample and analyser spectral cutoffs. The spectrometer was calibrated to yield the standard Cu $2p_{3/2}$ line at 932.66 eV, and Cu $3p_{3/2}$ at 75.13 eV. More details of the technique are described in [132].

Spectral analysis was done using *IGOR pro* software *(Wavemetrics, Inc)* where work function values were obtained by determining the intersect of secondary edge with the baseline of the spectra. 0.1 eV was added to account for the analyser broadening [134].

3.4.6 Solar cell characterisation

3.4.6.1 Current density-voltage measurements

Solar cell characteristics were determined by measuring the current as a function of voltage while cells (typically ~ 1 cm^2) were illuminated by a *New Port 67005* xenon lamp provided with a global air mass (AM 1.5) filter. The beam was focussed towards the entrance of an optical fibre that addressed the light to the measuring stage. Before each measurement, a

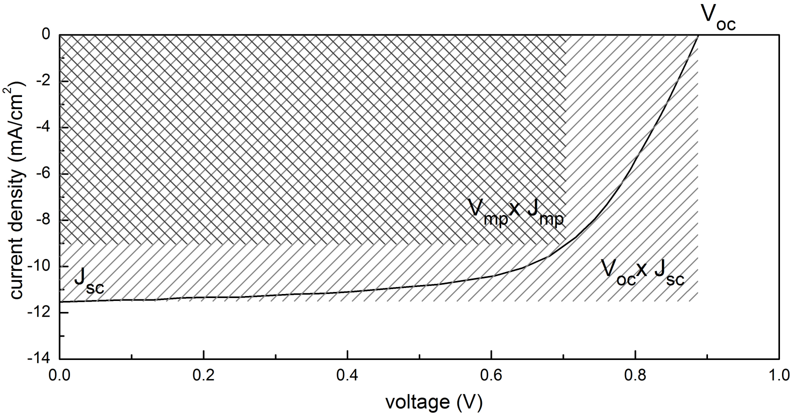

Figure 3.7: Typical solar cell curve for current density as a function of voltage under illumination.

well known standard cell was characterised in order to control the incident power of the light source. The measurements were performed at a cell temperature of 25°C.

From the measured current density-voltage curve, the short circuit current density (J_{sc}) and open circuit voltage (V_{oc}) can be obtained when voltage or current is zero respectively. A typical measurement can be found in Fig. 3.7.

The fill factor (FF) is related with the form of the J-V curve. It is the ratio between the maximum power density ($V_{mp} \times J_{mp}$) and the product of V_{oc} by J_{sc} (ratio between the two shaded rectangles in Fig. 3.7).

The cell efficiency can be calculated from the J-V curve by dividing the maximum power by the incident power. It gives the fraction of incident power which is converted into electricity.

The J-V curve of an a-Si:H or a μc-Si:H solar cell can be described by means of an equivalent circuit (Eq. 3.9) which consists of a parallel circuit of a single diode and a voltage dependent current generator $J_{ph}(V)$, plus parallel and series resistance, R_p and R_{sr} respectively [29].

$$J = -J_{ph}(V) + J_0 \left(exp\left(\frac{q_e(V - JR_{sr})}{n_i k_B T} \right) - 1 \right) + \frac{V - JR_{sr}}{R_p} \qquad (3.9)$$

where J_0 is the saturation current density, q_e is the electron elementary charge, n_i is the ideality factor, k_B is Boltzman's constant and T the absolute temperature. R_p and R_{sr} are parasitic resistances that reduce the solar cell efficiency by dissipating power in the resistances. The J-V curve measured under illumination gives information about these resistances because, in most cases, the parasitic resistances reduce the fill factor.

3.4.6.2 External quantum efficiency (EQE)

The EQE is the number of electrons produced in a solar cell per incident photon in short circuit condition. It is a measure of the electrical sensitivity of the solar cell to the wavelength of the incoming light. It was measured with a set up assembled at UB, which used a *Spex 1680* monochromator. The spectral range between 350 and 800 nm was examined in 10 nm increments.

The spectral response (SR) is given by the ratio between the photogenerated current and the incident power spectral density. The EQE is related to SR as follows:

$$SR(\lambda) = EQE(\lambda)\frac{\lambda q_e}{hc} \tag{3.10}$$

where q_e is the electron charge, λ the incident light wavelength, h Planck's constant and c the speed of light in vacuum.

It was possible to get the short circuit current density of the whole solar cell by integrating the product of the spectral response and the AM 1.5 photon flux spectrum. Given that the illumination used to measure the J-V curve at UB was not from a certified lamp for the standard characterisation of solar cells, the short circuit current density obtained from the EQE was more reliable.

4 Aluminium doped zinc oxide: influence of the deposition conditions and thermal treatments

The target of this thesis is to optimise the properties of transparent conducting oxides to use them as front contacts or back reflectors in thin film hydrogenated amorphous silicon solar cells. Aluminium doped ZnO is one of the mostly used TCOs thanks to the abundance of the raw materials [31, 55]. The deposition conditions used to obtain the ZnO:Al layers compromise the properties of the resulting films [68]. However, when ZnO:Al layers are deposited on top of already deposited silicon films, a good interface needs to be created and, thus, the conditions cannot be freely chosen, i.e. the deposition temperature cannot be above the temperature used to deposit the silicon layers, and high discharge powers or too low pressures can damage the interface. Instead, when the TCO is deposited on glass, high temperatures, and discharge powers or low pressures can be chosen to obtain layers with the best electrical and optical properties.

During this thesis, the properties of ZnO:Al were studied to understand how the material changed with the deposition parameters. Specifically, the dependence of the sputtered material with substrate temperature (Sec. 4.1.1) and deposition power (Sec. 4.1.2) was analysed and is presented in this chapter. Moreover, the properties of ZnO:Al after high temperature annealing under capping layer are discussed in this chapter (Sec. 4.2).

4.1 Influence of the deposition parameters.

The properties of ZnO:Al layers depend strongly on the deposition parameters. Here, the dependence on substrate temperature and delivered power to the target is presented. Other influencing parameters would be the deposition pressure [135], the plasma excitation frequency [136], the doping concentration of the target [115] and the deposition time, i.e. the layer thickness [137]. The nature of the substrate used also modifies the initial growth of the layer and, thus, its properties [138]. Increasing the substrate temperature does not change the plasma conditions during deposition but gives the ability for the incoming particles to diffuse along the surface or into the bulk [39]. By increasing the power delivered to the target, higher sputtering yields are achieved [139].

The properties of two series of samples deposited by rf magnetron sputtering using different substrate temperatures and rf powers are presented in this section. The films were deposited onto 10 × 10 cm^2 *Corning* glasses (1737F) at a pressure of 0.4 Pa in a pure argon gas atmosphere. The ZnO:Al target (2 wt.% $\mathrm{Al_2O_3}$) had a purity of 99.9%. The base pressure in the chamber was always below 2.7×10^{-4} Pa. The target to substrate distance was kept at 15.5 cm, and a substrate rotation of 10 rpm was used to achieve uniform composition in the films during the sputtering. In the following sections, the influence of both parameters, discharge power and substrate temperature, are presented.

4.1.1 Substrate temperature dependence

In order to study the influence of substrate temperature during deposition, the substrate temperature was varied from 21°C, which corresponds to no intentional heating, to 420°C. The layers were deposited at a constant rf power of 150 W. The deposition time was controlled to achieve a layer thickness of 200 ± 20 nm for all the films. The morphological, optical, and electrical properties will be detailed below.

The deposited films onto 10 × 10 cm^2 substrates presented a variation in thickness over the whole area below 10%. Deposition rate increased with the increase in temperature from 3 $\mathrm{nm\,s^{-1}}$ for films deposited with no intentional heating to 3.7 $\mathrm{nm\,s^{-1}}$ for films deposited at 420°C as it can be seen in Fig. 4.1. Although it was not a large increase, a raising tendency over the whole temperature range was observed.

The X-ray diffraction spectra in Bragg-Brentano geometry showed a hexagonal wurtzite structure with the *c*-axis predominantly oriented perpendicular to the substrate surface. The spectra exhibited a (002) peak at

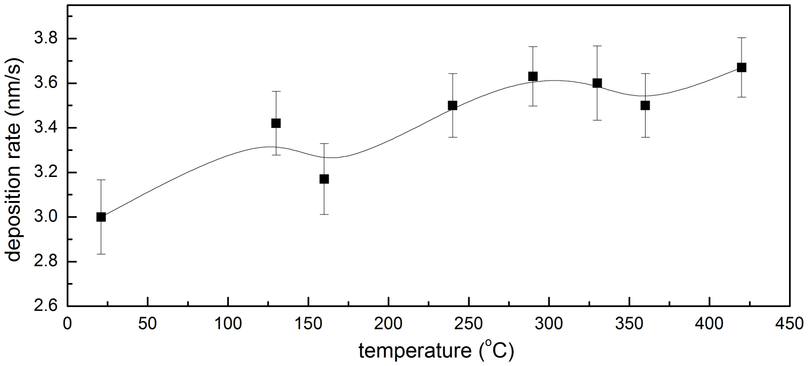

Figure 4.1: The deposition rate of ZnO:Al thin films deposited with different substrate temperatures. Line is added to guide the eye

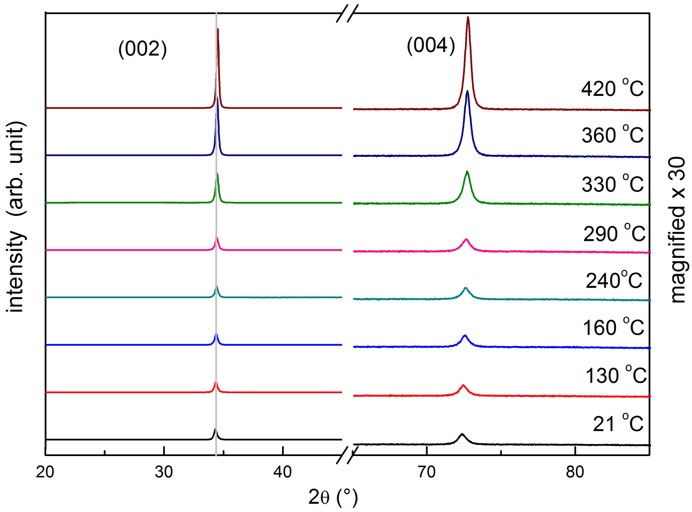

Figure 4.2: XRD patterns of ZnO:Al thin films deposited at different substrate temperatures. A line is added at the (002) maximum intensity position of the 21°C layer to help in the observation of the shift towards higher angles with the increase in temperature. The second part of the spectra where the (004) peak can be found is 30x magnified for a better observation.

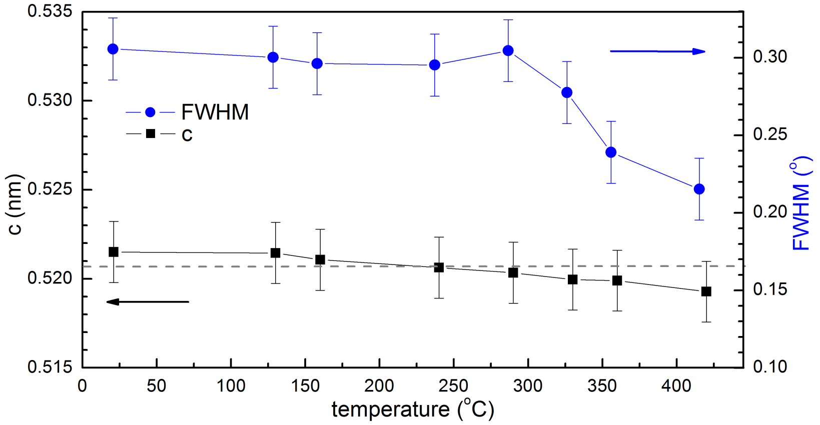

Figure 4.3: The FWHM (circle) and the lattice parameter c (square) of the ZnO:Al samples deposited at different substrate temperatures. The value of the standard lattice parameter c (0.5207 nm [38]) is marked with a grey dashed line. Lines connecting data points are added to guide the eyes.

around 34.4° as well as its second order diffraction (004) at around 72.4°. Given that c-axis growth posses the minimum surface energy [60], it dominates the growth according to the *survival-of-the-fastest* growth process [59]. No phases related to Al_2O_3 or metallic Zn could be observed, owing to the relatively small amount of extrinsic doping, or to the fact that Al^{3+} is substitutionally replacing Zn^{2+} sites. Fig. 4.2 shows the aforementioned spectra for the set of substrate temperatures characterised in this section. The (002) peak intensity increased with temperature, and, thus, enhanced the c-axis orientation. This feature was attributed to the increase in the ability of incoming particles to diffuse along the surface or into the bulk, and it was in accordance with the earlier studies [140].

Small shifts in the position of (002) and (004) peaks are revealed in Fig. 4.2. The (002) diffracted peak increased monotonically from 34.36° for the sample deposited at room temperature to 34.51° for the film deposited at 420°C. The position of the (002) peak was used to calculate the lattice constant c, which is plotted in Fig. 4.3. As the substrate temperature increased, the lattice parameter c decreased showing values below the ZnO standard value (0.5207 nm [38]). Below 200°C, c was higher than the

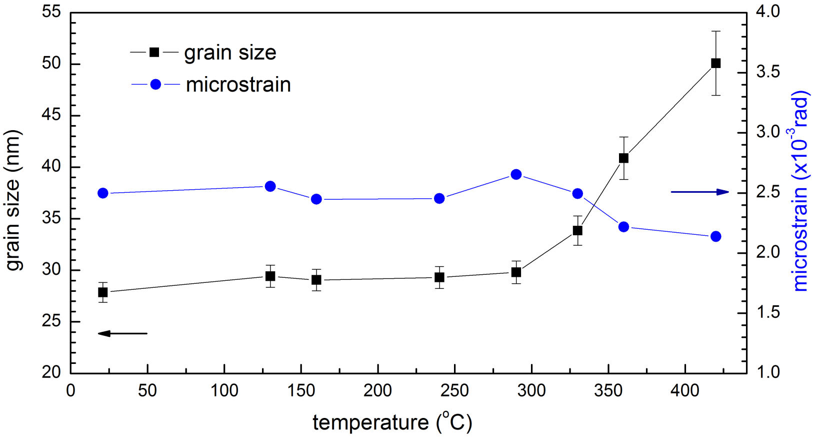

Figure 4.4: The variation of the average grain size D (square) and microstrain e (circle) of the ZnO:Al thin films deposited at different substrate temperatures Lines connecting data points are added to guide the eye.

standard value, which suggested that the lattice suffered a macroscopic compressive strain, whereas, above 200°C, c was below the standard value pointing to an increase in tensile strain (Sec. 3.4.2.1) caused by the increase in substrate temperature.

The FWHM of the (002) peaks is also presented in Fig. 4.3. The different samples showed similar values until the substrate temperature reached 300°C and then the FWHM decreased monotonously. A lower FWHM was associated with an improvement in film quality given that it means a higher number of coherently scattering crystal planes [120]. The improvement of the crystal quality could be due to both, a higher crystal size or a lower microstrain within a single crystallite. To differentiate between the crystallite size and the microstrain, the gaussian and lorentzian part of the integral breadth (β_L, β_G) were deduced from the pseudo-Voigt peak profile fitting of the XRD spectra. The average crystallite or grain size in the direction perpendicular to the diffracting lattice planes (i.e. vertical grain size) D, and the average microstrain in the diffracting volume e were calculated as described in Sec. 3.4.2.1. The evolution of these parameters can be observed in Fig. 4.4.

The grain size was estimated to be around 30 nm until 300°C and then

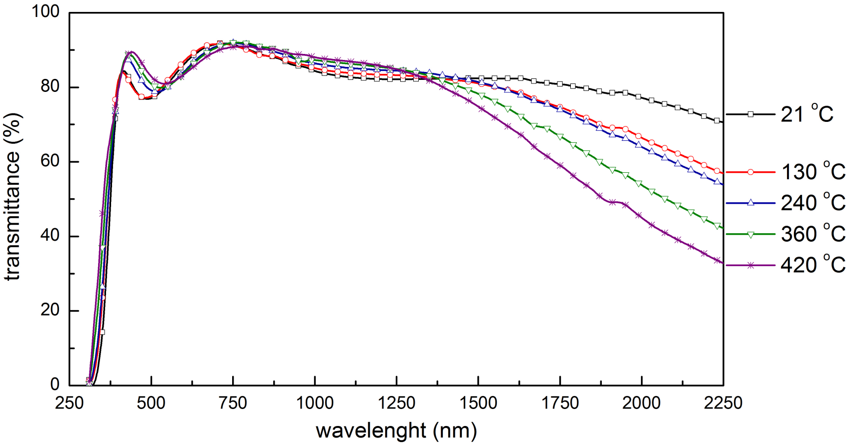

Figure 4.5: The transmittance curves of ZnO:Al thin films deposited at different temperatures. Only a few curves have been shown for a better clarity.

increased with temperature until it reached 50 nm at 420°C. Since XRD is sensitive to any crystallographic defect, including both intrinsic and extrinsic doping, small vertical grain sizes compared to those directly observed elsewhere [39] were found. Even though, the average grain size is an indicator of the crystal quality of the layer.

The microstrain in the diffraction volume showed a constant tendency with values between 2.1×10^{-3} and 2.6×10^{-3} rad. The nearly constant behaviour of the microstrain with the increase in temperature indicated that thermal stress did not significantly contribute to modify the amount of local lattice distortions. It also pointed out that the variation in FWHM above 300°C was mainly owing to an increase in crystallite size.

All the investigated ZnO:Al films showed a similar integrated transmittance, with averaged values above 85.4% in the visible range (400 to 800 nm) and above 85.0% in the near infrared range (800 to 1200 nm). In both ranges, the integrated transmittance slightly increased with temperature till 86.2% for the visible range (400 to 800 nm) and 88.2% for the near infrared range (800 to 1200 nm) at 420°C. Just five out of eight transmittance curves have been plotted in Fig. 4.5, for better clarity of the graph. In the ultraviolet part of the spectra, a steep drop can be observed due

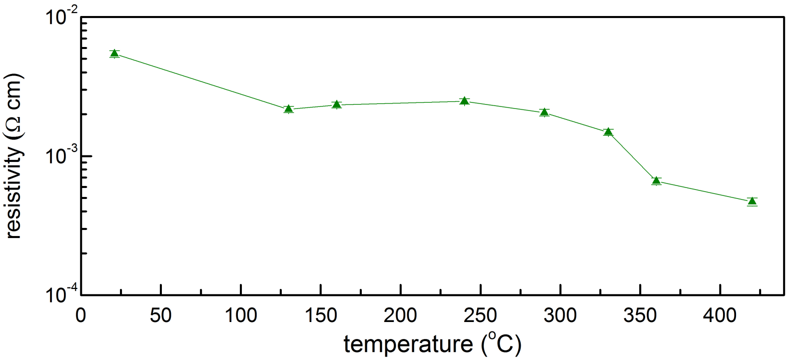

Figure 4.6: Resistivity values of the set of ZnO:Al samples deposited at different temperatures. Line is added to guide the eye.

to optical band gap absorption [14]. Moreover, absorption by free carriers arose with the increase in substrate temperature in the near infrared zone. The higher the temperature, the higher the absorption, observed in the NIR. However, the plasma edge did not affect the range below 1100 nm, which is the transparent window needed for μc-Si solar cells.

Fig. 4.6 presents the resistivity of the ZnO:Al films deposited at different substrate temperatures. Increasing the substrate temperature decreased the resistivity from $5.4\times10^{-3}\ \Omega\,\mathrm{cm}$ at room temperature to $4.7\times10^{-4}\ \Omega\,\mathrm{cm}$ at 420°C. As temperature increased and, thus, the incoming particles had a higher energy to form a more compact layer [68], the resistivity decreased. The most remarkable drop in resistivity was measured for a substrate temperature of 300°C and higher. This drop in resistivity coincided with the increase in the average grain size.

To evaluate the origin of the improvement in electrical properties, mobility and carrier concentration were measured by means of Hall effect. Results are shown in Fig. 4.7. The charged carrier concentration n increased with temperature till it reached $3.71\times10^{20}\ \mathrm{cm}^{-3}$ at 420°C, whereas the mobility μ varied with temperature reaching the highest value (37.5 $\mathrm{cm}^2\mathrm{V}^{-1}\mathrm{s}^{-1}$) at 420°C.

For carrier concentrations below $3\times10^{20}\ \mathrm{cm}^{-3}$, grain boundary scattering plays the crucial role in limiting the electrical transport [94]. In such a mechanism, the lateral grain size, the trap density at the grain boundaries

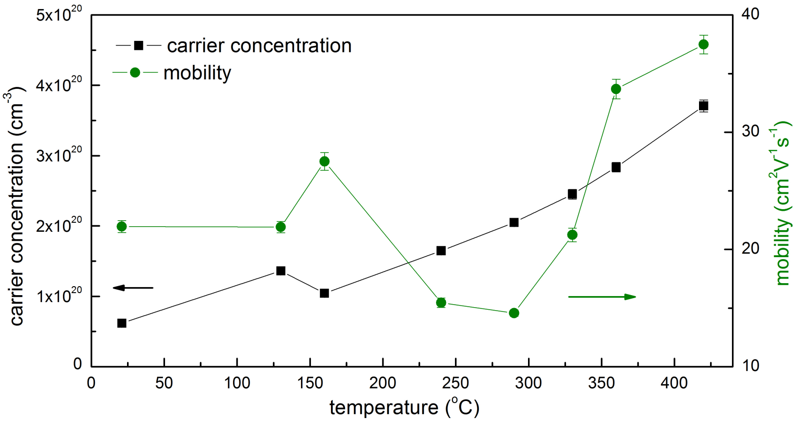

Figure 4.7: The variation of carrier concentration and mobility of the ZnO:Al thin films deposited at different temperatures. All the lines are added to guide the eye.

and the carrier concentration influence the resulting mobility. As measured from XRD, vertical grain sizes increased with temperature, specially above 300°C, but lateral grain sizes were not measured. However, from the modified Thornton model [68] it is expected that at high temperatures, grain boundaries can recrystallise, and grains with larger lateral sizes are formed [97]. Although it cannot be measured, fewer trap densities could also be expected at higher temperatures given that the compactness of the layer is expected to increase with temperature [68], and, thus, less defects can be chemisorbed at the grain boundaries. Last, as observed in Fig. 4.7, the carrier concentration increased with temperature. Layers with larger grains and lower defects use to be those where the more efficient doping takes place, i.e. the substitutional build-in of the Al dopant into zinc lattice sites is more effective [55]. Given that the grain barriers were expected to be lower because of the lower trap density and the higher grain sizes, also more carriers could account for conduction. The aforementioned observations are consistent with the higher mobility found here.

Mobility is reported to increase with film thickness [58, 141]. Given that the studied layers were just 200 nm thick, higher grain sizes and thus, mobilities, could be expected if layers were more thicker.

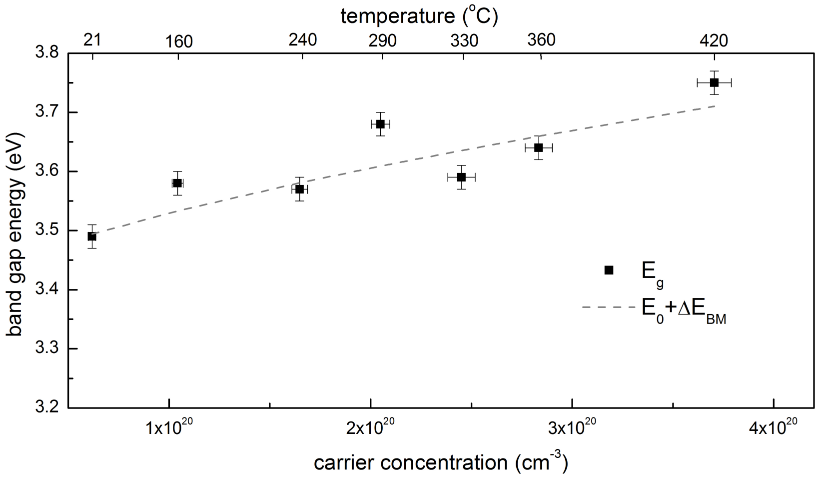

Figure 4.8: Band gap against carrier concentration. Substrate temperature can be read in the upper part of the graph. The line corresponds to the fundamental band gap (E_0 =3.4 eV) plus the Burstein-Moss effect.

The absorption coefficients and the optical band gap energies were determined from the transmittance and reflectance spectra by means of Eq. 2.4 and 2.5. The calculated values of band gap energies of the ZnO:Al films deposited at various temperatures are shown in Fig. 4.8. The band gap energy showed an increasing tendency with the substrate temperature reaching 3.75 eV for the film deposited at 420°C.

The increase in carrier concentration justified the band gap widening, which was attributed to the Burstein-Moss effect [74, 75]. In case of degenerately doped materials, as the amount of free carriers increases, the Fermi level moves towards higher values because the energy required to activate an electron from the valence band to the conduction band is higher than the fundamental band gap. In Fig. 4.8 it can be observed the plot of the carrier concentration against the band gap of the sample. Moreover, the curve observed in Fig. 4.8 corresponds to the Burstein-Moss shift expected for each carrier concentration. It was calculated as detailed in Sec. 2.3.1. The band gap curve extracted using the carrier concentration taking into account the Burstein-Moss effect fits well to the band gap values estimated from the optical measurements. No effect corresponding to the band gap narrowing was observed.

The higher the temperature, the higher the absorption, observed in the NIR wavelength range in Fig. 4.5. This effect was also associated to the higher carrier concentration found when substrate temperature increased. The carrier density determines the position of the plasma frequency (Eq. 2.12). The higher the concentration, the lower the wavelength of the absorptance peak and, thus, the measured transmittance is reduced.

4.1.2 Dependence on the deposition power

Magnetron sputtering is a plasma process which delivers a high energy input to the growing film [142]. In order to tailor the film properties, one has to adjust the energy input onto the substrate. The external deposition parameters, such as discharge power, influence the potential distribution and hence the particle energy [55]. The influence of the delivered power to the sputtering cathode was studied through a series of ZnO:Al layers deposited with an increase in rf power from 60 to 350 W. The power range corresponds to a power density between 1.3 and 7.7 $\mathrm{W\,cm^{-2}}$. The films were deposited at a substrate temperature of 160°C. All the depositions were done for a constant deposition time of 45 min, except for the layer deposited at 60 W, which was sputtered during 30 min. The optical, electrical and morphological properties were published in [143] and will be detailed below.

The deposition rate was found to increase considerably and proportional to the power till 250 W and then it kept on increasing but at a lower rate near to saturation as shown in Fig. 4.9. Given that the deposition time was constant, the thickness also increased with power. A 30 nm layer was obtained for a power of 60 W, whereas 400 nm were achieved at 350 W (Fig. 4.9). This difference in thickness made more difficult to extract the influence of discharge power of the sputtered samples given that for ZnO, the thickness also plays a crucial role [137, 141]. Both parameters, the discharge power and the thickness, will be taken into account in the discussion of the layer properties.

The deposition rate is determined by the energy of the ions at the sputtered target [55]. It was previously reported, for rf sputtering [55], that deposition rate was proportional to the discharge power as long as pres-

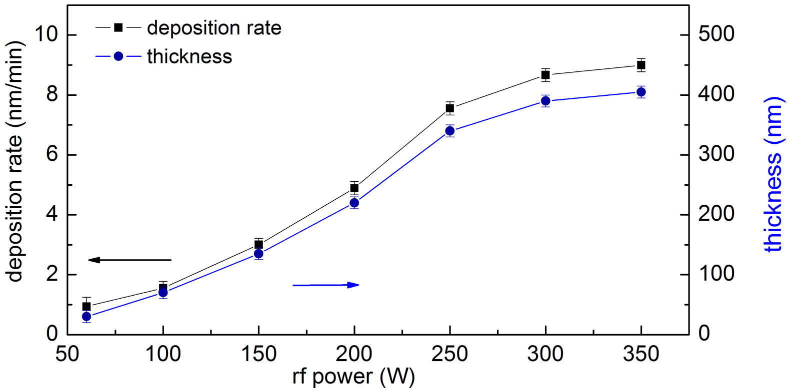

Figure 4.9: The deposition rate (square) and the thickness (circle) of ZnO:Al thin films deposited at different rf powers. Lines are added to guide the eye.

sure was kept constant. Moreover, the deposition by means of rf sputtering implies the existence of a significant ion current next to the substrate and thus a plasma density prone to re-sputter the deposited material [55]. Above 250 W, the power density at the substrate is high and probably re-sputtering of the material took place limiting the deposition rate.

X-ray diffraction patterns of the ZnO:Al films grown by rf magnetron sputtering at various discharge powers are shown in Fig. 4.10. The samples showed a diffraction peak at around 2θ =34.4° and an additional second peak of lower intensity at 72.4°. The first peak at 34.4° corresponds to the (002) plane and the second one at 72.4° to the second order diffraction (004). This implied a hexagonal wurtzite structure having a strong preferred orientation along the [001] direction with the c-axis perpendicular to the substrate surface. Increasing the power and; thus, the thickness of the layers led to an increase in the intensity of the diffraction peaks as it happened with the increase in temperature (Sec. 4.1.1). No change in the preferred orientation was observed with the increase in power. From the XRD spectra, the lattice parameter c, the full width at half maximum, the average crystallite size, and the microstrain were estimated as detailed in Sec. 3.4.2.1.

The FWHM, as well as the lattice parameter c, against the rf power are shown in Fig. 4.11. The lattice parameter was found to be quite

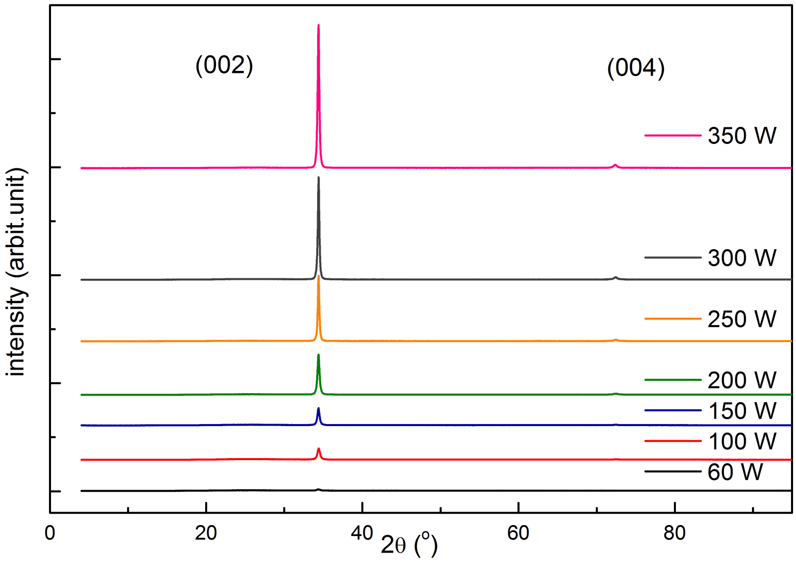

Figure 4.10: XRD patterns of ZnO:Al thin films deposited at different rf powers.

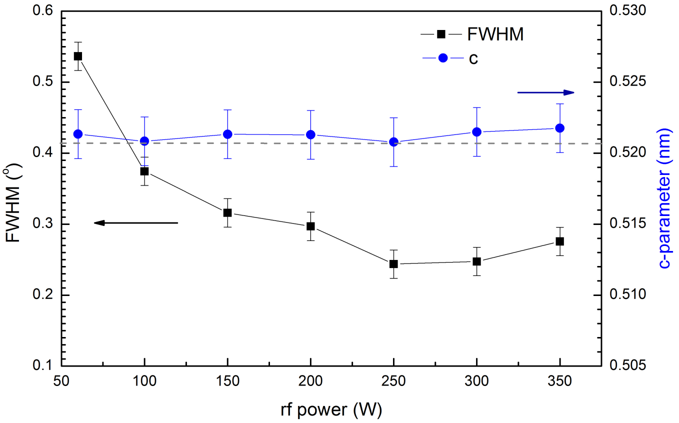

Figure 4.11: The variation of the lattice parameter *c* (circle) and the FWHM (square) of the ZnO:Al thin films deposited at different rf powers. The value of the standard ZnO lattice parameter *c* (0.5207 nm [38]) is marked with a dashed line. Lines connecting data points are added to guide the eye.

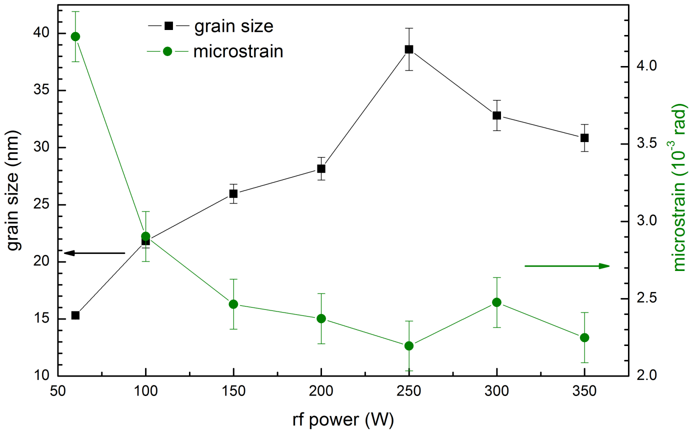

Figure 4.12: Grain size (square) and microstrain (square) as a function of the deposition power. Lines are added to guide the eyes.

near to the standard value (0.5207 nm [38]) and, thus, no macroscopic stress was detected. The same result was found for the layer deposited at the same temperature (160°C) in the previous section. The FWHM decreased monotonously till 250 W and then stayed almost constant or slightly increased again at higher powers. A lower FWHM means a higher number of coherently scattered crystal planes and thus a better crystal quality [120]. This improvement can be due to both, a higher crystal size or a lower microstrain within a grain. To differentiate between the crystallite size and the microstrain, the gaussian and lorentzian part of the integral breadth (β_L, β_G) were deduced from the pseudo-Voigt peak profile fitting of the XRD spectra as detailed in Sec. 3.4.2.1.

The grain size and the microstrain deduced from β_L and β_G are shown in Fig. 4.12. The crystallite size in the direction perpendicular to the substrate increased with power and presented the highest value of 38.6 nm at 250 W. However, further increase in rf power resulted in a slight decrease of the crystallite size. The microstrain within a grain also showed a decreasing tendency presenting the lowest value at 250 W and slightly increasing afterwards. Therefore, both D and e contributed to the FWHM behaviour. The crystal quality was improved with the increase in power, i.e

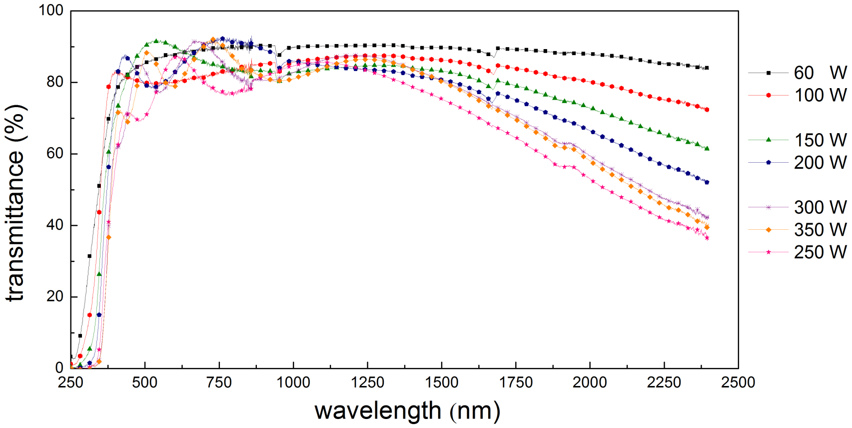

Figure 4.13: The transmittance curves of ZnO:Al thin films deposited at different rf powers.

the more energetic species arriving at the substrate enhanced the growth of bigger grains with fewer defects until 250 W. Also the increase in thickness of the layers allowed the growth of bigger grains, which could not be fitted in layers as thin as 30 or 70 nm for 60 and 100 W respectively.

The optical transmittance spectra of the ZnO:Al films grown at various rf powers are shown in Fig. 4.13. The layers showed, as expected for TCOs, a huge drop in the UV part of the spectra due to the band gap absorption. All the films were highly transparent in the visible region of the electromagnetic spectrum. The integrated transmittance was higher than 81% in the range between 400 and 800 nm and higher than 82% in the range between 800 and 1100 nm for all the samples. The highest transmittance in each range was of 86.8% and 88.9% respectively for the 30 nm thick layer deposited at 60 W. The films were thicker at higher rf powers given that the deposition time was constant, and the deposition rate grew with power. The variation in thickness ended up in a different interference scheme for each sample [76]. The lowering in transmittance in the near-infrared part of the spectra was associated to free carriers absorption.

The resistivity of the as-deposited ZnO:Al films decreased as power increased till 250 W where it showed the lowest value ($1.2 \times 10^{-3}\ \Omega\,\mathrm{cm}$).

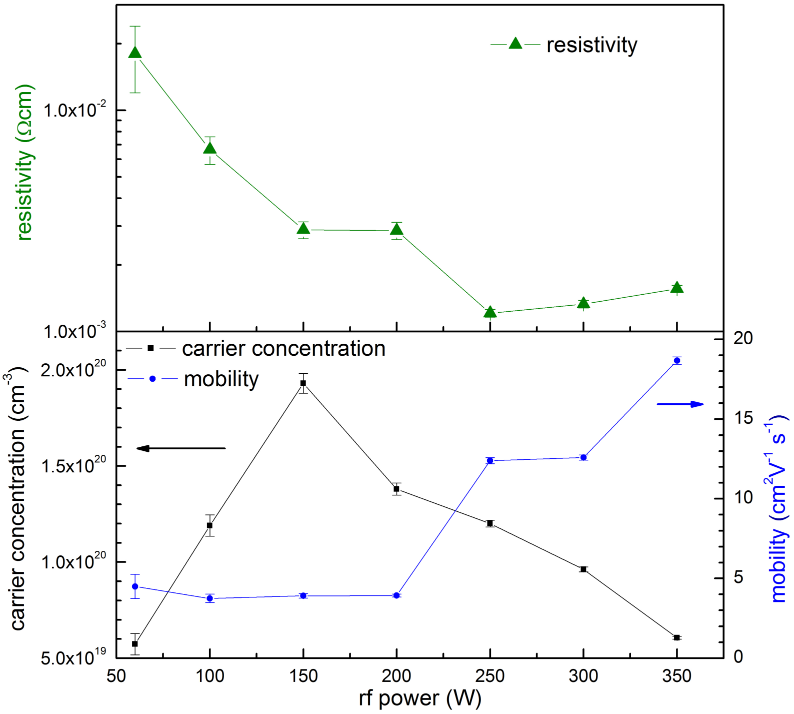

Figure 4.14: Resistivity (upper graph), carrier concentration (squares, bottom graph) and mobility (circles, bottom graph) of the ZnO:Al thin films deposited at different rf powers. Lines are added to guide the eye.

Afterwards, no significant change in resistivity was observed. The top graph in Fig. 4.14 shows the measured resistivity of the ZnO:Al films deposited using different discharge powers. This behaviour correlates with the observed trend in XRD, where the vertical grain size increased, and the FWHM and the microstrain decreased until 250 W. After 250 W, all the parameters stayed nearly constant driven by an increasing film thickness and a higher energy of the impinging particles reaching the substrate.

The values of carrier concentration and mobility are shown in the bottom graph of Fig. 4.14. On the one hand, the carrier concentration increased with the sputtering power and reached a maximum value of 1.9×10^{20} cm^{-3} at 150 W and then decreased with the increase in power. On the other hand, mobility was low at low sputtering powers, but showed a rapid increase beyond 200 W. The highest mobility of 19 $cm^2V^{-1}s^{-1}$ was observed for the films deposited at 350 W. The mobility was almost always below the values obtained with varying substrate temperatures as detailed in Sec 4.1.1.

For carrier concentrations below $3\times10^{20}cm^{-3}$, grain boundary scattering must be the limiting mechanism in electrical transport [94]. This mechanism depends mainly on the lateral grain size, the trap density at the grain boundaries and the carrier concentration.

The low mobility found at low discharge power could be ascribed to the low thickness of the layers, specially of those of 30, 70 and 135 nm. Thin layers showed small grain sizes and are more prone to content defects and voids [124], which are characteristic of the nucleation phase. Above 200 W, the mobility increased regardless the limited vertical grain size observed by XRD above 250 W. Therefore, lower defect densities at the grain boundaries might have enhanced the mobility at higher powers. However, low mobilities were measured in comparison to those obtained at high temperature for thicker layers in the previous section.

The use of low discharge powers (as 60 or 100 W) is said to result in a low Al incorporation in the ZnO lattice [61], hence, increasing the power led to an increase in carrier concentration until 150 W. However, for higher deposition powers, the carrier concentration decreased again. This effect could be due to a lower incorporation of Al^{3+} in Zn^{2+} lattice sites, to the presence of less Zn interstitials or to less oxygen vacancies. The reason is unclear and further studies would have been needed to clarify the origin of the lower carrier concentration found here.

The absorption coefficient α and the band gap energy (E_g) were determined from the absorption edge of the transmittance and reflectance by means of Eq. 2.4 and 2.5. The calculated values of band gap energies of the ZnO:Al films deposited at various rf powers are shown in Fig. 4.15 as a function of the carrier concentration. The inset shows a typical plot of $(\alpha h\nu)^2$ against $h\nu$ used for the E_g determination. The band gap values showed an increase with rf power and attained the highest value of 3.58 eV at 150 W. Beyond 200 W, the band gap decreased again. The behaviour found for the band gap is the same as the one found for the carrier concentration. This band gap broadening with the increase in carrier concentration was due to Burstein-Moss effect [74, 75]. As the amount of

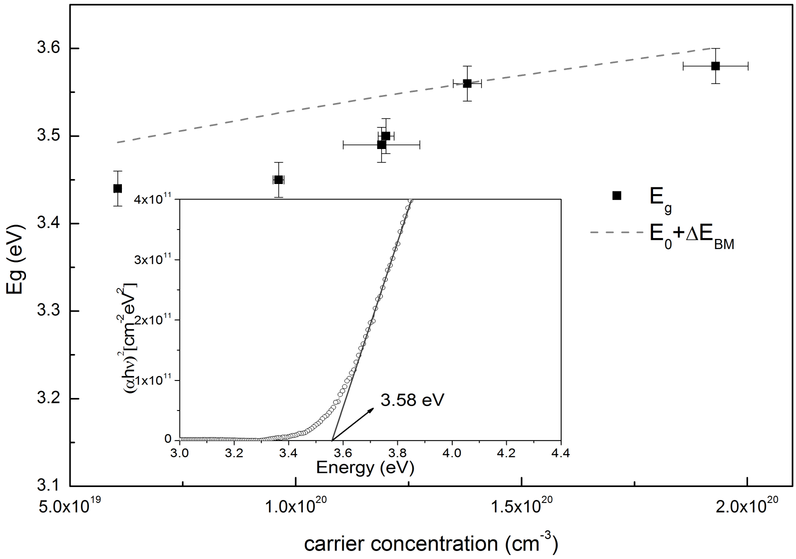

Figure 4.15: Band gap energies of the ZnO:Al films deposited at various rf powers against the carrier concentration. The line corresponds to the fundamental band gap (E_0 =3.4 eV) plus the Burstein-Moss effect. The inset shows a typical $(h\nu)^2$ against $h\nu$ plot of ZnO:Al thin film deposited at 150 W.

free carriers increases, the Fermi level of degenerate semiconductors moves to higher values because the energy required to activate an electron from the valence band to the conduction band is higher than the fundamental band gap. The band gap energies obtained, as well as the band gap values estimated from the carrier concentration, considering the Burstein-Moss broadening, can be observed in Fig. 4.15 (check Sec. 2.3.1 for further explanation). The obtained E_g values do not differ much to the fundamental band gap plus the Burstein-Moss effect, proving that it must be the reason for the widening of the band gap with the increase in carrier concentration.

Conclusions

A set of 200 nm layers deposited under different substrate temperatures were characterised. The deposition rate was found to increase slightly with temperature. By means of XRD, it was measured that the increase in temperature led to an enhanced *c*-axis orientation of the polycrystalline layers. The macroscopic strain of the layers was influenced by the temperature, which pushed the lattice parameter *c*, toward lower values. The FWHM and the grain size increased considerably for temperatures higher than 300°C. This effect was attributed to the better adatom mobility of the sputtered particles during the growth of the layer. The transmittance in the range where solar cells respond was not affected by substrate temperature. The highest integrated transmittance values of 86.2% in the VIS and 88.2% in the NIR range were found for the layer deposited at 420°C. The resistivity of the layers decreased with substrate temperature reaching 4.7×10^{-4} Ω cm at 420°C. A remarkable increase in mobility was found for temperatures above 300°C thanks to lower grain boundary barrier height. The highest mobility was of 37.5 $\mathrm{cm^2V^{-1}s^{-1}}$ at 420°C. The carrier concentration increased with temperature reaching 3.71×10^{20} $\mathrm{cm^{-3}}$ at 420°C. The latter pushed the band gap of the layers towards higher values owing to the Burstein-Moss effect.

The properties of the layers deposited with different deposition powers have been thoroughly presented and discussed. The most remarkable feature was the large increase in deposition rate (from 0.9 to 9 $\mathrm{nm\,min^{-1}}$). Given that the deposition time was kept constant, the thickness increased and, thus, also influenced the properties of the layers. The higher power and thickness led to a more pronounced *c*-axis orientation of the polycrystalline layers. The FWHM decreased, the vertical grain size increased and the microstrain decreased with the increase in power below 250 W. Afterwards, the aforementioned parameters stayed constant. The lattice parameter *c* did not change with deposition power. The resistivity decreased until it reached 1.2×10^{-3} Ω cm at 250 W. Instead, the mobility started increasing from 200 W onwards reaching 19 $\mathrm{cm^2V^{-1}s^{-1}}$ at 350 W. The mobility values obtained here were lower than those obtained for the temperature series. The integrated transmittance was higher than 81% in the range between 400 and 800 nm and higher than 82% in the range between 800 and 1100 nm for all the samples.

It has been shown that to achieve layers with higher mobilities, high substrate temperatures are needed. ZnO:Al samples deposited at high temperature are necessary to be used as the front TCO contacts in *pin* solar cells after a wet chemical etching. The wide range of deposition powers used here did not lead to electrical properties as good as at high substrate temperatures. However, the use of high deposition powers increased considerably the deposition rate, which can be beneficial for industrial applications.

4.2 High temperature annealing under capping layer

Based on works recently reported [39, 43, 144–146], a set of ZnO:Al layers were annealed at high temperatures under a capping layer. The results presented here were obtained during an internship at Forschungzentrum Jülich (Germany) and are an application of the process developed by the Helmholtz Zentrum Berlin in collaboration to Forschunzentrum Jülich. After the annealing under capping layer, higher mobilities are achieved without significant variations in the amount of charge carriers [145]. It is necessary to keep or reduce the concentration of charge carriers to avoid the influence of the plasma edge into the visible range of the transmittance. The samples used for high mobility annealing experiments were those normally used as front contact in *pin* type hydrogenated amorphous or microcrystalline silicon solar cells where lower resistivity and higher transparency of the front contact are desired to further improve the cell performance [115].

Annealing a ZnO:Al layer at high temperatures (around 400°C) in vacuum, air, argon or nitrogen normally leads to higher resistivities [147]. It is suggested that the incorporation of residual oxygen present in the ambient atmosphere reduces the mobility of the layers by chemisorption at the grain boundaries, thus increasing the grain boundary barrier height [40, 148]. Doing a thermal treatment under a capping layer is thought to protect the layer from the incorporation of oxygen [145].

Different silicon layers, as well as alumina films, were used to further investigate the influence of the capping layer. The ZnO:Al layers were deposited by rf magnetron sputtering in FZJ using the conditions detailed in Sec. 3.1.1. The annealing procedure under vacuum, nitrogen, or air atmosphere were performed as detailed in Sec. 3.3.2. Temperature was raised from room temperature to 250°C in 45 minutes and then slowly increased until 650°C in 4 hours ($1.7\ ^{\circ}\mathrm{C\,min^{-1}}$). The ramping was necessary to avoid bubble formation within the silicon capping layer. If the films were introduced directly at 500 or 600°C [149], effusion would be so fast, that would cause hydrogen accumulation, originating a bubble, which could burst breaking the silicon film [150]. After the ramp up process, the temperature was kept at 650°C for 24 hours and then the chamber was cooled down. The conditions chosen were those leading to the highest mobility reported by Ruske *et. al.* [145]. Finally, in the case of annealing under a silicon capping layer, the cap was removed by means of reactive ion etching using a mixture of CHF_3 and CF_4 reactive gases. The electrical and optical properties of the films derived from the hall and optical spectrophotometer measurements are presented in the following sections.

4.2.1 Influence of annealing atmosphere and type of silicon capping layer.

The differences in properties of the ZnO films annealed with three different capping layers, n, i or p-type a-Si:H were studied. The thicknesses of the capping layer in each case was 50 nm. a-Si:H layers were deposited as detailed in Sec. 3.2.1. The different layers were annealed in vacuum, nitrogen and air to check whether there was any influence of the annealing atmosphere. The mobility and carrier concentration, before and after annealing are shown in Table 4.1. After the thermal treatment in vacuum or nitrogen, the samples presented a lower resistivity characterised by an improved mobility regardless of the capping layer used. When samples were annealed in air, no clear trends were found. The air annealed ZnO:Al layer capped with an n-type silicon did not show an increase in mobility, whereas as an i-layer capping showed a slight increase in mobility and the p-layer capping presented a mobility as high as ZnO:Al layers annealed under vacuum or nitrogen atmospheres.

Some oxygen present in the air annealing atmosphere may had diffused through the small cracks or pores, which existed after deposition or were created during the high thermal annealing process [151]. The same cracks or pores could be present in samples annealed under air or nitrogen, but the higher concentration of oxygen in air atmosphere may have enhanced the diffusion of oxygen through the pores and, thus, the chemisorption at the grain boundaries.

The highest mobility of 68.5 $cm^2V^{-1}s^{-1}$ was obtained for an n-capped layer annealed in vacuum. It meant a 63% improvement in comparison to

capping layer a-Si:H	as-deposited	**vacuum**	**nitrogen**	**air**
	mobility ($\pm$*0.1* $cm^2V^{-1}s^{-1}$)			
n	44.5	68.5	61.0	45.3
i	42.2	62.2	62.6	55.2
p	42.8	65.6	60.1	60.8
	carrier concentration ($\pm$*0.1* $10^{20}cm^{-3}$)			
n	6.8	5.5	5.4	7.6
i	6.2	4.7	6.0	6.3
p	6.2	5.4	5.9	6.4

Table 4.1: The mobility and carrier concentration of the ZnO:Al layers capped with p, i and n-type a-Si:H layers before (as-deposited) and after annealing under vacuum, nitrogen or air atmosphere.

the mobility of the as-deposited ZnO:Al layer. The variation of the carrier concentration after annealing is minimal. The samples annealed under vacuum and nitrogen presented a slight decrease in carrier concentration whereas the samples annealed in air showed an increase.

In most of the previously published reports about this topic, a slightly higher carrier concentration was measured after annealing under capping layer. A possible explanation suggested by Ruske *et. al.* [145] and Ponomorev *et. al.* [152] was that hydrogen contained in the capping layers diffused into ZnO:Al enhancing the carrier concentration. Hydrogen, not only can diffuse into the layer but also can escape to the ambient [153]. Ruske *et al.* [145] found lower carrier concentrations, as reported in this work, when the annealing process is performed for longer duration. Given that, also here, the annealing was performed during 24 hours, hydrogen might have passed through ZnO:Al but could have escaped, slightly reducing or not affecting the number of charge carriers.

It was foreseen by Ellmer and Mientus [94] that ionised impurity scattering must have been the limiting electrical transport mechanism in ZnO for carrier concentrations higher than 3×10^{20} cm^{-3}. However, as discussed in previously reported works [43, 145], the remarkable improvement in mobility found here cannot be attributed to a change in ionised impurity scattering because the carrier concentration remained almost constant. Nevertheless, ionised impurity scattering might have slightly influenced given that, for annealed layers in nitrogen and vacuum, the behaviour found for the mobility (increasing) and the carrier concentration (decreasing) matched with the typical behaviour of ionised impurity scattering. However, the mobility improvement was too high to be only attributed to a so minimal decrease in carrier concentrations.

Instead, the mobility might have been improved thanks to a better transport across the grain boundaries. Since no important changes in carrier concentration or grain size were previously detected, Ruske *et al.* [145] and Wimmer *et al.* [43] suggested that defect density at the grain boundary (traps) must have decreased with the annealing under cap. The reduction of the trap density at the grain boundary takes place at an atomic scale and thus, no improvement in grain size was reported.

When samples were annealed in air atmosphere, a higher or equal mobility was found, but also a slightly higher carrier concentration. Therefore, it was thought that some oxygen preset in the air annealing atmosphere might have diffused through small cracks or pores present after deposition or created during the high thermal annealing process [151]. Then, in air atmosphere there could have been a superposition of two effects. First, the effect of annealing under a cap, which led to a grain boundaries healing and, thus, a better electrical transport through them. Second, the chemisorption of oxygen at some of the grain boundaries near the randomly distributed pores which, on the contrary, did not allow the mobility to increase.

As an example of the optical behaviour after annealing, the transmittance of ZnO:Al layers annealed with a *p*-type silicon capping layer are plotted in Fig. 4.16. After the thermal treatment, an improved transmittance was found. Both in the wavelength region near the band gap, and in the near infrared part of the spectra, the transmittance was improved regardless of the annealing atmosphere used. In the near infrared part of the spectra, the higher transmittance was for the layer annealed in vacuum, followed by nitrogen and then air.

Improvement in the transmission in the short wavelength occurred owing to the defect healing, which would have removed point or dislocation defects within the band gap avoiding absorption in the aforementioned region [72]. This improvement was found after annealing in nitrogen, vacuum and also in air suggesting that, also here defect healing took place.

The increase in transmittance in the near infrared part of the spectra

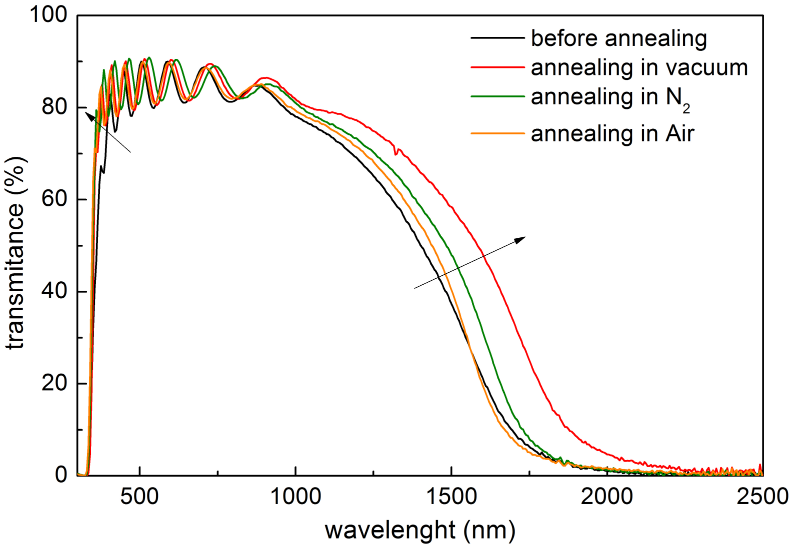

Figure 4.16: The transmittance curves of ZnO:Al before and after annealing under *p*-type a-Si:H capping layers in vacuum, nitrogen and air atmospheres.

was likely due to the improvement in the mobility which sharpened the plasma frequency absorption (Eq. 2.12). This sharpening implied a lower influence of the free carrier absorption in the visible range [145]. Although the mobility increased for the *p*-layer/ZnO:Al annealed in air, a higher carrier concentration was also observed which implied a slight movement of the plasma frequency towards higher energies (lower wavelength). Both effects were overlapped and, thus, the lowest change in transmittance is measured for the layer annealed in air atmosphere.

4.2.2 Layers capped with alumina

For the next experiment, after depositing the ZnO:Al layers at FZJ, samples were sent to TUEindhoven (The Netherlands), and Al_2O_3 was deposited by atomic layer deposition (ALD) on top of ZnO:Al. Given that highly conformal layers can be grown by ALD [154], thinner films were expected to protect compared to the thicker layers of a-Si:H deposited by PECVD. The thicknesses used were 1, 10, 25, 50 and 100 nm. Samples were

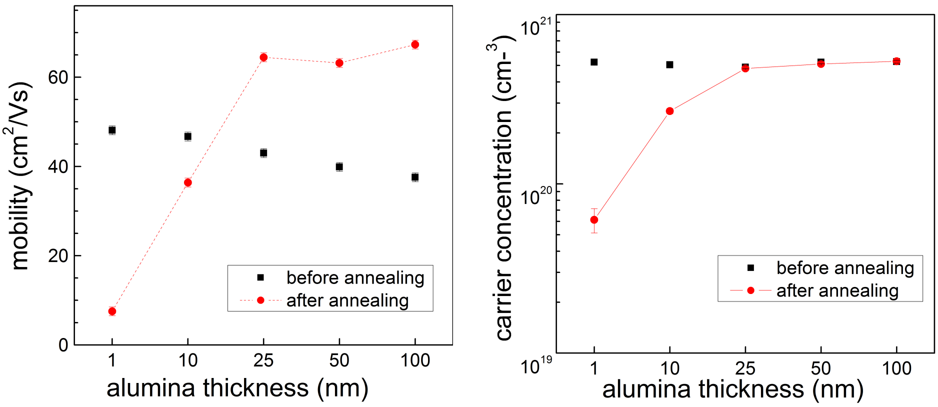

Figure 4.17: The mobility (left) and carrier concentration (right) of the ZnO:Al before and after annealing under Al_2O_3 capping layers in vacuum.

characterised before and after a standard annealing procedure at 650°C in vacuum as described above. Further details on the annealing process can be found in Sec. 3.3.2.

As it can be observed in Fig. 4.17, mobility and carrier concentration decreased with annealing for 1 and 10 nm capping layers. It can be seen that mobility decreased dramatically in case of just 1 nm Al_2O_3. In case of 10 nm Al_2O_3, the decrease was not so pronounced. For capping layers of 25 nm or thicker, the mobility was improved after annealing and showed values comparable to the values obtained after annealing under a-Si:H capping. For the 100 nm Al_2O_3 layer, the highest mobility of 67 $cm^2V^{-1}s^{-1}$ was obtained, which meant a mobility improvement of 79%. The carrier concentration decreased when ZnO:Al was covered with 1 and 10 nm of Al_2O_3, but stayed almost constant for thicker alumina layers. Therefore, a thicker alumina layer ended up fulfilling the same protective function as the a-Si:H. A similar effect with the increase in a-Si:H thickness was observed by Ruske *et al.* [145].

Moreover, a 2-4 at.% of hydrogen is reported to be deposited in Al_2O_3 layers [154] which is lower to the 16-19 at.% reported for a-Si:H with a 10 % silane concentration [155]. This fact made no difference in the behaviour of the carrier concentration in comparison to the previous experiment.

This experiment showed that a-Si:H was not the only proper film to be

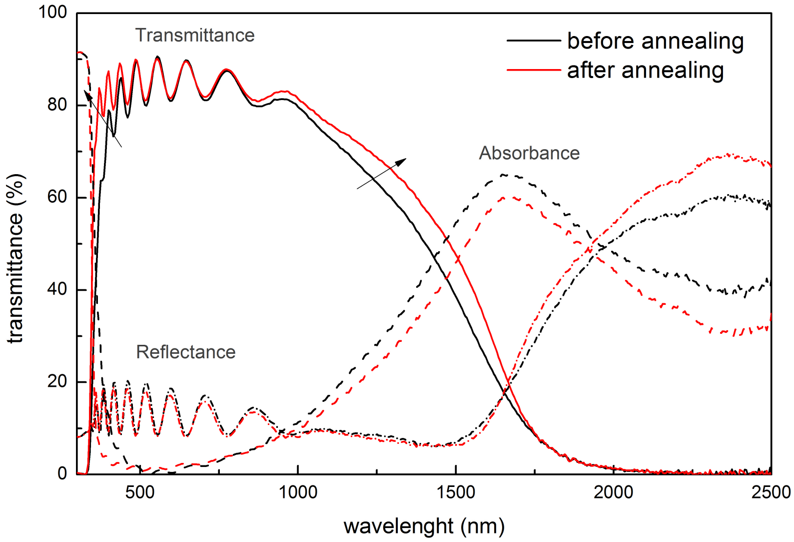

Figure 4.18: The transmittance, reflectance and absorption of ZnO:Al before and after annealing under 25 nm Al_2O_3 capping layer in vacuum.

used as a capping layer and opened the door to explore other materials. The fact that the thinner layers did not prevent the incorporation of oxygen in ZnO:Al films suggested that the 1 nm and to an extend the 10 nm Al_2O_3 presented some holes or were rather thin to allow oxygen to diffuse through them. The conformal growth of ALD did not allow thinner layers to protect ZnO:Al from atmospheric influence.

The optical properties of the ZnO:Al layers with the alumina capping layer were studied by measuring the transmittance and reflectance before and after annealing. In Fig. 4.18 the curves can be observed, as well as the absorptance calculated from Eq. 2.1. The depicted layer corresponds to the layer capped with 25 nm of alumina. The transparent window was widened with the thermal treatment. After annealing, there was an increase in transmittance in the low wavelength range (300-500 nm) as well as in the long wavelength range (800-1800 nm). As it happened for a-Si:H capping layers, the long wavelength improvement was attributed to the increase in mobility while keeping a constant carrier concentration. The maximum in absorbance was kept at the same position but had a lower intensity and a narrower breadth. The improvement in the low wavelength range was attributed to a lowering in defect density within the band gap [72].

Conclusions

The annealing in vacuum or nitrogen at 650°C under different capping layers (a-Si:H and alumina) improved significantly the mobility leaving a similar carrier concentration. Mobility values as high as 68.5 $cm^2V^{-1}s^{-1}$ and 67 $cm^2V^{-1}s^{-1}$ for ZnO:Al capped with *n*-type silicon and alumina were achieved respectively. It was observed that the minimum alumina thickness needed to achieve a higher mobility was 25 nm. The reason for the higher mobility is unclear. Even though, the healing of the ZnO:Al grain boundaries is thought to be the fact that allowed such an improvement. The transmittance was higher in both, the low and long wavelength range. This fact would reduce optical losses in the TCO of thin film silicon solar cells. A considerable improvement is expected for μc-Si:H and tandem (stack of a-Si:H and μc-Si:H) solar cells where a wider transparent region is needed. Nevertheless, the process implied a high temperature process which would be a drawback for the solar cell industry.

5 Gallium as an alternative dopant to ZnO

Most of the applications related to ZnO use aluminium as a dopant [17–19]. Nevertheless, aluminium presents a high reactivity leading to oxidation during the growth of the ZnO:Al films. Instead, gallium is less reactive and more resistive to oxidation in comparison to aluminium [23]. The closer atomic number of gallium (31) to zinc (30) in comparison to aluminium (13) suggested a better acceptability of Ga into ZnO lattice. Moreover, the covalent bond lengths of Ga-O and Zn-O are close: 1.92 and 1.97 Å [23]. The slightly smaller bond length of Ga-O in comparison to Zn-O is advantageous since it allows to reduce the deformation of the ZnO lattice even for high gallium concentrations [23]. Therefore, gallium doped ZnO was deposited and studied as an alternative to aluminium doped ZnO. The influence of pressure, doping concentration, substrate temperature and oxygen volume concentration on the resulting ZnO:Ga layers are presented in this chapter.

All the layers presented throughout this chapter were deposited by rf magnetron sputtering onto 10 × 10 cm^2 *Corning* glass (1737F). The purity of all the targets used was of 99.9%. The applied rf power, target to substrate distance and base pressure were the same for all the deposited layers studied in this chapter, i.e. 150 W, 15.5 cm and 6.7×10^{-4} Pa respectively. The deposition time was adjusted in order to obtain films of 200 ± 20 nm.

5.1 Influence of pressure on the deposition of ZnO:Ga layers

The pressure during sputtering deposition strongly influences the sputtering rate and mean free path of the sputtered particles [55]. In order to

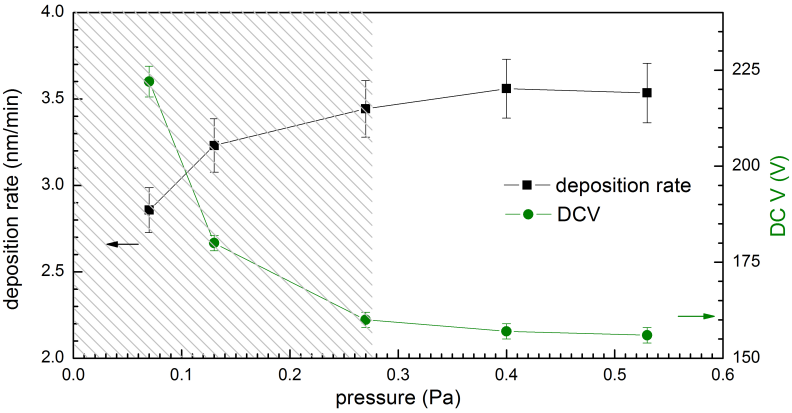

Figure 5.1: Deposition rate and measured cathode voltage of ZnO:Ga thin films at different sputtering pressures. Lines are added to guide the eyes

study the influence of pressure on the deposited ZnO:Ga films, the deposition was carried out at pressures between 0.07 and 0.53 Pa. This range is rather low compared to other publications [23, 82, 156]. The argon gas flow was kept constant at 6 sccm and the sputtering pressure was controlled by adjusting the gate valve position. A ZnO target with 2 wt.% of Ga_2O_3 was used to study the dependence of pressure onto the resulting ZnO:Ga layers. All the depositions were performed without intentional substrate heating keeping in mind the back reflector application of these layers. The morphological, optical, and electrical properties are detailed below.

The deposition rate varied between 2.86 $\mathrm{nm\,min^{-1}}$ at 0.07 Pa to 3.56 $\mathrm{nm\,min^{-1}}$ at 0.40 Pa. The time was adjusted to obtain 200 ± 20 nm layers. Fig. 5.1 shows the dependence of the deposition rate on the argon deposition pressure. An increase in deposition rate was observed as pressure increased but then remained almost constant for pressure above 0.27 Pa. The resulting cathode voltage at different pressures is also plotted in Fig. 5.1. The voltage decreased with an increase in pressure until 0.27 Pa and then it remained almost constant for higher pressures.

Depending on the deposition pressure used, different sputtering regimes can be observed. At low pressures (below 0.27 Pa in this work), the mean free electron path between collisions is large, and the electrons may reach the anode or the chamber walls without ionising Ar atoms. At low ionisation efficiencies, high target voltages are required to sustain the plasma (dashed region in Fig. 5.1) [57]. For middle range pressure (above 0.27 Pa in this work), the electron mean free path is reduced, and the Ar ionisation efficiency increased resulting in larger current flows (Fig.5.1) lower cathode voltages. In this range, the highest deposition rate is observed. A third regime could have been taken into account if higher pressures were used. In that range, electrons, ionised Ar, as well as sputtered atoms undergo many collisions resulting in an energy loss that would have reduced the ionisation efficiency, and the energy of the particles reaching the substrate and lower quality films would have been formed [23]. In such a case, a higher cathode voltage would be needed to sustain the plasma [55].

The samples were studied by means of X-ray photoelectron spectroscopy, but the cation stoichiometry found could not be taken into account owing to the low signal of the Ga peak. A weight content of 2% of Ga_2O_3 in ZnO target meant a Ga content ratio ([Ga]/([Zn]+[Ga])%) of 1.7%. In case of the target used in the last chapter (2 wt.% of Al_2O_3), the Al content ration ([Al]/([Zn]+[Al])%) in the target was 3.2 %. This difference is due to the lower atomic mass of aluminium, that leads to a higher cation content for targets with the same doping weight content.

X-ray diffraction analysis of the samples showed similar features like ZnO:Al samples as discussed in Chapter 4, and hence the whole spectra are not shown here. As typical for magnetron sputtered ZnO layers [136, 137], the existence of a polycrystalline layer with grains showing a hexagonal wurtzite structure was observed. The grains were predominantly oriented with their c-axis perpendicular to the substrate surface as it was found for ZnO:Al layers. The XRD spectra exhibited a ZnO (002) peak at around 34.4^o as well as its second order diffraction (004) at around 72.4^o. No phases related to Ga_2O_3 could be observed, owing to the relatively small extrinsic doping amount or to the fact that Ga^{3+} was substitutionally replacing Zn^{2+} sites.

The full width at half maximum and the lattice parameter c were deduced from the broadening and the position of the XRD peaks and are shown in Fig. 5.2. The lattice parameter c decreased until it reached 0.27 Pa, and it was kept constant afterwards. As the deposition pressure increased, the lattice parameter c got closer to the standard reported parameter for ZnO (0.5207 nm [38]). It suggested that the lattice suffered a

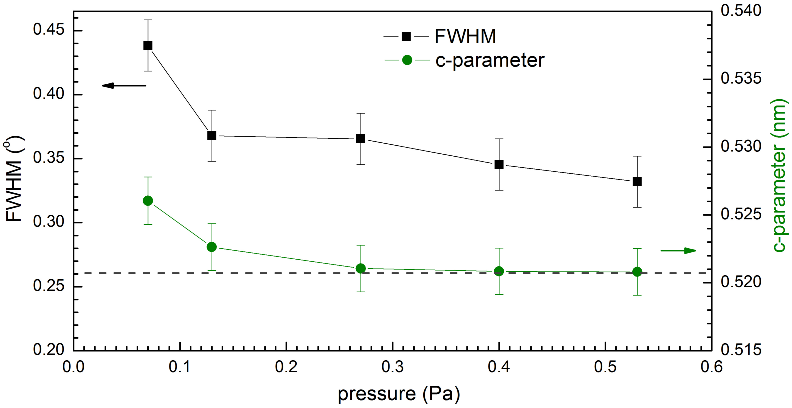

Figure 5.2: The FWHM (square) and the lattice parameter *c* (circle) of ZnO:Ga samples deposited at different pressures. The value of the standard lattice parameter *c* (0.5207 nm [38]) is marked with a grey dashed line. Lines connecting data points are added to guide the eyes.

macroscopic compressive stress when low pressures were used, but higher pressures led to the relaxation of the lattice.

The lattice parameter *c* of the ZnO:Ga 2 wt.% sample deposited at 0.4 Pa can be compared to the ZnO:Al 2 wt.% sample deposited without intentional heating described in Sec. 4.1.1. Both were deposited under the same pressure, substrate temperature, discharge power, target to substrate distance and both presented quite similar thicknesses. The only difference is the dopant used. The lattice parameter *c* of the ZnO:Ga layer was 0.5208 nm while the one of ZnO:Al was 0.5215 nm. ZnO:Ga showed a value closer to the standard value for undoped ZnO (0.5207 nm [38]) since the atomic radius of Ga is closer to that of Zn. However, the difference is rather small.

The FWHM decreased rapidly at low pressures, specially from 0.07 to 0.13 Pa. Afterwards, it kept on decreasing but at a lower rate. The reduction of the FWHM pointed out the existence of a better crystalline quality with the increase in pressure.

From the deconvolution of the fitted XRD peak profile, the gaussian and lorentzian part of the broadening were obtained. Thereby, the grain size *D* and the microstrain *e* were obtained and are shown in Fig. 5.3. The grain size showed a significant improvement with the increase in pressure

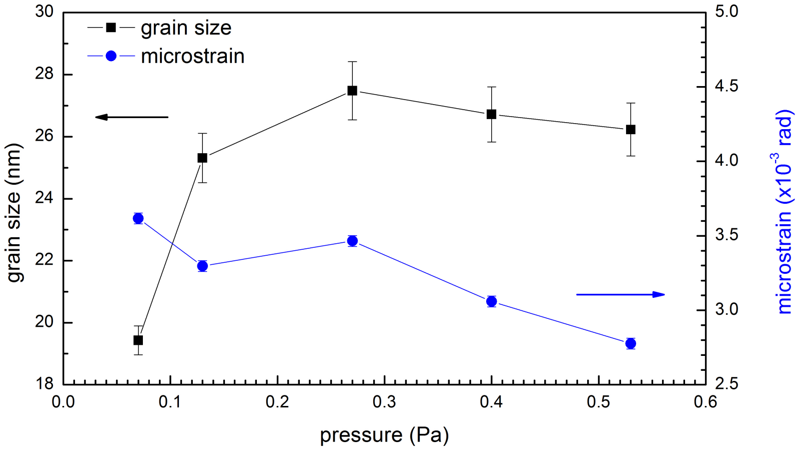

Figure 5.3: The variation of the grain size D (square) and microstrain e (circle) of ZnO:Ga thin films deposited at different pressures. Lines connecting data points are added to guide the eye.

from 0.07 to 0.27 Pa and then D remained almost constant or even slightly decreased. At 0.27 Pa, the grain size achieved its highest value (27.5 nm) and afterwards showed a slightly decreasing tendency at higher pressures probably caused by the energy loss of the incoming particles owing to the collisions suffered on its way from the target to the substrate. In the case of microstrain, the variation was not much significant, but a slight decreasing tendency was found. The contribution of both parameters explained the tendency observed in FWHM.

The optical properties were studied from the measurements obtained by spectrophotometry and are shown in Fig. 5.4. As usual for a transparent conducting oxide, three different features were observed in the optical transmittance spectra (see Sec. 2.3). First, a band to band absorption in the ultraviolet part of the spectra which enhanced an abrupt drop in transmittance. Second, a highly transparent region in the visible range, with transmittances above 83.7%. In the range between 800 and 1100 nm, the average transmittance was above 86.3% in all cases. Third, a slight decrease in the near infrared part of the spectra was observed, caused by free carriers absorption. A further decrease would have been observed if

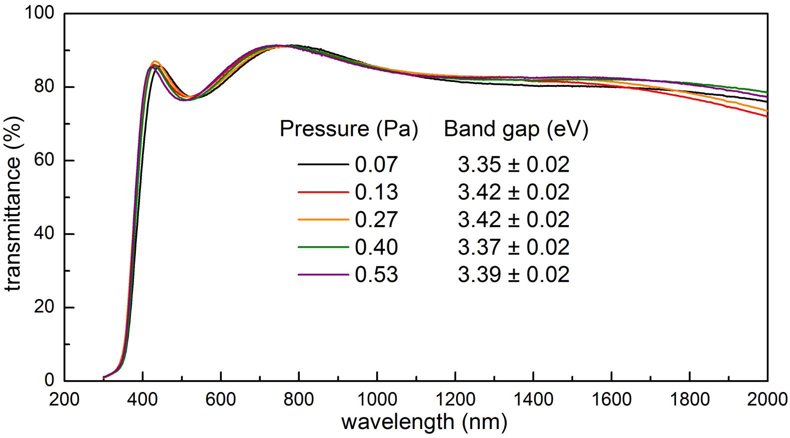

Figure 5.4: The transmittance curves of ZnO:Ga thin films deposited at different pressures.

the measured range were longer.

The average transmittance in the visible range of the ZnO:Al sample deposited at room temperature as discussed in Sec. 4.1.1 was of 85.4% whereas the transmittance for the ZnO:Ga layer deposited at 0.4 Pa was of 84.3%. In the range between 800 and 1100, ZnO:Al showed an integrated transmittance of 85.1% while ZnO:Ga showed an averaged value of 86.7%. The difference is rather small, but ZnO:Ga showed a slightly better transmittance in the NIR.

The absorption coefficient and the band gap energy were determined from the transmittance and reflectance spectra by means of Eq. 2.4 and 2.5. The calculated values of band gap energies of the ZnO:Ga films deposited at various pressures did not show a clear tendency with pressure (see the values in Fig. 5.4). The lowest value was of 3.34 eV at 0.07 Pa, and the highest was 3.42 eV at 0.13 and 0.27 Pa.

The electrical properties were studied by means of 4-point probe and Hall effect measurements. The resistivity, mobility and carrier concentration can be observed in Fig. 5.5. The resistivity showed an almost constant behaviour until it reached 0.27 Pa and afterwards increased reaching 9.0×10^{-3} $\Omega\,$cm at 0.53 Pa. By Hall effect measurements, the mobility

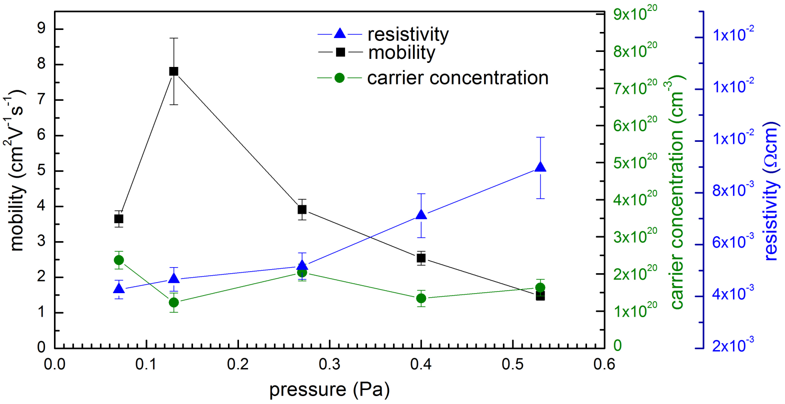

Figure 5.5: The variation of resistivity (triangle), carrier concentration (circle) and Hall mobility (square) of the ZnO:Ga thin films deposited at different pressures. All the lines are added to guide the eye.

and carrier concentration were measured. Mobility was improved for the sample deposited at 0.13 Pa reaching 7.8 cm^{2}V^{-1}s^{-1}. Then, it slowly decreased for higher pressures. Meanwhile, carrier concentration showed an almost constant behaviour with values between 1×10^{20} to 2×10^{20} cm^{-3} as expected from the band gap energies found. If changes in the carrier concentration were found, the band gap would move toward higher (higher carrier concentration) or lower energies (lower carrier concentration) due to the Burstein-Moss effect (Sec. 2.3.1). Moreover, changes in carrier concentration would also change the position of the plasma frequency and, thus, the NIR part of the transmittance spectra would also have been affected.

The mobility measured for the ZnO:Al layer deposited under the same conditions in the previous chapter was of 22 cm^{2}V^{-1}s^{-1}, whereas the carrier concentration was of 6.2×10^{19} cm^{-3}. The ZnO:Ga layer deposited at 0.4 Pa showed a mobility 2.5 cm^{2}V^{-1}s^{-1} and a carrier concentration 1.2×10^{20} cm^{-3}. It is remarkable that ZnO:Ga layers show higher carrier concentrations but much lower mobilities.

The limiting electrical transport mechanism for the samples studied here was the grain boundary scattering given that the carrier concentration was below 3×10^{20} cm^{-3} [55]. The mobility improvement at 0.27 Pa had to be ascribed to an increase in lateral grain size or to a decrease in trap density at the grain boundaries, due to the almost constant behaviour of the carrier concentration. In the low pressure range, an increase in vertical grain size is found, but then, grain size remained almost constant. However, the limiting factor in Hall mobility is the lateral grain size, not the vertical. In some cases, both parameters are related, but it is not necessary. Here, it is difficult to relate the mobility improvement only to the grain size since for pressures higher than 0.13 Pa, the mobility decreased, but grain size still increased. Therefore, the increase in mobility at 0.27 Pa must have been enhanced by a lower trap density at the grain boundaries. For pressures higher than 0.13, the lower energy of the impinging particles might have led to an increase in defect density between the grains and it might have reduced the mobility.

This observation is in agreement with the structure zone model developed by Thornton [67] and adapted to ZnO by Kluth *et. al.* [68], where an increase in deposition pressure implied the transition from a zone with densely packed fibrous grains to a zone with a porous structure consisting of tapered crystallites separated by voids. This voids would limit the inter grain transport and would explain the decreasing mobility for pressures higher than 0.13.

However, when comparing the ZnO:Ga layer deposited at 0.4 Pa to the ZnO:Al layer deposited at the same pressure in the temperature series (Sec. 4.1.1), the higher mobility found for a much lower carrier concentrations suggests that ionised impurity scattering limits the electrical mobility in ZnO:Ga layers. Although the changes from sample to sample in the ZnO:Ga pressure series discussed in this section were related to a change in the grain barrier height (constant carrier concentration), the comparison between the two doping materials suggested that ionised impurity scattering could have limited the presence of higher mobilities in ZnO:Ga.

Despite the higher Al cation content ratio in 2 wt.% ZnO:Al target (3.2%) in comparison to Ga cation content ratio in 2 wt.% ZnO:Al (1.7%), the carrier concentration was considerably higher for the ZnO:Ga layer. Probably, the better suitability of Ga^{3+} into Zn^{2+} lattice sites must have enhanced the charge carrier density.

Conclusions

In this section, a set of ZnO:Ga layers deposited at pressures between 0.07 and 0.53 Pa were characterised. The different pressures used modified the plasma dynamics and the growth of the resulting layers. Polycrystalline layers with the *c*-axis oriented perpendicular to the substrate were obtained. The FWHM decreased with pressure. The pressure range used influenced the grain size, which reached 27 nm at 0.27 Pa. The mobility of the layers was modified achieving the highest value of 7.8 $cm^2V^{-1}s^{-1}$ at 0.13 Pa, but the carrier concentration stayed almost constant with varying pressure.

The ZnO:Ga layer deposited at 0.4 Pa was compared to a ZnO:Al layer deposited at the same pressure. The lattice parameter c was found to be smaller in case of ZnO:Ga regardless of the higher concentration of charge carriers measured in ZnO:Ga (above 10^{20} cm^{-3}) in comparison to ZnO:Al (6.2×10^{19} cm^{-3}). The ZnO:Al layers presented a higher mobility and a lower carrier concentration compared to ZnO:Ga.

5.2 Influence of doping concentration

The electrical transport in ZnO is normally enhanced by doping the material with specimens that provide an extra electron for conduction. Nevertheless, a higher carrier concentration could also imply a worsening of the optical properties in the long wavelength range. Different concentrations of extrinsic dopants are normally used in order to find the optimal amount of free carriers. Here, three distinct targets were used to study the dependence of Ga_2O_3 dopant onto the resulting ZnO:Ga layers. The dopant weight contents of the targets used were 2, 4 or 6%. All the depositions were performed without intentional substrate heating to use them later in the back reflector for amorphous or microcrystalline *pin*-type solar cells. The deposition pressure chosen was 0.13 Pa, which had resulted into the layer with the highest mobility in the previous section. An Ar flow of 6 sccm was used. The time was adjusted to obtain 200 ± 20 nm layers. The morphological, optical, and electrical properties are detailed below.

The X-ray diffraction pattern of ZnO:Ga films grown by rf magnetron sputtering using different Ga_2O_3 wt.% contents were recorded. All the samples showed a broad diffraction peak at around $2\theta = 34.4\ ^\circ$ and an

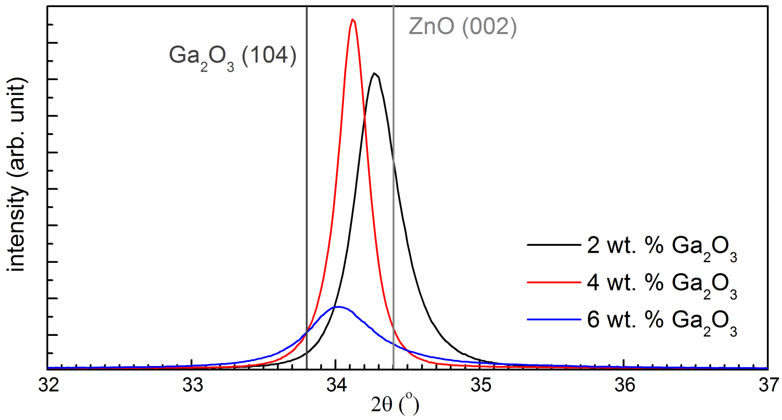

Figure 5.6: XRD spectra of the layers deposited with different Ga_2O_3 doping level. The standard ZnO (002) peak position, as well as Ga_2O_3 (104), are marked in the graph.

additional second peak of lower intensity at 72.4 °. The first peak corresponded to the ZnO (002) plane and the second one to the second order diffraction (004). It implied the existence of a hexagonal wurtzite polycrystalline structure with a strong preferred orientation along the [001] direction, i.e. grains with the *c*-axis perpendicular to the substrate surface. The ZnO (002) peak obtained for each layer can be observed in Fig. 5.6. The higher the doping concentration, the higher the shift of the diffracted peak to lower angles. Moreover, the peak of the layer deposited from the target with a 6 wt.% of Ga_2O_3 broadened significantly. It is remarkable that the (104) peak of Ga_2O_3 is located at 33.7° [157] and the shift and broadening of the 6 wt.% sample spanned both the (104) of Ga_2O_3 and the (002) of ZnO located at 34.4 ° [38]. It suggested that not only ZnO grains were formed, but also rhombohedral Ga_2O_3 grains with a (104) orientation could be present.

From the broadening and the position of the (002) peak, the full width at half maximum and the lattice parameter c were obtained and are shown in Fig. 5.7. The lattice parameter c increased with the increase in doping concentration. It was always higher than the standard reported value (0.5207 nm [38]) suggesting the existence of an increase in macroscopic

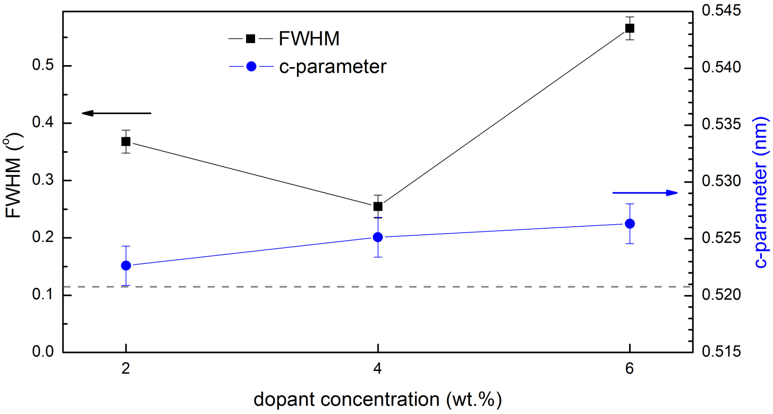

Figure 5.7: The FWHM (square) and the lattice parameter c (circle) of the ZnO:Ga samples deposited using different Ga_2O_3 doping concentration. The value of the standard lattice parameter c (0.5207 nm [38]) is marked with a grey dashed line. Lines connecting data points are added to guide the eyes.

compressive lattice stress with the increase in doping concentration. This stress may have been enhanced by the introduction of more Ga^{3+} in Zn^{2+} lattice sites. However, in case of 6 wt.% the existence of the Ga_2O_3 (104) peak next to the ZnO (002) may be the responsible factor for the observed shift in peak position and, thus, in the lattice parameter c. Probably, two different structures might have segregated in case of the 6 wt% doping. The FWHM showed a minimum for a doping concentration of 4 wt.% Ga_2O_3 pointing out that the best crystalline quality was obtained for such a concentration.

Fitting a pseudo-Voigt function to the diffraction peaks, the grain size D and the microstrain e of the layers were obtained (see Sec. 3.4.2.1). The grain size in the direction perpendicular to the substrate surface showed a maximum value of 34 nm at a doping concentration of 4 wt.%, whereas the microstrain slightly decreased with the increase in doping concentration. The bigger grain size obtained for a doping concentration of 4 wt.% explained the better FWHM (crystal quality) obtained before. The decrease in microstrain suggested that a better crystal quality within the grains was obtained with higher doping, i.e, fewer defects within each grain (see Sec.

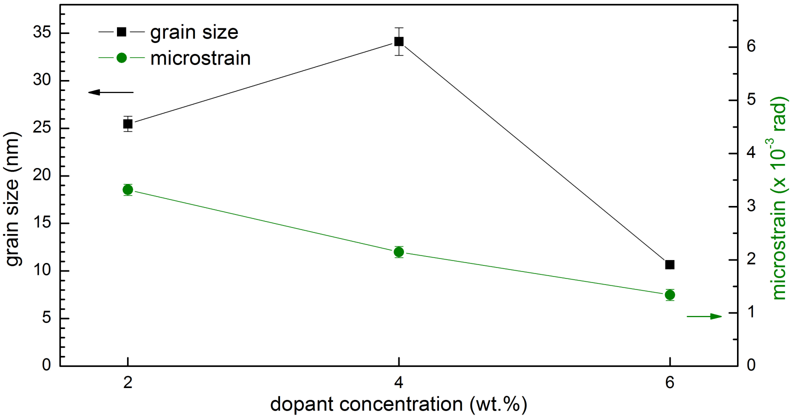

Figure 5.8: The variation of the grain size D (square) and microstrain e (circle) of the ZnO:Ga thin films deposited using targets containing different Ga_2O_3 doping concentration. Lines connecting data points are added to guide the eye.

3.4.2.1).

By means of X-ray photoelectron spectroscopy, the content ratio of Zn and Ga was measured. The manufacturer indicated that the ZnO:Ga targets contained 2, 4 and 6 wt.% of Ga_2O_3. When converting this weight percent into content ratio ([Ga]/([Zn]+[Ga])%) it would imply 1.7, 3.5 and 5.3% respectively. When analysing the obtained films by XPS, the layers deposited from 2 wt.%, 4 wt.% and 6 wt.% of Ga_2O_3 targets, showed Ga content ratios ([Ga]/([Zn]+[Ga])%) of 3.5 ± 1%, 5.4 ± 1% and a 11.0 ± 1% respectively. The measurements were performed after 1 minute of Ar sputtering of the surface prior to the XPS measurement. The error for such a small concentration was high owing to the low signal of the obtained peaks. Nevertheless, the incorporation of Ga was much higher than what was expected from the target content.

The transmittance of the samples was recorded with a spectrophotometer, and the results are shown in Fig. 5.9. The layers were highly transparent in the visible range showing an integrated transmittance above 84.6% between 400 and 800 nm. Between 800 and 1100 nm, the transmittance for the 2 wt.% Ga_2O_3 was of 86.2 %, whereas for the 4 and 6 wt.% Ga_2O_3 was of 84.4 and 84.1% respectively. Although the difference was not large,

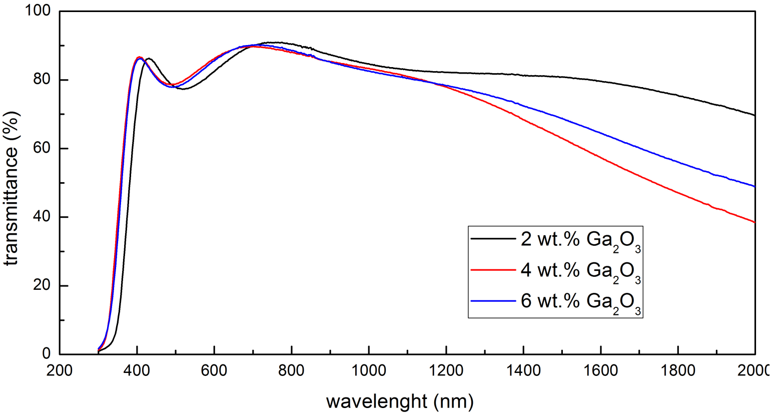

Figure 5.9: The transmittance curves of ZnO:Ga thin films deposited using targets containing different Ga_2O_3 doping concentration.

the reduction in the NIR part could be detrimental for microcrystalline solar cells. For longer wavelengths, an important drop in transmittance was observed caused by the free carrier absorption. The 4 wt.% Ga_2O_3 doped layer showed the highest drop in transmittance in this range pointing out that it had the highest amount of charge carriers. A decrease in transmittance was also observed in the ultraviolet part of the spectra as expected for a wide band gap TCO material, due to the band to band absorption. Comparing the cutting edge of the three layers, a displacement towards shorter wavelengths can be observed for the layer deposited with a 4 and 6 wt.% Ga_2O_3.

The absorption coefficient and the band gap energy were determined from the transmittance and reflectance spectra by means of Eq. 2.4 and 2.5. The estimated band gap energy values of the ZnO:Ga films deposited with different Ga_2O_3 doping concentration are shown in Fig. 5.10. A huge increase in the band gap energy was observed for a doping concentration of 4 wt.% (3.71 eV) compared to 2 wt.% doping (3.45 eV). The band gap energy of the layer with a doping concentration of 6 wt.% decreased again (3.67 eV) but still showed a high band gap value.

The samples were electrically characterised by means of Hall effect measurements. The resistivity, carrier concentration and mobility of the as-

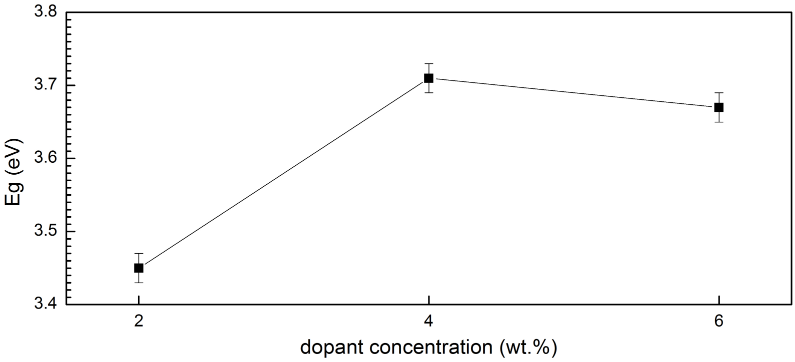

Figure 5.10: Band gap energies against Ga_2O_3 doping concentration.

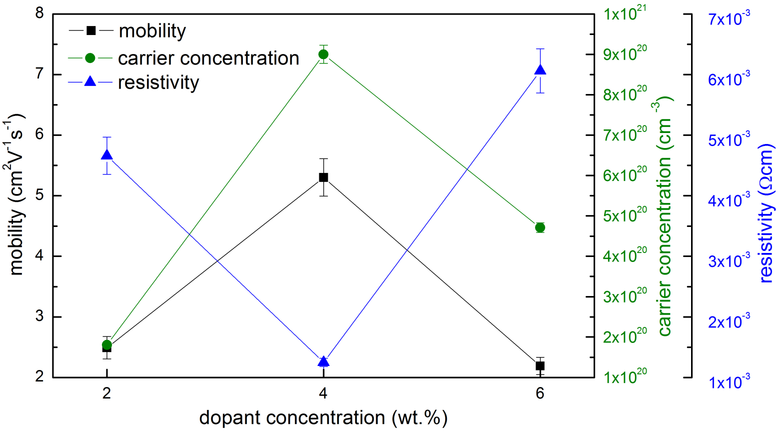

Figure 5.11: The variation of resistivity (triangle) carrier concentration (circle) and mobility (square) of the ZnO:Ga thin films deposited using targets containing different Ga_2O_3 doping concentration. All the lines are added to guide the eye.

deposited samples are shown in Fig. 5.11. At a doping concentration of 4 wt.%, the lowest resistivity (1.25×10^{-3} Ω cm) as well as the highest mobility (5.3 cm^{2}V^{-1}s^{-1}) and carrier concentration (9×10^{20} cm^{-3}) were achieved. Further increase or decrease in the doping concentration led to an impoverishment of the electrical properties.

Increasing the doping concentration from 2 to 4 wt.% must have led to a higher incorporation of extrinsic dopants into lattice sites, where more Ga^{3+} could replace Zn^{2+} lattice sites. With a carrier concentration as high as 9×10^{20} cm^{-3}, the mobility increased instead of decreasing as expected if ionised impurity scattering were the limiting transport mechanism as expected for such a high carrier concentration [55]. Instead, grain boundaries might have played a role in electrical conduction mechanism and, thus, increasing the amount of carriers reduced the barrier height at grain boundaries. Moreover, a bigger vertical grain size was found by XRD for a 4 wt.% doping, which could also be related to bigger lateral sizes and could have helped to enhance the mobility. The carrier concentration found was near to the upper limit of ZnO of about 1.5×10^{21} cm^{-3} [80].

The fact that a higher doping concentration in the target (6 wt.%) did not lead to a higher amount of carrier concentration, it suggested that no more Ga^{3+} could further replace Zn^{2+} lattice sites. Instead, Ga_2O_3 might have formed grains in between ZnO:Ga doped grains, as suggested from XRD, reducing the amount of carriers which account for conduction in ZnO:Ga and decreased the mobility owing to a higher barrier height at grain boundaries. The maximum solubility of Ga in ZnO (2.7 at.% by Wang *et al.* [158]) must have been reached. Other reports [51, 159] show that at high Ga concentrations, $ZnGa_2O_4$ phases can appear. These phases could be present in heavily Ga-doped ZnO thin films as small nanocrystals yielding broad and weak X-ray scattering, which made them difficult to detect. Although they were not measured here, the presence of ternary compounds could not be discarded.

The variation in carrier concentration justified the band gap widening or narrowing, which was attributed to the Burstein-Moss effect [74, 75]. In case of degenerately doped materials, as the amount of free carriers increases, the Fermi level moves towards higher values because the energy required to activate an electron from the valence band to the conduction band is higher than the fundamental band gap.

The absorption in the NIR part of the spectra was also associated to the different carrier concentration measured at different target doping. The carrier density determines the position of the plasma frequency (Eq. 2.12). The higher the concentration, the lower the wavelength of the absorption peak and, thus, the measured transmittance is reduced.

Conclusions

After studying the resulting layers deposited with different target doping, the 4 wt.% Ga_2O_3 doping concentration was found to be optimal for the production of highly conducting ZnO:Ga layers with a high band gap energy (3.71 eV). All the layers appeared to be polycrystalline with the *c*-axis perpendicular to the substrate. The higher the doping concentration, the higher the lattice compressive stress. A carrier concentration as high as 9×10^{20} cm^{-3}, with a mobility of 5.3 $cm^2V^{-1}s^{-1}$ was obtained for the layer with a 4 wt.% Ga_2O_3 doping concentration. The use of 6 wt.% Ga_2O_3 target must have led to the formation of Ga_2O_3 grains instead of substitutionally replaced Zn^{2+} by Ga^{3+} in ZnO lattice sites and, thus, the resistivity of the layers increased. The use of highly doped layers (4 and 6 wt.% Ga_2O_3) implied a slight reduction of the transmittance at wavelengths larger than 800 nm in comparison to 2 wt.% Ga_2O_3 due to the change in carrier concentration.

5.3 Influence of substrate temperature

The use of intentional heating during deposition enhances the adatom mobility during the film growth, and it increases the compactness of the layers [68]. To study this effect, the substrate temperature was varied between 21°C and 300°C. This range was chosen to optimise the layers which could be later used during the fabrication process of a solar cell. Low temperatures, such as those between 21 and 150°C could be deposited on the *n* layer of *pin* type silicon thin film devices as part of the back reflector without modifying the previously deposited active layers. Films deposited at higher substrate temperatures are expected to show better performance to be used as the front TCO for silicon thin films solar cells. ZnO:Al layers deposited at substrate temperatures around 300°C were optimised by Berginski *et al.* [35] to be etched and used as front contacts in *pin* thin film silicon solar cells. Higher temperatures are not recommended since they would imply a higher industrial cost.

The target used to study the dependence of temperature on the resulting ZnO:Ga layers had a 4 wt.% of Ga_2O_3, which had been previously considered the one leading to the lowest resistivity. All the depositions were performed at a pressure of 0.13 Pa with an Ar flow of 6 sccm. The deposi-

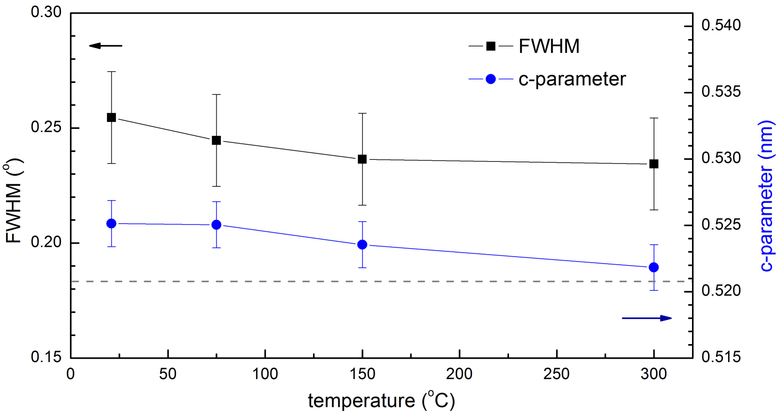

Figure 5.12: The FWHM (square) and the lattice parameter c (circle) of the ZnO:Ga samples deposited at different temperatures. The value of the standard lattice parameter c (0.5207 nm [38]) is marked with a grey dashed line. Lines connecting data points are added to guide the eyes.

tion time was adjusted to obtain 200 ± 20 nm layers. The morphological, optical, and electrical properties are detailed below.

The structure of the layers was characterised by means of X-ray diffraction. Two broad peaks appeared in the spectra, the ZnO (002) peak at around 34.4° and its reflection, the (004) peak at around 72.4°. These peaks indicated the existence of a polycrystalline ZnO layer preferentially oriented with the c-axis perpendicular to the substrate surface. As it was obtained in previous sections, the grains within the layer presented a hexagonal wurtzite structure. Again, no other phases could be detected by XRD.

From the breadth and position of the diffracted peaks, the full width at half maximum and the lattice parameter c were obtained. The peak position (2θ) moved towards longer values indicating a reduction of the lattice parameter c as depicted in Fig. 5.12. The higher the temperature, the closer the c paramenter to the standard ZnO c value, i.e. the lower the lattice compressive stress. The same effect was found for ZnO:Al in Sec. 4.1.1. As shown in Fig. 5.12, the FWHM slightly moved towards lower values with an increase in temperature, indicating an improvement of the crystalline quality of the layers.

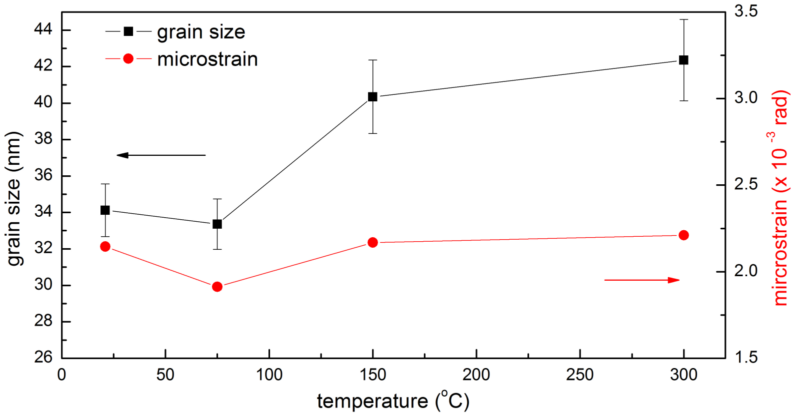

Figure 5.13: The variation of the grain size D (square) and microstrain e (circle) of the ZnO:Ga thin films deposited at different temperatures. Lines connecting data points are added to guide the eye.

From the deconvolution of the pseudo-Voigt diffraction peaks into the gaussian and lorentzian part, the microstrain e, and the estimated grain size D, were calculated (Fig. 5.13). The grain size increased considerably from 150°C onwards, reaching 42 nm at 300°C thanks to the increase in surface diffusion of the arriving species at higher substrate temperatures. The constant behaviour found for the microstrain indicated that the thermal stress did not contribute significantly to modify the amount of local lattice distortions except for the layer deposited at 75°C, which showed a lower e.

By means of X-ray photoelectron spectroscopy the surface and the bulk of the ZnO:Ga layers deposited at different temperatures were analysed. The area under the the O 1s, Zn 2p$_{3/2}$ and Ga 2p$_{3/2}$ peaks were used to estimate the stoichiometry of the samples. The shape and position of the metal peaks (Zn and Ga) did not vary with the increase in temperature. Instead, the shape of the O peak varied considerably.

The surface O 1s spectra (Fig. 5.14) could be described in terms of three gaussian peaks located at a binding energy of $\sim$ 530.4, $\sim$ 532 and $\sim$ 532.6 eV.

The O 1s contribution found at $\sim$ 532.6 eV was attributed to surface

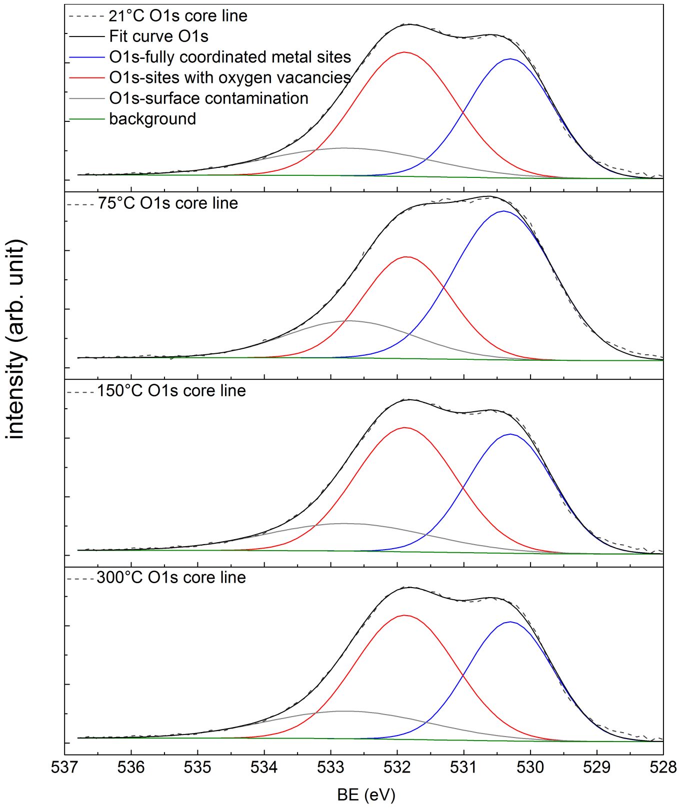

Figure 5.14: The plot of the O 1*s* peak measured by XPS at the surface of the ZnO:Ga layers deposited at different temperatures. The peaks were fitted by means of three gaussian curves at $\sim$ 530.4, $\sim$ 532 and $\sim$ 532.6 eV.

contamination, i.e to oxygen loosely bonded to surface species such as -CO_3, adsorbed H_2O or adsorbed O_2 [32, 160]. No relation could be found between the intensity or area of the surface contamination peak and the substrate temperature. However, this peak masked the relation between the $\sim$ 530.4 and $\sim$ 532 peak. To remove this contribution, the samples were etched by Ar during 1 minute. Afterwards, the metal and oxygen peaks were characterised again. Then, the O 1*s* peak did not present the contribution of surface contamination but still two peaks could be observed as shown in Fig. 5.15. The suppression of the contamination peak by means of etching the surface was also found in [161]. The fitted peaks were associated to fully coordinated O sites ($\sim$ 530.4 eV) and to sites with oxygen vacancies ($\sim$ 532 eV). The peaks positions found in this work were in accordance with previous publications on ZnO:Al [61, 161, 162].

The O 1s component at 530.4 eV is attributed to O^{2-} ions in a wurtzite structure surrounded by Zn (or the substitution of Ga) atoms in a fully oxidised stoichiometric surrounding [161]. Instead, the peak centered at 532 eV, is associated to oxygen vacancies, i.e. O^{2-} ions surrounded by metal ions but in an oxygen deficient region where neighbouring O^{2-} ions are missing. Therefore, changes in this component are connected to the variation in the concentration of oxygen vacancies.

At the layer surface (Fig. 5.14), the intensity of the oxygen vacancies component was similar or even higher than the fully coordinated O 1s contribution. It indicated the existence of a large oxygen-deficient state at the layer surface. On the contrary, as shown in Fig. 5.15A, bulk measurements showed a considerably lower intensity of the O 1s peak related to oxygen deficiency sites in comparison to the fully coordinated O 1s peak at 530.4 eV. Independently of the temperature used, the peak presented the same feature indicating that the amount of oxygen vacancies in bulk did not vary throughout the substrate temperature range used here.

The Ga content ratio ([Ga]/([Zn]+[Ga]) was characterised from the metal $2p_{3/2}$ peaks obtained by XPS after etching the samples surface and results are shown in Fig. 5.15B. It was found that the Ga content ratio increased considerably reaching a maximum of 9.2% at a substrate temperature of 75°C and then it decreased smoothly. The huge amount of Ga incorporated at 75°C was unexpected, but it explained the slightly anomalous behaviour found in terms of grain size and microstrain for the aforementioned layer. The concentration of Ga was found to be high above the content ratio of the target, which was 3.5% [Ga]/([Zn]+[Ga]) for a 4 wt.% Ga_2O_3.

The optical properties of the layers were characterised by means of a spectrophotometer and the transmittance can be observed in Fig. 5.16. All the layers presented an integrated transmittance above 85.5% in the visible range (400 to 800 nm) and above 83.8% in the range between 800 and 1100. Given that the layers were deposited with a 4 wt.% Ga_2O_3, the absorption in the near infrared part of the spectra was considerably

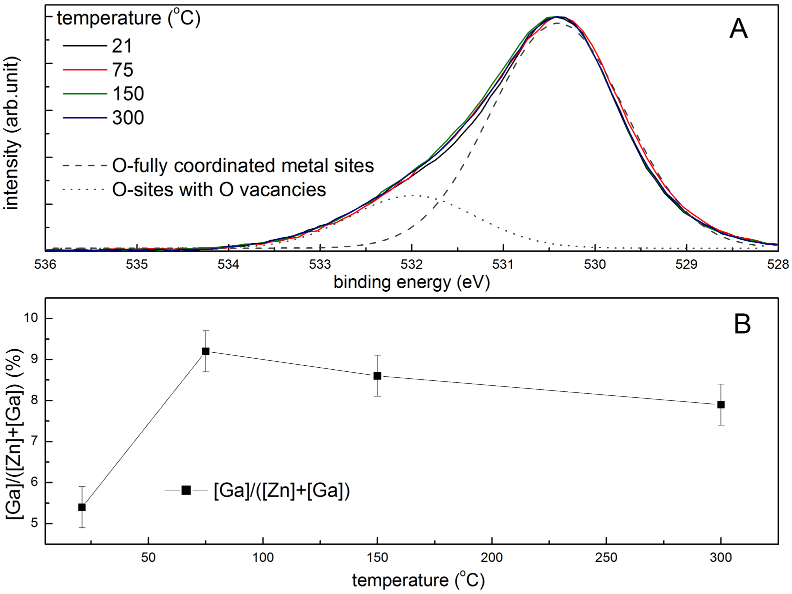

Figure 5.15: In the top graph (A), the plot of the normalised O 1*s* peak measured by XPS after etching the surface of the ZnO:Ga layers deposited at different temperatures. The peaks were fitted by means of two gaussian curves at $\sim$ 530.4 and $\sim$ 532 eV. In the bottom graph (B), the Ga content ratio, [Ga]/([Zn]+[Ga]) against the temperature. Lines are added to guide the eyes.

high. In general trends, except for slight differences in the interferences schemes due to slightly different thicknesses, the spectra showed a similar behaviour even in the long wavelength range pointing out a similar amount of free carriers.

From the transmittance and reflectance of the deposited layers, the absorption coefficient was calculated, and the band gap energy was obtained by means of the Tauc plot: $((h\nu)^2$ against $(h\nu))$. The calculated band gap energies of the films deposited at different substrate temperature are shown in Fig. 5.17. Quite similar values were obtained. The highest value was 3.77 eV at a substrate temperature of 150°C, and the lowest was only 3.69 eV at 300°C.

The electrical properties (resistivity, mobility and carrier concentration)

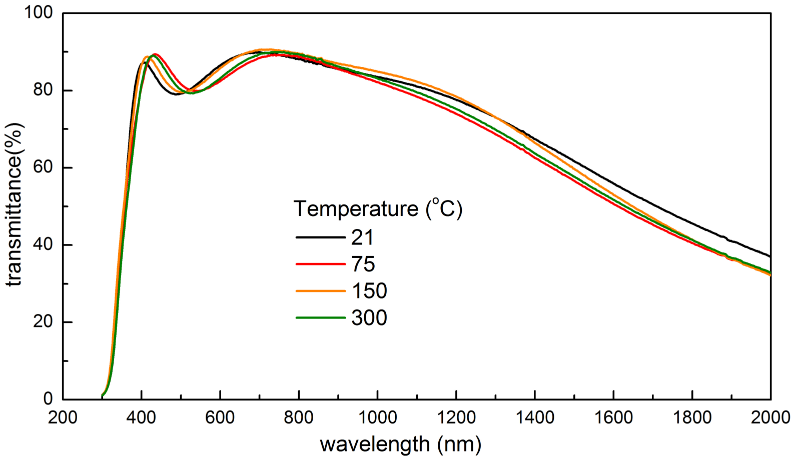

Figure 5.16: The transmittance curves of ZnO:Ga thin films deposited at different temperatures.

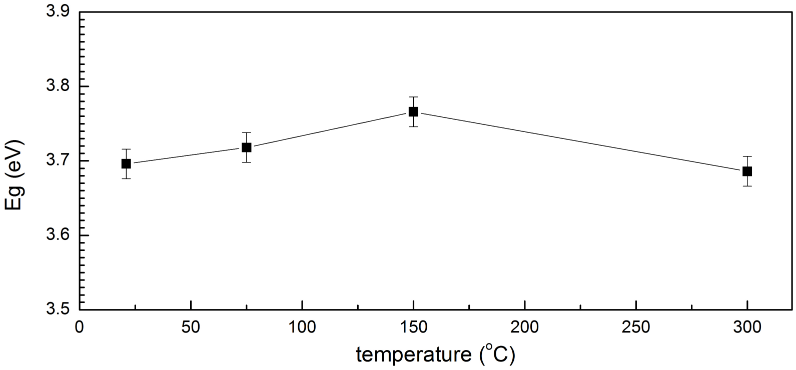

Figure 5.17: Band gap energies against deposition temperature.

of the layers are shown in Fig. 5.18. The lowest resistivity (6.4×10^{-3} Ω cm) was achieved at 300°C. Mobility raised monotonously with the increase in temperature reaching a value of 10.7 cm^{2}V^{-1}s^{-1} at 300°C. The carrier concentration, instead, reached its highest value at room temperature (9×10^{20} cm $^{-3}$) and decreased to its lowest value at 75°C to raise again till 300°C.

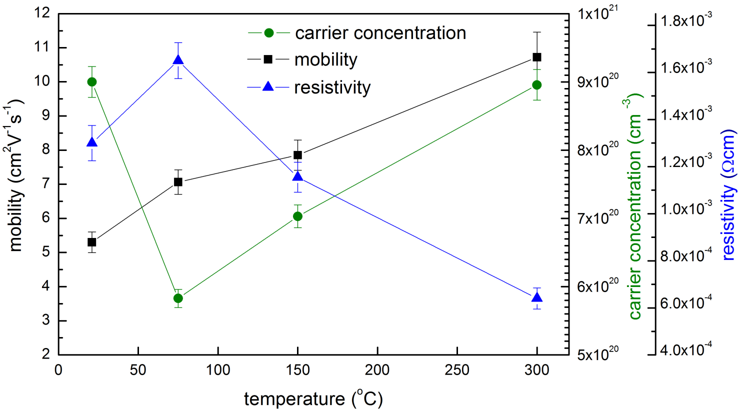

Figure 5.18: The variation of resistivity (triangle) carrier concentration (circle) and mobility (square) of the ZnO:Ga thin films deposited at different temperatures. All the lines are added to guide the eye.

Although the variation was not large, a remarkable reduction of the carrier concentration took place at 75°C. This reduction coincided with a lowering of the grain size as well as with the highest amount of Ga incorporated into the layer. The low carrier concentration found at 75°C suggested that part of the incorporated Ga was not substitutionally replacing Zn^{2+} sites but it must have segregated forming Ga_2O_3 or other ternary compounds such as $ZnGa_2O_4$ [51]. Increasing the temperature above 75°C must have enhanced the substitution of Zn^{2+} by Ga^{3+}. The sample deposited at 75°C was repeated, and the same results were obtained pointing out that some effect at such a temperature took place. At 75°C, the temperature may have been the responsible for a higher incorporation of Ga but this temperature could not be high enough to enhance the substitution of Zn^{2+} by Ga^{3+}. Nevertheless, the differences in carrier concentration were not high, and their variation effects could not be detected in the near infrared absorption nor in the band gap.

In spite of the high carrier concentration found, the grain boundary scattering is thought to play the crucial role in limiting the electrical transport. This mechanism depends mainly on the lateral grain size, the trap density at the grain boundaries and the carrier concentration. Considering the aforementioned results, the increase in mobility could be ascribed to bigger grain sizes except for the sample deposited at 75°C. Moreover, lower trap densities would be also expected in the grain boundaries with the increase in temperature as discussed in Sec. 4.1.1.

Conclusions

As a summary, a set of ZnO:Ga layers deposited at substrate temperatures between 21 and 300°C were studied. The increase in adatom mobility onto the growing layer improved the crystalline quality and reduced the lattice compressive stress. Optical transmittances were found to be above 85.5% in the visible wavelength range and above 83.8% in the range between 800 and 1100. By means of XPS, the existence of a large oxygen-deficient state at the layers surface was proved. Moreover, the amount of oxygen vacancies in bulk did not vary throughout the substrate temperature range used here. The highest Ga incorporation (9.2%), as well as the lowest carrier concentration, was found at 75°C, which was thought to imply the formation of Ga_2O_3 or other ternary compound at the ZnO grain boundaries. The highest mobility (10.7 $cm^2V^{-1}s^{-1}$) and the lowest resistivity ($6.4\times10^{-3}\ \Omega\,cm$) were achieved at 300°C.

5.4 Influence of oxygen volume concentration

The use of oxygen during deposition is reported to reduce the amount of free carriers which, on one hand, enhances the transparency of the layer at long wavelengths, but on the other hand, reduces the electrical conductivity [163]. A small amount of oxygen was added during deposition, to find a compromise between both effects. Different oxygen flows were mixed with argon during sputter deposition to study the influence of oxygen on the layer properties. The concentration of oxygen in volume was varied between 0% and 4.6%. It implied using a constant argon flow of 20 sccm and adding an oxygen flow between 0.46 and 0.97 sccm. In comparison to previous sections, higher Ar fluxes were necessary to get a low oxygen volume concentration. The reason was that the mass flow controllers of the equipment could not fix lower oxygen concentrations. Therefore, the layers are not comparable to those of the previous sections. Although the pressure was the same, different fluxes resulted in different residence time

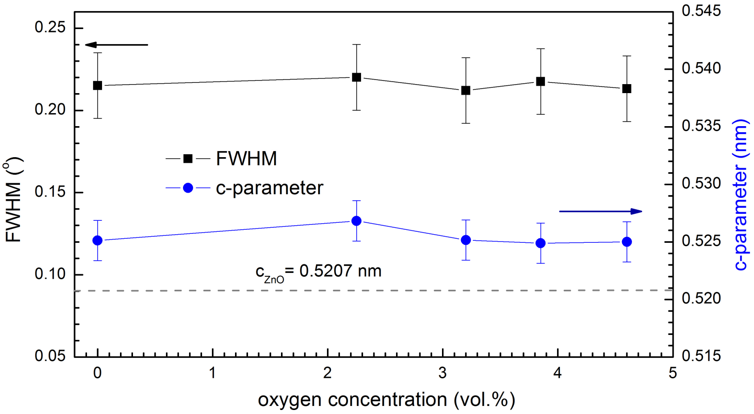

Figure 5.19: The FWHM (square) and the lattice parameter c (circle) of the ZnO:Ga samples deposited with diferent O_2 volume concentrations. The value of the standard lattice parameter c (0.5207 nm [38]) is marked with a dashed line. Lines connecting data points are added to guide the eyes.

of Ar atoms and, thus, different ionisation efficiencies that led to slightly different layers. The target used to study the dependence of oxygen concentration onto the resulting ZnO:Ga layers had a 4 wt.% of Ga_2O_3. All the depositions were performed without intentional substrate heating at a pressure of 0.13 Pa. The time was adjusted to obtain 200 ± 20 nm layers. The morphological, optical, and electrical properties are detailed below

The X-ray diffraction spectra showed, as normally obtained for magnetron sputtered ZnO layers [136, 137], a polycrystalline hexagonal wurtzite structure with the c-axis predominantly oriented perpendicular to the substrate surface. The XRD spectra exhibited a ZnO (002) peak at around 34.4° as well as its second order diffraction (004) at around 72.4°. No clear phases related to Ga_2O_3 or any other compound could be observed.

The main properties of the layer structure were studied by XRD. The full width at half maximum and the lattice parameter c were deduced from the broadening and the position of the diffracted peak and are given in Fig. 5.19. The FWHM remained almost constant pointing out to the existence of a constant crystalline quality with the increase in oxygen flow.

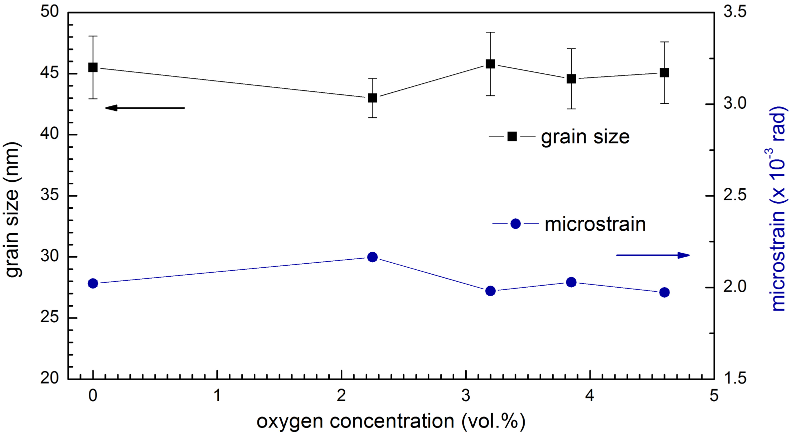

Figure 5.20: The variation of the grain size D (square) and microstrain e (circle) of the ZnO:Ga thin films deposited with different O_2 volume concentrations. Lines connecting data points are added to guide the eye.

It suggested that oxygen had no influence on the polycrystalline structure of the layers. The lattice parameter c also showed a similar behaviour. It stayed almost constant with the increase in the oxygen volume. In any case, the values of the lattice parameter c obtained were higher than the standard parameter for ZnO (0.5207 nm [38]) suggesting that the layers suffered a remarkable compressive lattice stress. This stress might have been related to the high doping amount contained in the layers.

From the fitting of the XRD peak profiles by means of pseudo-Voigt functions, the gaussian and lorentzian part of the broadening were obtained. The grain size D and the microstrain e contained in the grains are shown in Fig. 5.20. The grain size showed no significant deviation from its initial value of $\sim$ 45 nm. It stayed almost constant regardless the higher oxygen concentration. The microstrain slightly increased for a 2.25 vol.%, and it was kept constant for higher oxygen volumes. Therefore, no major changes in defects within a crystal occurred during the sputtering under oxygen gas.

To investigate the changes in the chemical state of the ZnO:Ga thin films, the X-ray photoelectron spectroscopy spectra were analysed. The surface and the bulk of the ZnO:Ga layers deposited with different oxygen volumes were studied.

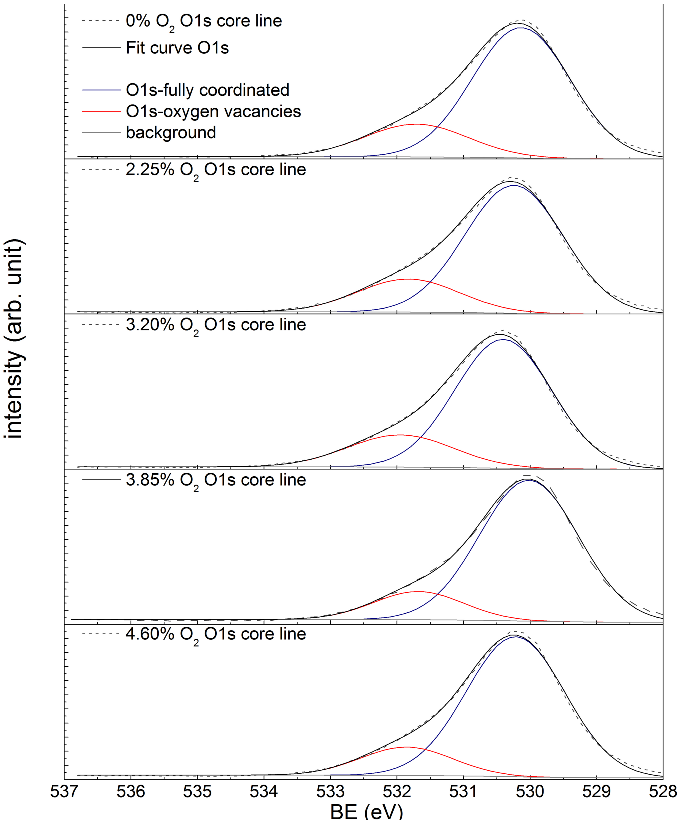

Figure 5.21: The plot of the O 1*s* peak measured by XPS after etching the surface of the ZnO:Ga layers deposited with different oxygen volume concentrations. The peaks were fitted by means of two gaussian curves at ∼ 530.4 and ∼ 532 eV.

Firstly, the metal peaks were analysed to obtain the stoichiometry of the layers. The Ga content ratio ([Ga]/([Zn]+[Ga])) was characterised from the Zn and Ga $2p_{3/2}$ peaks obtained after etching the sample surface using Ar. It was found that Ga content ratio slightly decreased with the incorporation of oxygen inside the chamber. The Ga content varied between 8.8% (0 vol.% O_2) and 8.2% (4.6 vol.% O_2), which were quite high values in comparison to the cation content ratio of Ga in the target (3.5%).

The close inspection of the O 1*s* surface peak showed that it was composed of three gaussian components centered at 530.4, 532 and 532.60 eV, respectively. The high binding energy component located at 532.60 eV is usually attributed to the presence of loosely bound oxygen at the surface of ZnO films, belonging to contaminant species, i.e. -CO_3, adsorbed H_2O or adsorbed O_2 [32, 160]. The contribution of this peak was relevant at the sample surface and varied independently of the oxygen concentration during deposition. In the previous section, it was observed that this component disappeared in bulk, i.e. after sputtering the sample surface by Ar ions. In bulk, the O 1*s* peak did not present the contribution of surface contamination but still two peaks could be shown in Fig. 5.21. The extinction of the contamination peak after etching the surface was also found in [161].

The low binding energy fitted peak corresponded to fully coordinated O sites ($\sim$ 530.4 eV). The high binding energy fitted peak corresponds to sites with oxygen vacancies ($\sim$ 532 eV). The characterisation of this peak gives an idea of the oxygen deficiency sites present in the layers. The peak positions found in this work were in accordance with previous publications on ZnO:Al [61, 161, 162]. In Fig. 5.21, it can be observed that, when the oxygen volume concentration increased, the peak related to oxygen vacancies was reduced. However, the reduction was minimal, and the observation in such a graph was difficult.

To further analyse the variation between the O 1*s* fully coordinated and the oxygen vacancies emission features, the ratio between bulk O 1*s* peaks and metal peaks ([Zn]+[Ga]) is plotted in Fig. 5.22. The top graph shows the ratio between the entire O 1*s* feature and the metal peaks. The middle and the bottom graphs show the oxygen-metal ratio using each O 1*s* contribution, i.e. the $\sim$ 530.4 eV (fully coordinated O 1*s* sites) and the $\sim$ 532 eV (sites associated to oxygen vacancies). From the plot, it could be observed that, with a higher oxygen volume concentration inside the chamber, the amount of oxygen vacancies ($\sim$ 532 eV) started decreasing as it could be also seen in Fig. 5.21.

In Fig. 5.23, the transmittance curves of the ZnO:Ga layers deposited with different oxygen volume concentrations are shown. In the visible spectrum region (400 to 800 nm), the integrated transmittance was more than 84.2% for all the films. Moreover, in the near infrared spectrum

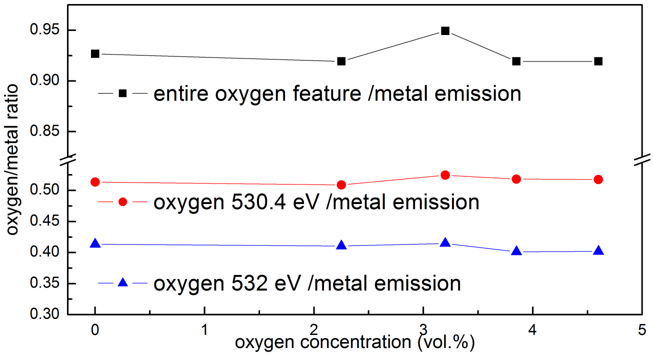

Figure 5.22: Ratio between oxygen and metal emissions against the oxygen volume concentration measured by XPS after etching the surface. The top graph shows the ratio between the entire O 1*s* feature and the metal peaks. The middle graph plots the ratio between the oxygen line at ~ 530.4 eV and the total metal emissions. The bottom graph shows the ratio between the oxygen line at ~ 532 eV and the total metal emission. Lines are added to guide the eyes.

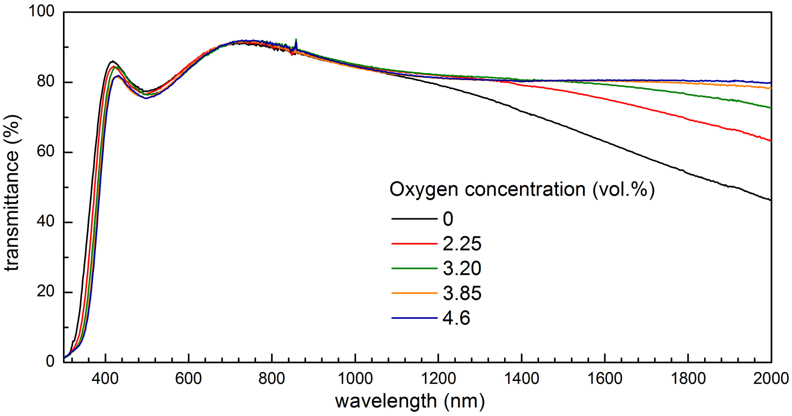

Figure 5.23: The transmittance curves of ZnO:Ga thin films deposited with different O_2 volume concentrations. Lines connecting data points are added to guide the eyes.

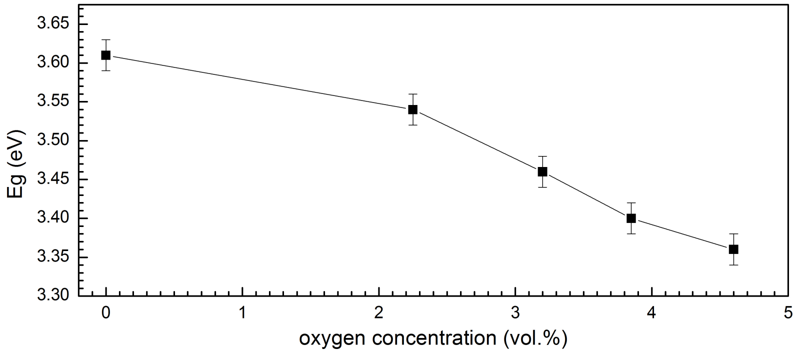

Figure 5.24: Band gap energies of different ZnO:Ga layers deposited under different O_2 volume concentrations.

region, the absorption decreased with the increase of oxygen gas flow. Nevertheless, the transmittance in the region between 800 and 1100 nm, which could be of interest for microcrystalline solar cells, was still above 85.8% even for the layer deposited without oxygen flow. The absorption found at wavelengths longer than 1100 nm for the layers deposited with lower oxygen flows was mainly due to the higher free carriers concentrations as it is shown below. In the ultraviolet spectrum region, the absorption edge shifted towards longer wavelengths as oxygen volume increased.

The absorption coefficient can be calculated from the transmittance and reflectance spectra of the layers. By extrapolating the linear part of the $(\alpha h\nu)^2$ against $h\nu$ plot, the direct band gap energy was determined. The values can be seen in Fig. 5.24. The optical band gap of ZnO:Ga films decreased from 3.61 to 3.36 eV with the increase of oxygen gas flow during deposition.

The electrical properties of ZnO:Ga thin films deposited under different oxygen gas flows are shown in Fig. 5.25. The resistivity exponentially increased one order of magnitude from $1.3\times10^{-3}\ \Omega\,\mathrm{cm}$ to $1.6\times10^{-2}\ \Omega\,\mathrm{cm}$ whereas the oxygen volume in the sputtering chamber only increased from 0 to 4.6%. The carrier concentration was reduced monotonously from 6.0×10^{20} cm^{-3} to 1.2×10^{20} cm^{-3}. In addition, the carrier mobility also dropped from 7.7 cm^{2}V^{-1}s^{-1} to 3.6 cm^{2}V^{-1}s^{-1}. The lower carrier concentration was responsible for the aforementioned shift in the band gap

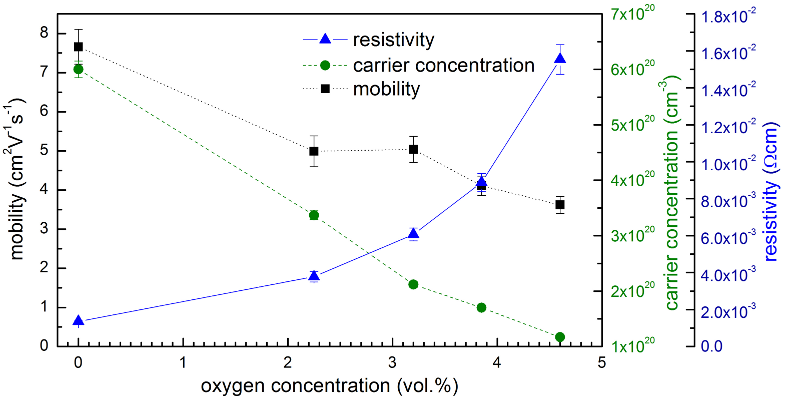

Figure 5.25: The variation of resistivity (triangle) carrier concentration (circle) and mobility (square) of the ZnO:Ga thin films deposited with different O_2 volume concentrations. All the lines are added to guide the eye.

energy. This change in the band gap energy is known as Burstain-Moss [74, 75].

The origin of the electrical degradation with increasing oxygen concentration in similar experiments is attributed to the chemisorption of oxygen at the grain boundaries [40], to the reduction of the oxygen vacancies [78] and to the high energetic oxygen ions bombardment at the substrate [164].

For a conduction mechanism limited by the barrier height at grain boundaries, as expected for the carrier concentration found here [55], the chemisorption of oxygen may have enhanced the amount of trapping states at the grain boundaries giving rise to the barrier height and limiting the mobility.

The oxygen vacancies reduction found by means of XPS can also account for the carrier concentration [78] reduction. When the oxygen gas flow increased during sputtering, the oxygen vacancies were slightly compensated by excessive oxygen atoms as observed in Fig. 5.22. In addition, some authors report that excess oxygen atoms can form ZnO with the interstitially occupied Zn atoms [163]. Both effects could have influenced the further decrease of carrier concentration with the increase in oxygen gas.

Some publications also suggest that high energetic oxygen ion bombardment takes place at the substrate [164] when oxygen gas is used for deposition and this bombardment can degrade the layer growth. Nevertheless, the grain size and microstrain obtained from XRD showed a constant behaviour throughout the whole range studied here suggesting that this effect may play a minor role.

Conclusions

The great variation in electrical properties illustrated that even a small amount of oxygen had an obvious influence on ZnO:Ga thin films. The structure of the samples, studied by XRD, was found to remain almost constant throughout the O volume range used here. The resistivity increased with oxygen concentration until it reached $1.6\times10^{-2}\ \Omega\,\mathrm{cm}$ at 4.6% oxygen volume concentration owing to a reduction in the free carriers (1.2×10^{20}) and the reduction in the mobility ($3.6\ \mathrm{cm}^2\mathrm{V}^{-1}\mathrm{s}^{-1}$). Mainly the oxygen chemisorption at the grain boundaries and the oxygen vacancies reduction with the increase in oxygen volume were responsible for the increase in resistivity. The averaged transmittance in the visible range was above 84.2% and 85.8% in the range between 800 and 1100 nm. The lower carrier concentration moved the plasma frequency toward longer wavelengths and, thus, a lower absorption was observed in the near infrared part of the spectra. However the major improvement in the transmission was in the wavelength range beyond 1100, where thin film silicon solar cells are not active anymore.

6 Co-sputtering of ZnO and ITO

Indium tin oxide composed of In_2O_3 doped with SnO_2 is a TCO widely used as transparent electrode in thin film silicon solar cells or thin film transistors owing to its low resistivity and high transparency. Nevertheless, indium is a scarce and expensive element [26]. Moreover, although not presenting as good properties as ITO, ZnO is a promising and cheaper alternative. Therefore, the strategy was to deposit ITO and ZnO multi-component thin films at room temperature by rf magnetron co-sputtering in order to achieve TCOs with a reduced indium content. The depositions were performed at room temperature to study the properties of the layer which could be later used as the front contact for amorphous silicon *nip* solar cells. The results concerning this chapter were published in three different articles [165–167] and are presented in four different sections, each concerning the structural and morphological, electrical, optical properties and electronic band structure respectively.

Thin films of the quaternary system Zn-In-Sn-O (ZITO) were deposited by rf magnetron co-sputtering of ZnO and ITO in a pure argon gas atmosphere. The technique consisted in the simultaneous sputtering of two targets, and when the sputtered particles reached the surface of the rotating substrate, they nucleated to form a multi-compound material. The targets presented a purity of 99.995% and 99.99% for ZnO and ITO (In_2O_3 with 10 wt.% SnO_2) respectively. A constant rf power of 50 W was used for the ITO target, whereas the rf power to ZnO target was varied from 0 W (pure ITO layer) to 150 W in steps of 25 W. Moreover, a pure ZnO layer deposited at 120 W was used in X-ray photoelectron spectroscopy and electronic band structure studies in order to compare it with the ZITO layers. The target to substrate distance was kept at 11.7 cm, and a substrate rotation of 10 rpm was used to achieve a uniform composition of the films. The substrates used were 5×5 cm^2 *Corning* glass (1737F) and the depositions were performed at a pressure of 0.35 Pa without any intentional heating of the substrate. The deposition time was controlled to achieve a thickness

Name	ITO (W)	ZnO (W)	[In] %	[Zn] %	[Sn] %
ITO	50	0	89.3	0	10.7
ZITO25	50	25	75.5	17.1	7.5
ZITO50	50	50	57.6	36.6	5.8
ZITO75	50	75	46.7	48.5	4.8
ZITO100	50	100	41.8	53.8	4.4
ZITO125	50	125	34.5	62.8	2.7
ZITO150	50	150	30.2	67.3	2.6

Table 6.1: The deposition power used to co-sputter the ZITO set of samples with the corresponding content ratio estimated from XPS.

of 215 ± 20 nm for all the films. Thickness was measured in several points from centre to the border and variations under 3% within the deposition area were found.

6.1 Structure and composition

In this section, the composition of the samples was analysed by using X-ray photoelectron spectroscopy and the structure of the samples was determined by using X-ray diffraction and transmission electron microscopy.

As the power applied to ZnO target increased, the deposition rate increased linearly (see Fig. 6.1) until it reached 6.2 $\mathrm{nm\,min^{-1}}$ at 150 W of ZnO and 50 W of ITO. The deposition rate of pure ITO was of 2.2 $\mathrm{nm\,min^{-1}}$ whereas ZnO presented a deposition rate of 1.2 $\mathrm{nm\,min^{-1}}$ at the same power (50 W). This meant that, while both were sputtered, the ITO content was almost twice for the same power. As the ZnO rf power was increased, the Zn content raised till it overcame the In content, thanks to the increased sputtering rate at higher ZnO powers.

The composition of the films was analysed using XPS and the percentage of cations contained in the layers with the sample identity are shown in Table 6.1. The plot of the Zn content ratio in the film ([Zn]/([In]+[Sn]+[Zn])) against the ZnO power is shown in Fig. 6.1. As the power to ZnO target was varied from 25 W to 150 W, the Zn content ratio varied from 17.1% to 67.3%. The Zn content ratio in the film was found to be proportional to the rf power applied to the ZnO target and hence, either the rf power of

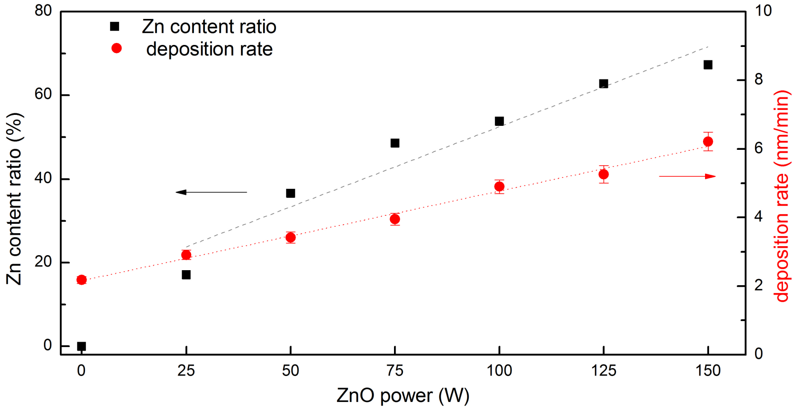

Figure 6.1: The deposition rate of ZITO thin films deposited at different rf powers. Lines correspond to the linear fit of the experimental data.

ZnO or the Zn content ratio could be considered the differential parameter to discuss the film properties.

The content ratio was obtained from the analysis of the core levels photoemission spectra of the ZITO layers measured by XPS and are shown in Fig. 6.2. The graph shows the Zn $2p_{3/2}$, the O 1s, and the In $3d_{5/2}$ photoemission lines. Sn $3d_{5/2}$ lines are not plotted since the signal was low owing to the low Sn concentration (see Table 6.1). The Zn $2p_{3/2}$ sequence showed an increase in intensity with increase in Zn content ratio. This was in direct agreement with the attenuation of the In $3d_{5/2}$ emission line as the In content decreased correspondingly. Both lines showed a shift to higher binding energies as the Zn content increased, however, the shifts were different in magnitude. The In $3d_{5/2}$ line shifted by 0.35 eV, whereas the Zn line exhibited a shift of 0.6 eV between the film with a Zn content ratio of 17.1% and 67.3%. The Zn peak of the final ZnO film had a lower binding energy corresponding to only a 0.2 eV shift relative to the initial 17.1% film.

Fig. 6.3 shows only the O 1*s* emission feature but fitted with three individual lines. The main line at about 530.5 eV corresponded to O^{-2} bonded at fully coordinated metal sites, whereas the line at about 532 eV was related to sites with oxygen vacancies. The third emission feature at

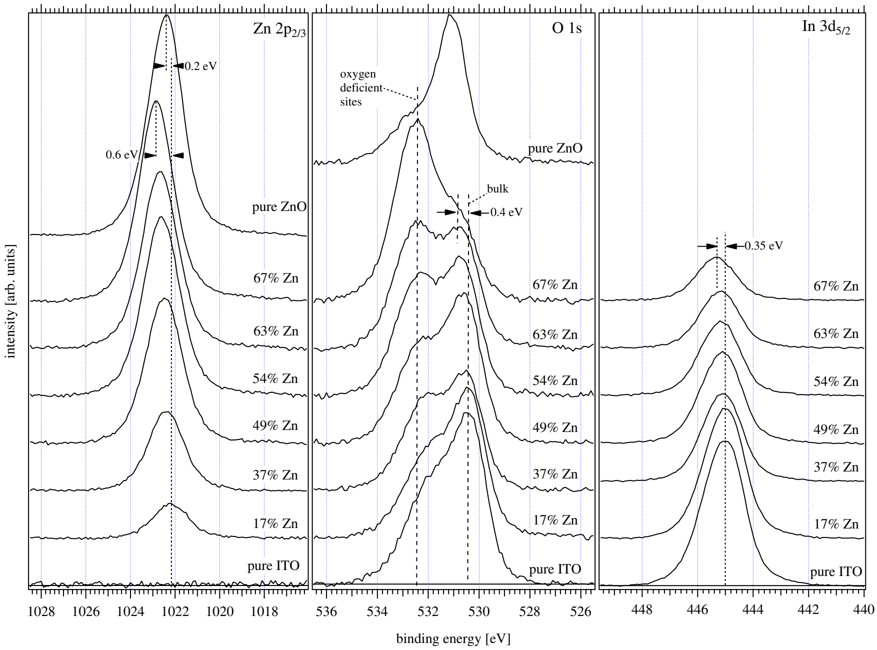

Figure 6.2: Core level photoemission spectra of the ZITO layers measured by XPS. The graph on the left shows the Zn $2p_{3/2}$ peak, the centre graph shows the corresponding O $1s$ emission features and the right hand side shows the In $3d_{5/2}$ spectra.

about 532.6 eV was related to surface contamination (water, OH^-) present on the sample surface after the *ex-situ* solvent cleaning step. Similar O $1s$ emission lines were found in the previous chapter for ZnO:Ga and also in other published works for ZnO:Al [61, 161, 162] and In_2O_3 [168]. It was obvious that, with increasing Zn concentration, the oxygen vacancies related component increased strongly in relation to the 530.4 eV peak. As the Zn content increased, the component related to O vacancies increased its intensity, indicating a higher defect density in these films. The pure ZnO film showed again a smaller 532 eV component. In addition to these stoichiometric changes, the peaks were shifted to higher binding energies similarly to the two metal related lines. The shift of the low binding energy O $1s$ line between pure ITO and pure ZnO was of 0.7 eV.

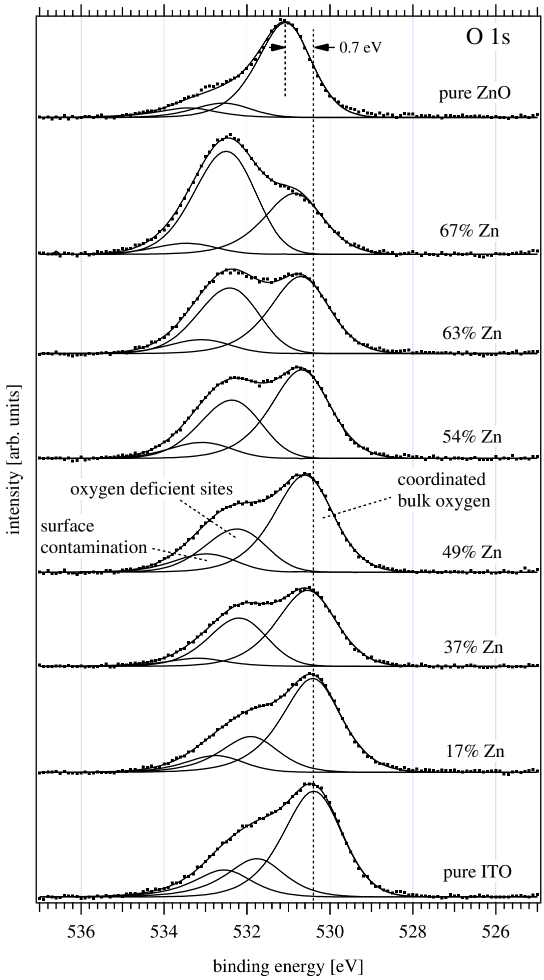

Figure 6.3: Least squares fit of the O 1s emission feature. Three individual lines were fitted reflecting oxygen atoms at fully coordinated metal sites ($\sim$ 530.4 eV), sites with oxygen vacancies ($\sim$ 532 eV), and in the surface contamination layer ($\sim$ 532.6 eV). The main peaks show a shift of about 0.7 eV to higher binding energy.

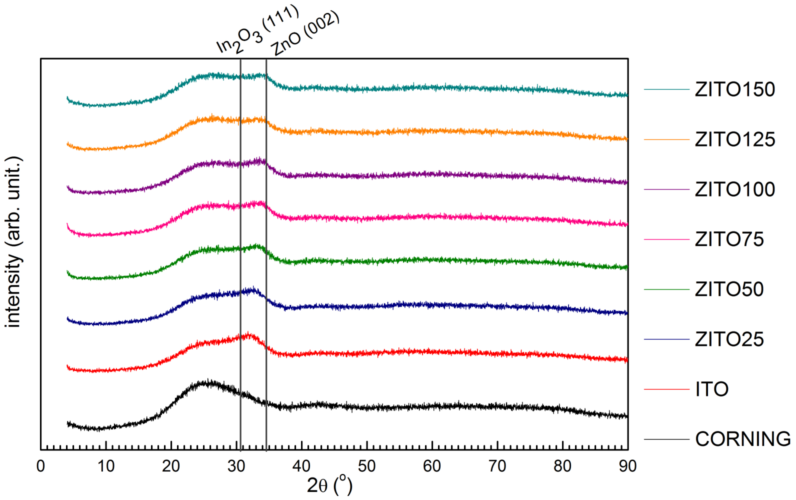

Figure 6.4: XRD patterns of ZITO thin films deposited at different ZnO powers. A line is added to guide the eyes at the standard ZnO(002) peak position [38] as well as at ITO (111) peak position [46].

The shift of the core level lines was likely a result of both stoichiometric and doping density changes influenced by the composition as well as by the density of O vacancies at the film surface.

The XRD profiles of the films are shown in Fig. 6.4. All the films appeared to be amorphous in nature. The broad peak that appeared at around 25^o corresponded to the *Corning* glass. Another halo peak is superposed to the *Corning* one and its maximum varies between 31.7^o for ITO to 33.7^o for ZITO150. This peak shift suggested the presence of a few grains changing its orientation from the ITO bixbyite cubic (222) referenced at 30.6^o [46] to the wurtzite ZnO (001) referenced at 34.4^o [38]. It suggested that some short range order could be present. However, we could not confirm any crystallinity because the peak intensity was too low. Similar XRD spectra have been reported for the for other ZITO samples deposited by co-sputtering [169, 170]. The amorphous structure of the layers could be ascribed to the low temperature sputter deposition. No intentional heating was applied during the growth of the layers and, therefore, species arriving at the substrate had a low adatom mobility to enhance the formation of a polycrystalline layer.

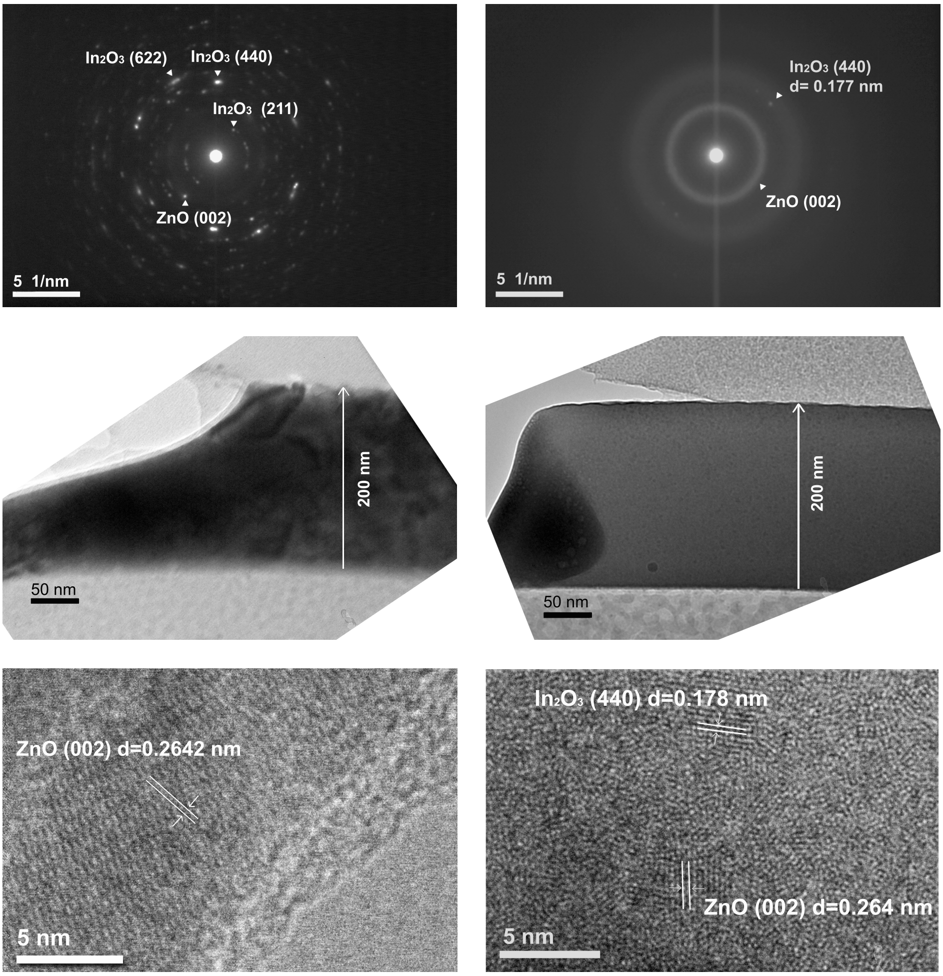

Figure 6.5: Selected-area electron diffraction pattern (top), cross-section view (middle) and HRTEM image (bottom) of ZITO films prepared with 25 W, i.e 17.1% Zn content ratio (left column) and 100 W, i.e. 54% Zn content ratio (right column) ZnO sputtering power.

In order to check whether some short range order was present in ZITO samples, TEM analyses were performed. ZITO25 with a 17.1% Zn content ratio and ZITO100 with a 53.8 % Zn content ratio were carefully prepared for TEM on an insulating substrate (*Corning* 1737F), and the images obtained can be observed in Fig. 6.5.

The left hand side column shows the images corresponding to ZITO25 whereas the right hand side columns shows the ones corresponding to ZITO100. Three micrographs are shown for each sample. The top one corresponds to the selected-area electron diffraction pattern, the second to a cross-sectional view of the samples, and the bottom one is a HRTEM image taken at a magnification of 800 000, where crystallographic planes can be observed. In case of ZITO25, which corresponded to a 17.1% zinc content ratio, the diffraction pattern showed identifiable peaks proving the polycrystalline nature of the sample. The brighter peaks corresponded to In_2O_3 (211), ZnO (002), In_2O_3 (440) and In_2O_3 (622). Every peak could be associated to either In_2O_3 or ZnO, suggesting that no other nanocrystalls of ternary compounds were formed. The fuzzy ring containing each bright peak gave evidence of the amorphous matrix [171] where nanocrystals were embedded. In the cross section view of ZITO25, a 10 nm amorphous initial growth layer was observed followed by a 200 nm film. The thickness was in agreement with the one measured with the profilometer. In the high resolution image, atomic plane distances could be measured. In particular, the ZnO $d_{(002)}$ was identified as 0.264 nm.

ZITO100 showed a different selected-area electron diffraction pattern (right hand side figures). In this case, only a few faint peaks corresponding to In_2O_3 (440) could be seen. The fuzzy rings proved the mainly amorphous character of the layer. In the cross section view of ZITO100, a less porous 200 nm layer can be observed. When going deeper as in high resolution image, a short range order could be observed, where the In_2O_3 $d_{(440)}$ plane distance was measured as 0.178 nm and also the ZnO plane distance $d_{(002)}$ was measured as 0.264 nm. These images confirmed the nanocrystalline growth of the material, where approximately 2 nm crystals were grown embedded in an amorphous matrix.

With these images we showed that, although the samples seemed to be amorphous by XRD, they contained small nanocrystals as could be deduced from TEM images. Just two samples were measured, and conclusions regarding the evolution of the structure were difficult to draw. Even though, it seemed that increasing zinc content led to a more amorphous material, where still a low range order was present.

The presented results had a remarkable importance given that no other TEM images are reported on ZITO samples. It is worth mentioning that the preparation of the samples implied not only mechanical but also ion milling to obtain layers thin enough to be observed by means of TEM. The process was developed under liquid nitrogen cooling and at low voltage. Therefore, no structural change was expected during this process. However, the electron irradiation in a transmission electron microscope environment is reported to enhance crystallisation [172]. Consequently, the observed nanocrystallinity may be the result of the exposure of the thin layers to electron irradiation. Nevertheless, both samples were equally prepared, and results are still different. The sample with the lowest Zn content ratio presented a higher crystallinity as deduced from the selected-area electron diffraction pattern. Moreover, the existence of nanocrystals was already suggested from the observation of XRD spectra. Then, although crystals may be enhanced by electron irradiation some of them could be previously present.

6.2 Electrical properties

Amorphous oxide semiconductors formed by Zn, Sn or In are said to present relatively high mobilities regardless their structure because the bottom of the conduction band is formed by spherically symmetric 4s or 5s orbitals with isotropic shapes and, therefore, direct overlap with next 4s or 5s orbital is possible [173, 174]. This property allows them to behave similarly to its polycrystalline phase. Therefore, presenting an amorphous structure, as it was previously found, it is not expected to be a disadvantage.

The electrical properties were mainly studied by means of Hall effect measurements. The Hall coefficient showed a negative sign, thus, the carriers responsible for conduction were electrons. The as-deposited ITO film presented a resistivity of 7.58×10^{-4} $\Omega\,$cm as shown in Fig. 6.6. The resistivity of the as-deposited ZITO samples slightly decreased as we started introducing Zn, reaching a minimum value of 6.6×10^{-4} $\Omega\,$cm for a ZnO power of 25 W corresponding to a Zn content ratio of 17.1%.

From a Zn content ratio of 36.6% onwards, the resistivity of the films increased. The sample with the highest content ratio (67.3%) showed a

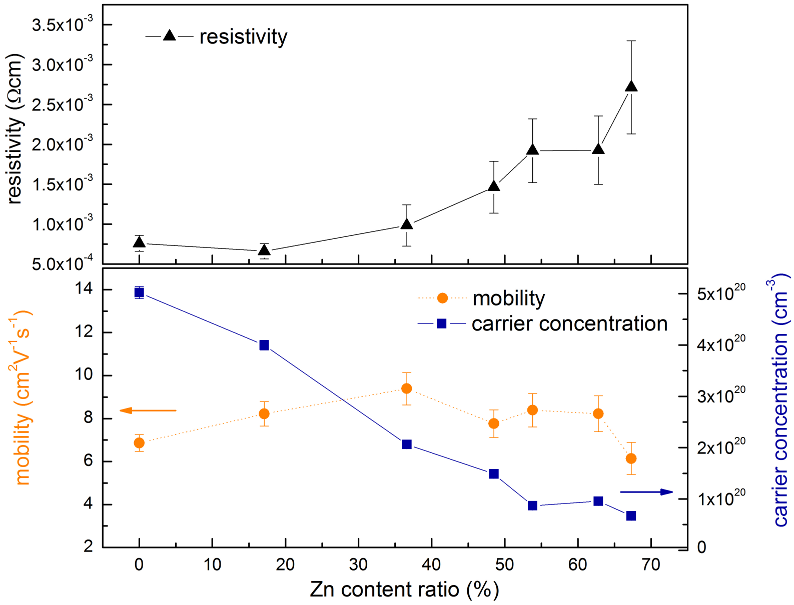

Figure 6.6: The resistivity (top graph triangles), carrier concentration (bottom graph squares) and mobility (bottom graph circles) of the ZITO thin films with different Zn content ratio. All the lines are added to guide the eye.

resistivity as high as $2.7{\times}10^{-3}$ Ω cm. As it can be observed in Fig. 6.6, the charge carriers concentration was found to decrease with the increase in Zn content ratio. The lowest carrier concentration was found to be $6.7{\times}10^{19}$ cm^{-3} for the sample with a 67.3% Zn content ratio whereas the as deposited ITO film showed the highest carrier concentration of $5.0{\times}10^{20}$ cm^{-3}.

The Hall mobility of the ZITO films is also shown in Fig. 6.6. No clear trend could be observed with the increase in Zn content. Nevertheless, the mobility slightly increased until it reached 9.4 $\mathrm{cm}^2\mathrm{V}^{-1}\mathrm{s}^{-1}$ for a Zn content ratio of 36.6% and then slightly decreased reaching 6.1 $\mathrm{cm}^2\mathrm{V}^{-1}\mathrm{s}^{-1}$ for a Zn content of 67.3%. The slightly improved mobility observed for the sample with a 17.1% Zn content ratio explained the drop in resistivity measured for that sample.

The lower resistivity observed for low Zn addition (sample ZITO25) was also found by Minami *et al.* [28], Liu *et al.* [175] and Heo *et al.* [169]. Although the Zn concentration values that led to a minimum in resistivity were different in the aforementioned publications, the deposition conditions also vary among these authors. Nevertheless, it seems that a low content of Zn (between 7% and 36%) improved the electrical properties of ZITO in comparison to ITO. Liu *et al.* [175] and Minami *et al.* [28] suggested that the improved resistivity of the ZITO films in comparison to ITO might have been caused by the formation of an amorphous-like ternary compound of $Zn_2In_2O_5$ [175]. However, TEM images did not give evidence of the creation of a ternary compound. At least, any nanocrystal composed of a ternary compound was detected. The low adatom mobility of the incoming species (owing to room temperature deposition) may have prevented the growth of a more complex compound.

For ZITO layers with a Zn content ratio of 36.6% and higher, the increase in resistivity was mainly owing to a decreasing amount of charge carriers as observed in Fig. 6.6. Given that the free carriers in an ITO film are originated from oxygen vacancies and Sn^{4+} ions substituting In^{3+} ion sites, the addition of co-sputtered ZnO material might have resulted in either filling up the oxygen vacancies or the compensation of the extrinsic dopants. In the latter, Zn^{2+} ions would occupy the In^{3+} ion sites resulting in a decrease in carrier concentration. In this case, Zn^{2+} could compensate the extra electrons delivered by the substitution of In^{3+} by Sn^{4+}.

An increasing oxygen concentration during deposition might have diminished the carrier concentration by extinction of oxygen vacancies and also by the electron trapping due to the chemisorption of oxygen within the film and/or at the surface of the films. Nevertheless, the proportion of metal to oxygen is lower in case of ZnO (1:1) in comparison to In_2O_3 (2:3). Thus, the expected mechanism causing the reduction of carriers was thought to be the increase in the amount of Zn^{2+}, which could compensate the extra electrons delivered by the substitution of In^{3+} by Sn^{4+}, rather than the filling of the oxygen vacancies.

Although the mobility did not show a notable trend, the values were similar to those found in Chapter 5 for polycrystalline ZnO:Ga layers. The electrical properties can be understood in terms of the working hypothesis of wide band gap conducting oxides [170, 173, 176]. Inverse photoelectron and molecular orbital studies show that the density of states of the bottom of the conduction band of amorphous TCOs are almost the same as in

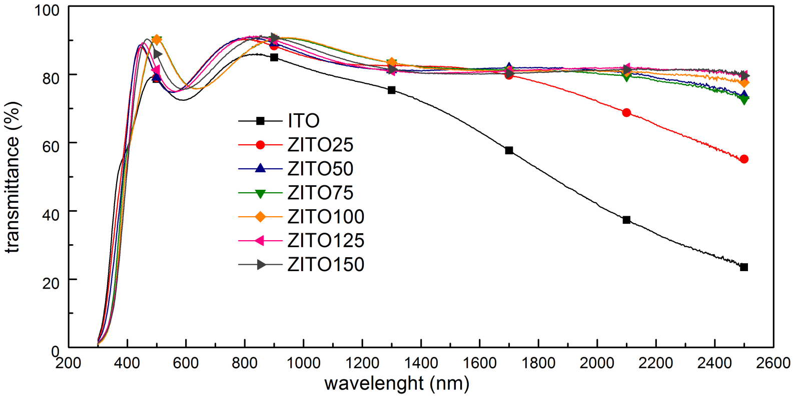

Figure 6.7: The transmittance curves of ZITO thin films deposited with different ZnO powers.

the crystalline material [174, 177]. The particular morphological change observed by TEM did not affect the mobility. Concretely, the samples analysed by TEM with a Zn content ratio of 17.1 and 53.8% showed as similar mobility values as 8.2 $cm^2V^{-1}s^{-1}$ and 8.4 $cm^2V^{-1}s^{-1}$ respectively.

6.3 Optical properties

The optical properties of the films were analysed by using the transmittance (Fig. 6.7) and reflectance spectra in the range between 300 and 2500 nm. The ITO film showed an integrated transmittance of 75% in the visible wavelength range (400-800 nm), whereas the ZITO samples showed a transmittance above 80% for all the Zn content ratios in the same range. As usual in TCO materials, a drastic drop in transmittance can be observed for all the layers in the low wavelength range caused by the band to band absorption. Moreover, the ZITO films showed an improved transmittance in the near infrared region when the Zn content ratio in the film increased.

The higher transmittance in the long wavelength range was mainly caused by the reduction of free charge carriers with increased Zn content ratio. This reduction of free carriers moved the plasma absorption edge to-

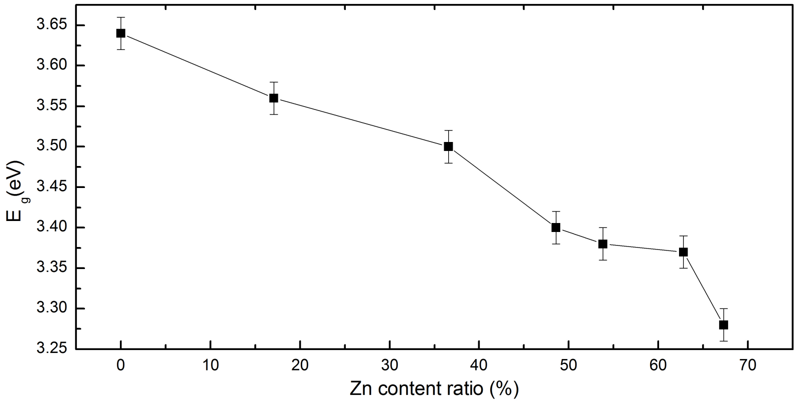

Figure 6.8: Band gap energies of the different ZITO layers deposited at different ZnO target rf powers.

ward longer wavelengths and, thus, a lower reduction of the transmittance could be observed in the range analysed here.

The lower transmittance measured in the visible range in case of ITO layer is often reported [168] when oxygen is not added to the sputtering chamber. The transmittance of the ITO layer used for this experiment could have been further optimised by using a small concentration of oxygen gas during deposition, and it would have reduced the optical differences between the ITO and the ZITO transmittance curves.

The absorption coefficient was determined from the transmittance and reflectance values by means of Eq. 2.4 assuming that the material was a direct band gap semiconductor. The optical band gap energies of the films were deduced from $(\alpha h\nu)^2$ against $h\nu$ plots and can be observed in Fig. 6.8. The ITO film showed a band gap of 3.64 eV and the band gap energy of ZITO films were found to decrease with the increase in Zn content ratio. The lowest value of 3.28 eV was obtained for ZITO150 film with a Zn content ratio of 67.3%. This band gap shrinkage can be understood in terms of the Moss-Burstein effect [74, 75]. The band gap shift caused by Moss-Burstein effect usually appears in heavily n-doped materials because the Fermi level lies in the conduction band and the filled states block thermal or optical excitation. As a consequence, the measured band gap moves to higher energies as carrier concentration increases as it happened for this set of samples. Moreover, since the band gap of ZnO ($\sim$ 3.3-3.4 [55]) is lower than that of In_2O_3 ($\sim$ 3.6 eV [178]), an increase in zinc content (relative decrease in indium content) is expected to lead to a band gap shrinkage since, as expected from TEM, the two materials are mixed in the layer [170, 179]. These results proved that the band gap of the films can be easily tuned by just varying the Zn content ratio.

6.4 Electronic band structure

The objective of the present section is to characterise the electronic structure (i.e. work function and band edge energies) of ZITO thin films in order to assess their suitability for electrode applications. A secondary focus of this section was directed towards the investigation of the measurement technique itself.

UPS is the standard technique used to characterise the work function of surfaces given that absolute values can be obtained. However, research has demonstrated that UPS measurements on metal oxide surfaces can result in a lowering of the work function caused by the measurement itself [130–133]. These experiments suggested that this phenomenon is likely caused by the formation of a surface dipole owing to the photochemical hydroxylation of the surface by UV photons during the UPS measurement. Although the artifact occurs instantaneously during UPS characterization (i.e. cannot be detected by UPS itself), it was possible to identify its magnitude through low intensity X-ray photoemission spectroscopy, whereas only exposes the surface to magnitudes lower photon fluxes while still enabling the determination of the work function. Hence, another objective of the presented research was to investigate whether ZITO surfaces were prone to this artifact. In this context, LIXPS measurements were performed on all of the investigated films prior to the standard UPS measurement.

The samples used for this study were the set of ZITO layers deposited at UB and discussed in previous sections. However, the measurements presented here were performed at the University of South Florida (USA), and the results were published in [166]. The experimental conditions of the electronic band structure measurements are detailed in Sec. 3.4.5.3.

A summary of the UPS measurements can be found in Fig. 6.9. The bottom spectra correspond to the pure ITO film, while the subsequent

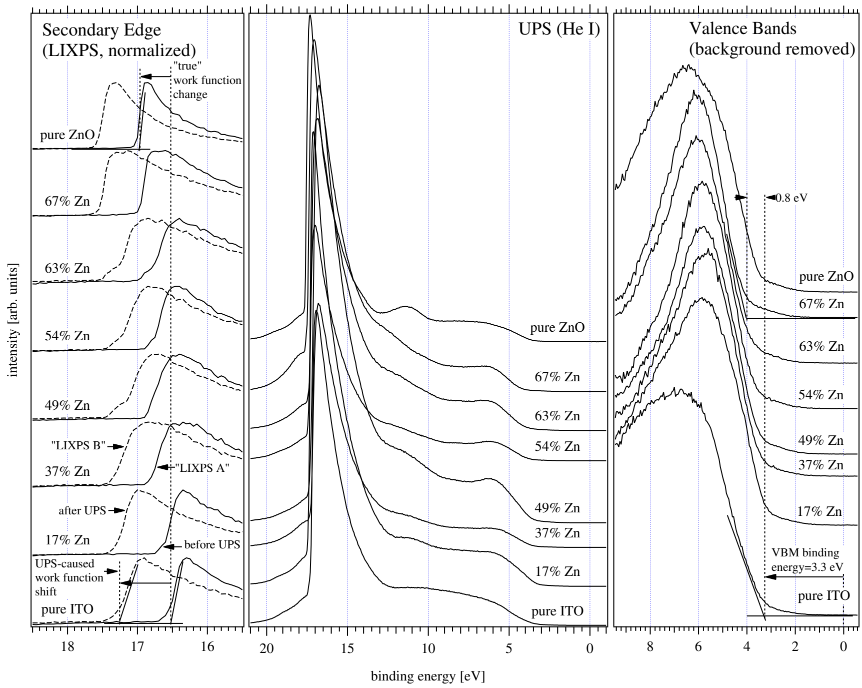

Figure 6.9: Work function and valence bands characterisation. On the left the LIXPS A and B measurements. The UPS raw data is depicted in the central graph. The valence band region measured by UPS is magnified and with the inelastic background removed on the right hand side of the graph.

spectra reflect the films with higher Zn content. The top spectra correspond to the pure ZnO film. The graph on the left shows the normalised secondary edge spectra measured with LIXPS before (LIXPS A) and after the UPS measurement (LIXPS B). The observed shift of the order of 0.5 eV to higher binding energy from A to B measurements is a result of the work function reduction due to UV-induced surface hydroxylation during the UPS measurement. However, it was also obvious that the initial LIXPS A cutoffs shifted to a higher binding energy, thus, reflecting a real work function reduction as the Zn content increased. The work function change between ITO and ZnO is about 0.4 eV. The central graph shows the raw UPS data. The strong feature at ~17 eV binding energy is the secondary edge cutoff, which allows the determination of the work function of the samples. The energy range between 0 and ~10 eV corresponds to the valence bands density of states of the samples. Part of this range is shown magnified and with the inelastic background removed on the right hand side of Fig. 6.9. A distinct change of the density of states could be observed as the Zn concentration of the films changed. Also, a shift of the valence band maximum to higher binding energy was observed.

The evaluation of the UP- and LIXP-spectra shown in Fig. 6.9 yielded the work function and the VBM energy for each of the investigated films. In addition, using the optical band gap energies for each of the ZITO compositions found in the previous section, the respective conduction bands minima (CBM) can be also estimated for each film. The results of this evaluation are shown in Fig. 6.10. The top part of the figure shows the evolution of the work function depending on the composition of the films. The solid round markers correspond to the work function values measured during the initial LIXPS A, before the performance of the UPS. The open markers correspond to the work function values determined from the second LIXPS B measurement, after the UPS characterization. The two dashed lines correspond to least square fitted lines into each of the two sets of values. The lines indicate that the overall work function change caused by the UPS measurement is reduced as the Zn concentration increased. However, the overall values in the range of ~ 0.4 - 0.6 eV are in good agreement with values previously seen for this artifact on ITO and TiO_2 surfaces [130–132]. In these previous studies, it was found that the UV or X-ray photons cause a photochemical surface hydroxylation resulting in a uniform dipole potential across the surface. This effect lowers the work function since the attached -OH groups are oriented with their positive hydrogen end away from the surface.

To further evaluate the electronic structure of the investigated films, the work function values estimated from LIXPS A were used since they yield the *true* work function of the samples. By direct comparison of LIXPS with in-situ Kelvin probe measurements, it was proved that the technique do not alter the work function significantly during the short and weak X-ray exposure needed for a single LIXPS scan [130]. Fig. 6.10 shows that the work function of the films drops by about 0.4 eV between pure ITO and pure ZnO. The absolute values range varied from 4.74 eV for pure ITO to 4.30 eV for pure ZnO.

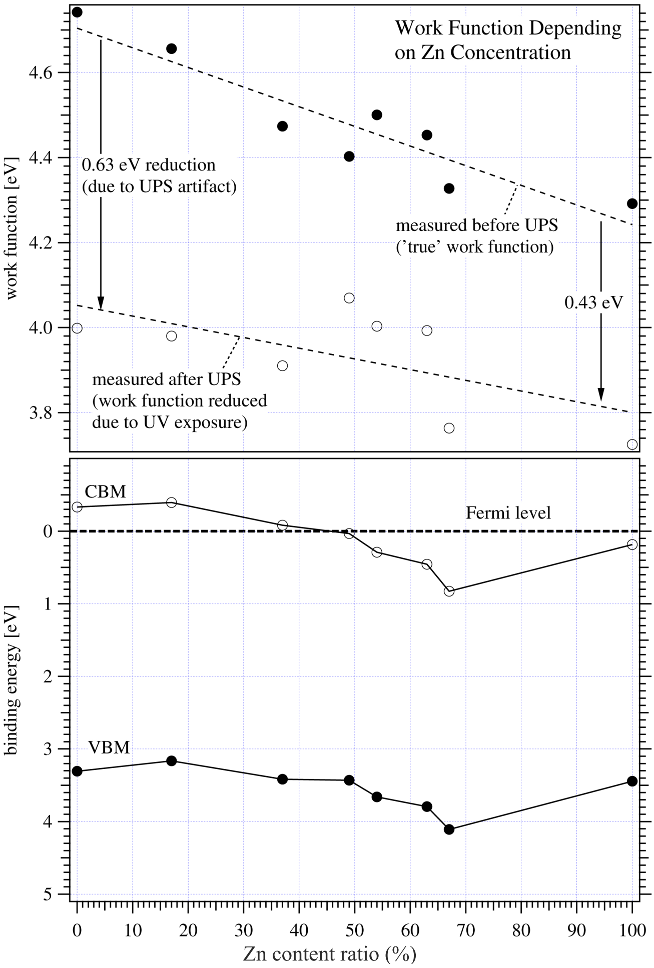

Figure 6.10: The top graph shows the work function values derived from the LIXP-spectra measured before (full circles) and after (open circles) the UPS measurement. The bottom graph shows the corresponding values for the VBM binding energy (full circles) as determined from the low binding energy cutoff position of the UP-spectra. The associated CBM energies are also shown (open circles).

These values fall into the range of work function values established previously for these materials. The work function value of the pure ITO sample is similar to values previously measured on ex-situ cleaned thin films [130, 131, 180]. Scanning Kelvin probe measurements by Chen on ITO films yielded values ranging from 4.28 to 4.86 eV depending on the surface treatment [181]. Previous work function measurements on pure ZnO by Kelvin probe yielded values between 4.45 eV and 4.50 eV [182], which were close to the value of 4.3 eV that we obtained. Klein *et al.* [183] investigated a variety of in-situ deposited ZnO layers at room temperature and measured work functions ranging from 4.3 to 5.2 eV, depending on the oxygen deficiency of the films. The same publication gives values between 3.8 and 4.7 eV for in-situ prepared In_2O_3 co-doped with 10% Zn and 30% Sn, which covers the range of WFs found here (4.4 to 4.7 eV).

The bottom part of Fig. 6.10 shows a graph where the VBM and CBM are plotted *vs.* the Zn concentration. The full markers show the VBM values determined from the valence band edge cutoff of each of the spectra shown in Fig. 6.9. The corresponding CBM energies were obtained using the optical band gap values determined in the previous section via UV-VIS spectroscopy (Fig. 6.8). The graph shows that as the Zn concentration is increased in the ITO film, the VBM shifts to higher binding energies. It corresponds to an upwards shift of the Fermi level in the band gap. The Fermi level position is indicated as a dashed line in the graph. The results suggested that the Fermi level entered the conduction band at around the 50% Zn concentration point. As the concentration further increased, the Fermi level advanced deeper into the conduction band. In the case of the pure ZnO film, the Fermi level was again close to the CBM. This observation was in tune with the increase of the O-vacancy related O 1s surface peak previously presented in Fig. 6.2. The increase in O vacancies with the Zn concentration resulted in degenerate doping levels. Recent data by Klein *et al.* [183], where ZnO films were prepared by magnetron sputtering with varying oxygen content, demonstrated that highly oxygen deficient films show degenerate doping levels.

From Fig. 6.3 (presented in previous sections) it was shown that, with increasing Zn concentration, the oxygen vacancies related component increased strongly in relation to the 530.4 eV peak. This is also shown in Fig. 6.11 where the oxygen/metal intensity ratios are plotted for the 530.4 eV and the 532 eV peaks. The ratios are relative to the combined Zn-In

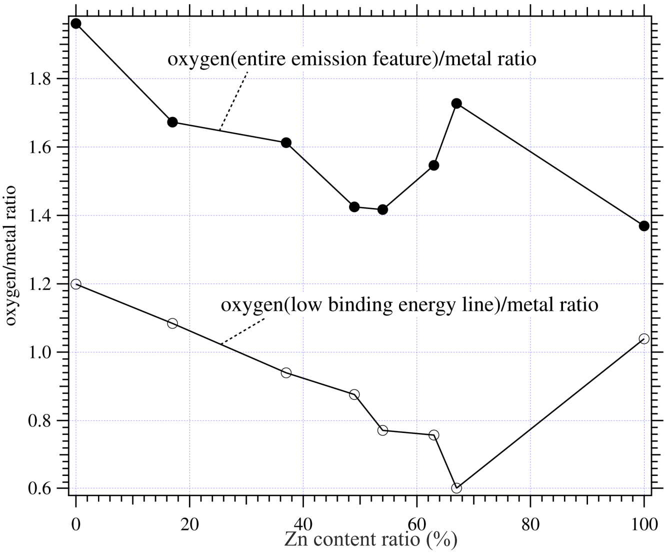

Figure 6.11: Ratio between oxygen and metal emissions depending on the Zn concentration. The lower graph (open circles) plots the ratio between the oxygen line at ~ 530.4 eV and the total metal atom emissions vs. the Zn concentration. The top graph shows the ratio between the entire O 1*s* feature and the metal peaks.

metal peak intensity (except for the pure films). The concentration of Sn was not included owing to the low concentration and, thus, large error of the measurement. These curves clearly showed that the oxygen deficiency rose as the Zn content increased, which was in good agreement with the Fermi level rise within the band gap. It is interesting to note that the defect level was considerably lower for the ZnO film, which was probably related to the fact that alloys typically have higher defect densities than their associated pure compounds.

All the core level peaks showed significant shifts to higher binding energy with the increase in Zn concentration (Fig. 6.2). The Zn 2*p* peak shifted by 0.6 eV between 17.1% and 67.3% Zn concentration, whereas the In 3d peak shifted by 0.35 eV between pure ITO and the 67.3% ZITO film. On the other hand, the oxygen related emission lines exhibited a gradual shift from pure ITO to pure ZnO of about 0.7 eV. Part of the shift was related to the change of the average charge localised on oxygen and metal sites due to the changing chemical environment and the different oxygen vacancy density depending on the Zn concentration. A second effect that played a role was most likely the vacancy density related Fermi-level shift into the conduction bands, which increased the binding energy of the core levels of all atomic species present in the samples. Likewise, the observed core level shifts were caused by both chemical changes and Fermi level shifts.

The final point of this discussion concerns to comparing the surface related data presented here with the investigation of the bulk properties discussed in previous sections. In Sec. 6.2 it was shown that the carrier concentration was reduced with increasing Zn content. This was in direct disagreement with the Fermi level shift into the conduction band observed at the sample surface, which suggested a strong increase in the carrier density driven by an increase in oxygen vacancies. Furthermore, it was found that the absorption edge (optical band gap) of the ZITO multi-compound was reduced by about 0.4 eV between the pure ITO film and the 67.3% Zn concentration layer. The surface results presented here would suggest that the absorption edge of those films, where the Fermi level entered the conduction band, should shift to larger energies (or shorter wavelengths, respectively) due to the Burstein-Moss effect [74, 75] where occupied states at the CBM prevent transitions from the VBM to the CBM resulting in the larger band gap measured.

Given the large disagreement between photoemission measurements and the bulk results presented in previous sections, XPS was performed after etching the ZITOs samples surface. LIXPS or UPS could not be performed anymore, thus, the electronic band structure cannot be detailed. The core levels of the ZITO samples were characterised after etching the samples surface during 5 minutes with Ar atoms. The obtained O 1s spectra, as well as the fitting of the peak, can be observed in Fig. 6.12. The peak at $\sim$ 532.6 eV, corresponding to oxygen atoms loosely bonded to contaminants such as -OH, which was observed in Fig. 6.3, was not present in bulk measurements. This effect was also found in [161] for ZnO:Al, as well as in the previous section for ZnO:Ga. As soon as the surface was etched, the peaks associated to contamination disappeared. Moreover, the intensity of the $\sim$ 532 eV peak, associated to sites with oxygen vacancies decreased dramatically when comparing to surface measurements. It indicated that the bulk was not as oxygen deficient as the surface. As the Zn content ratio

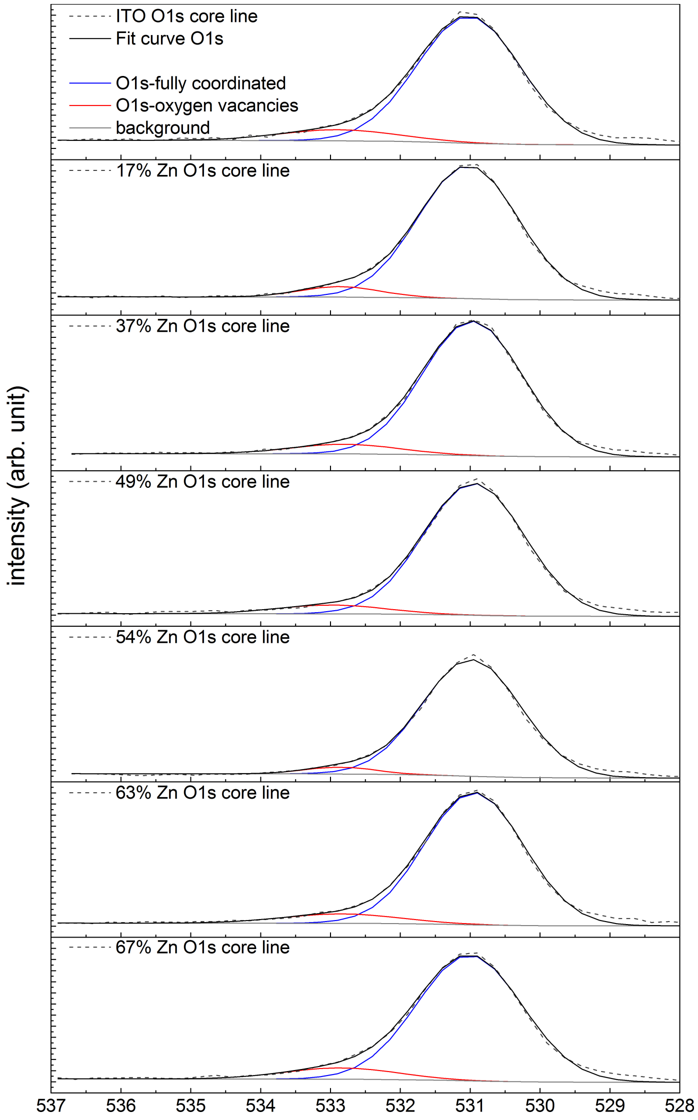

Figure 6.12: Gaussian fit of the O 1*s* emission feature. Two individual lines were fitted reflecting oxygen atoms at fully coordinated metal sites (∼ 530.4 eV) and sites with oxygen vacancies (∼ 532 eV).

increased, the oxygen peak related to sites with oxygen vacancies varied slightly, but no clear trend as the one found at the surface could be found. The peak related to oxygen deficiency sites is much smaller in bulk than at the surface suggesting that many oxygen vacancies can be found at the surface but not anymore in the bulk of the material.

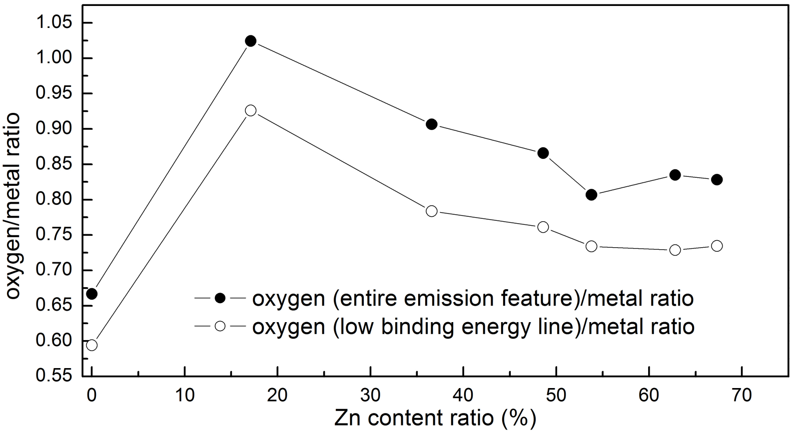

Figure 6.13: Ratio between oxygen and metal emissions depending on the Zn concentration after etching the samples surface. The lower graph (open circles) plots the ratio between the oxygen line at ~ 530.4 eV and the total metal atom emissions vs. the Zn concentration. The top graph shows the ratio between the entire O 1*s* feature and the metal peaks.

In Fig. 6.13 the oxygen/metal ratios are plotted for the 530.4 eV and the whole O 1*s* peak (530.4 and 532 eV). The ratios are relative to the combined Zn-In-Sn metal peak concentration. Both curves show a similar behaviour, indicating that the oxygen vacancies did not play an important role. The ITO layer showed the lowest oxygen to metal ratio. It suggests that a higher amount of metal is non oxidised in the bulk of the ITO layer as it was commented in Sec.6.3 as a plausible explanation for the low transmittance of ITO in comparison to ZITO. As soon as Zn was added to the layer, the ratio between oxygen and metal increased considerably and afterwards, it started decreasing smoothly like it happened at the surface.

The only way to explain the discrepancy between the carrier concentration and the electronic band structure detailed at the beginning of this

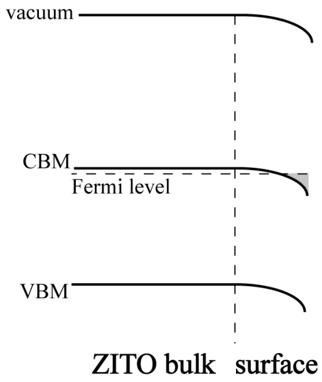

Figure 6.14: Electronic structure at ZITO film surface. A high oxygen vacancy density at the surface causes the Fermi level to enter the conduction bands.

section was to realise that the results reflect bulk properties, whereas the photoemission spectroscopy data presented (work function, VBM, CBM, and surface XPS surveys) were related to surface properties. This, in combination with the bulk XPS results presented above, allowed the conclusion that the vacancy density of the investigated ZITO films was higher at the surface than in the bulk, which gave rise to a highly conductive surface layer on top of a less conductive bulk phase. This is shown schematically in Fig.6.14. The Fermi level entered the conduction band in the surface layer resulting in a thin degenerately doped layer.

Conclusions

Zinc indium tin oxide transparent conducting thin films with varying Zn concentration were investigated, and their structural, optical and electrical properties, as well as their electronic band structure were discussed. A set of amorphous layers containing embedded nanocrystals were obtained and characterised by means of XRD and TEM. The resistivity of the ITO layer decreased with the incorporation of a 17.1% of Zn, but then it increased with higher Zn content ratios. The lowest resistivity was of $6.6\times10^{-4}\ \Omega\,\mathrm{cm}$. The mobility of the layers remained almost constant, whereas the carrier concentration decreased with the introduction of Zn reaching 6.7×10^{19}

cm^{-3} for a Zn content ratio of 67.3%. The probable reason for such a degradation must be the substitution of In^{3+} by Zn^{2+}, which compensated the Sn^{4+} doping in ITO layers. As soon as Zn was introduced in the films, the optical transmittance was considerably improved in the visible wavelength range due to the higher oxygen content in ITO films. The band gap of the layers varied between 3.64 eV for ITO to 3.28 eV for the layer with a Zn content ratio of 67.3%.

By means of X-ray and UV photoemission spectroscopy, the electronic band structure was studied. The measurements showed that, with the increase in Zn concentration, the oxygen vacancy concentration at the surface increased resulting in a degenerately n-doped surface layer. At the same time, the work function decreased from to 4.7 to 4.3 eV. Comparison with bulk XPS measurements and with optical absorption and carrier density measurements allowed the conclusion that the degenerately doped region was confined to a thin surface layer. Additionally, the experiments demonstrated that the work function of ex-situ cleaned ZITO surfaces was reduced by about 0.5 eV during UPS measurements, similar to what was observed earlier on other metal oxide surfaces.

7 Application of ZnO in the back reflectors for amorphous silicon *pin* solar cells

The aim of this chapter is to compare Ga-doped ZnO and Al-doped ZnO layers for the back contact in hydrogenated amorphous silicon solar cells. The objective is to improve the complete device behaviour on a laboratory scale by improving the transparent conducting oxide layer located at the back side of the cell.

TCOs were grown onto state-of-the-art *pin* structures prepared by T-Solar Global S.A. in its production line and lately also onto *pin* structures fabricated at the Universitat de Barcelona. Apart from comparing ZnO:Al and ZnO:Ga, the interfacial problems derived from the long exposure of a-Si:H surfaces to the environment prior to the back reflector deposition, are discussed.

7.1 Role of the back reflector

On the rear side of an a-Si:H *pin* solar cell, an electrode must be deposited to collect the photogenerated current (see Sec. 2.5). It generally consists of a TCO/metal double structure known as back reflector. Ag or Al is chosen as the metal electrode whose purpose is to collect the electrons and reflect the light not absorbed in the cell, so that it can have a second chance to be absorbed. The TCO layer between the n-layer and the metal prevents the diffusion of the metal into the cell and acts as an optical spacer, enhancing the reflectance thanks to its intermediate refractive index. The use of a TCO at the back side of the cell implies a considerable gain in photocurrent, caused by the increased conversion at long wavelengths. The combination of a TCO and a metal back reflector was patented by Ullal in 1991 [30]. Generally, both layers are deposited by sputtering.

The back reflector is an essential constituent of the light-trapping scheme of thin-film silicon solar cells. When a TCO is used as a back reflector, it must fulfill certain conditions. Its refractive index must be between that of silicon (~ 4) and that of the metal (~ 1) to enhance the reflectance [184]. Moreover, the lower the refractive index, the higher the energy of the surface plasmonic absorption at the metal interface [185, 186]. Furthermore, it must be electrically conductive to avoid a decrease in the cells fill factor [187]. Finally, it has to be highly transparent in the near-infrared range to avoid absorption by free carriers. In the case of a-Si:H, it is enough if the layer is transparent up to 800 nm. If microcrystalline silicon (μc-Si:H) is used, the TCO should be transparent until 1100 nm. Moreover, non aggressive deposition conditions must be chosen to create a defect-free interface.

When light goes through a flat multilayer stack, it is partly reflected and partly transmitted at each interface. The reflected light from the upper and lower surfaces interferes if the film is thin enough to keep the coherence of the incoming light. Therefore, the thickness can be optimised to obtain the highest reflectance of the BR at a certain wavelength. In case of a-Si:H, given that the absorption coeficient drops from 600 nm onwards, it is interesting to reflect the light in that range so that light goes through the device again.

The BR deposition parameters cannot be freely chosen given that the sequence of this deposition is after the deposition of the active layers of the cell. Therefore, the deposition temperature cannot be above the *pin* deposition temperature ($\sim 200^{\circ}$C) and the sputtering pressure and power should be controlled to avoid ion bombardment and, thus, prevent the creation of a defective interface. The range of pressures used here is the same as the one chosen in Sec. 5.1, i.e. between 0.07 and 0.53 Pa. The use of 0.13 Pa led to the best electrical properties but also implied a high dc voltage. Therefore, higher pressures are preferred since the particles will reach the surface with less energy.

The TCO layers studied in the previous chapters were deposited by means of rf magnetron sputtering. However, for the back reflector deposition, dc magnetron sputtering was used. With the equipment used at UB, the dc power source led to a better performance of the solar cells. In fact, using rf sputtering, the cells appeared to be short circuited. Instead, using dc sputtering, the cells worked well. The reason was uncertain, and probably further optimisation of the conditions were needed. In case of rf sputtering, a higher plasma density appears next to the substrate [55]. Such a plasma density next to the substrate might have caused some trouble when the TCO was sputtered on top of the *pin* structure. To discard problems caused by rf, dc was always used for the BR deposition. Moreover, the use of dc was advantageous since TS has a dc sputtering equipment and the improvements found at UB could be lately performed at their factory.

Regarding the metal layer, it must present a high reflectivity, especially at the initial growing stage where the reflection takes place. Trials comparing silver and aluminium, which are the most commonly used materials, showed an increase of the generated photocurrent when silver is used [20]. Nevertheless, the use of silver implies a large increase in the production cost and, therefore, industrial modules are preferably finished with aluminium [20].

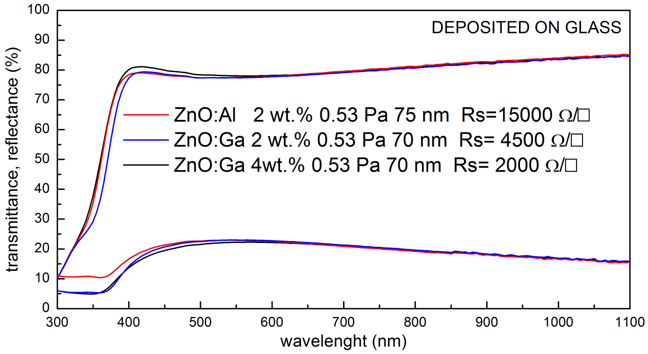

Figure 7.1: Transmittance and reflectance of ZnO:Al and ZnO:Ga layers deposited on glass.

ZnO:Al is normally used as back reflector and its suitability is extensively proved [20, 21]. In this work, ZnO:Ga and ZnO:Al are used in order to compare both materials. When ZnO:Ga and ZnO:Al layers were deposited under the same conditions over glass they showed similar optical properties but ZnO:Ga presented a better electrical performance. In Fig. 7.1, the transmittance and reflectance of 70-75 nm layers of ZnO doped with a 2 wt.% of Al_2O_3, and a 2 and 4 wt.% of Ga_2O_3 are shown. As shown in the figure, the curves are identical in the long wavelength region (600-1100 nm), where the TCO must be as transparent as possible. In the short wavelength range, (300-600 nm) slight differences in transmittance and reflectance are found, which are due to slight differences in thickness and to the different band gaps of the layers. Regarding the electrical properties, the layer doped with a 2 wt.% of Ga_2O_3 instead of a 2 wt.% of Al_2O_3 showed a sheet resistance 3 times lower. Similar doping amounts led to better electrical properties when Ga_2O_3 was used. Moreover, when a 4 wt.% of Ga_2O_3 was used, the sheet resistance was 7 times lower in comparison to 2 wt.% of Al_2O_3. Higher doping concentrations of Al_2O_3 were not tried. In this study, the ZnO back reflectors are deposited from ZnO targets with a 2 wt.% of Al_2O_3 or with a 2 or 4 wt.% of Ga_2O_3.

7.2 Deposition of back reflectors onto industrial *pin* coupons

The application feasibility of the studied TCO layers was proved onto devices fabricated by T-Solar Global S.A. in the framework of the European project HELATHIS. TS provided us with 10 × 10 cm^2 *pin* coupons on glass/TCO substrates which were cut from their modules in their production line. Solar cells had to be finished at UB by adding the back contact. It has to be taken into account that TS factory is located in Ourense, 1000 km away from Barcelona. The trials done onto TS cells were part of the project tasks and were considered a good opportunity since TS has the capability of fabricating state-of-the-art a-Si:H solar cells. Therefore, onto such good devices, different back reflectors were tried. In addition, this helped us to optimise the BRs since during most of the time spent to develop this thesis, the PECVD equipment used to deposit the silicon layers onto 10 × 10 cm^2 substrates was not available.

The *pin* amorphous silicon layers were deposited by PECVD onto 2.2 × 2.6 m^2 TCO coated glass substrates at TS without performing any laser scribing step. This large *pin* structures were cut into 10 × 10 cm^2 coupons at TS. Once the coupons were received at UB, they were cut again into smaller pieces, and a back reflector stack was deposited on top of the *pin* structure. First, ZnO:Ga or ZnO:Al were sputtered over the whole *pin* structure and then, silver or aluminium was deposited by means of thermal evaporation through a mask which defined 1 cm^2 area solar cells. Afterwards, ZnO was etched by means of 0.5% HCl in order to avoid lateral leaks during solar cell operation. Finally, the device was annealed in air for half an hour at 160 °C.

The long air exposure of the *pin* coupons during transportation from TS to UB resulted in the growth of an interfacial oxide layer on top of the n-layer. Different approaches were followed to identify and eliminate the effect of this thin oxide layer, and the results are presented in the following sections.

7.2.1 Defective layer formation and effect of aqueous cleaning

As soon as the TS *pin* coupons were received, a back reflector was deposited onto the n-layer following the procedure described above. However, independently of the deposition conditions used, the cells showed S-shaped current density voltage (J-V) curves suggesting the existence of a defective layer at the interface of the device. The TS *pin* coupons had been exposed to air during some time (a few days owing to transportation), and it was assumed that the interface could have been oxidised. As it happens with crystalline silicon, when a clean a-Si:H surface was exposed to air a layer of silicon oxide could have built up forming what is called a native oxide layer.

In order to evaluate the effect of time, identical *pin* structures with identical back contacts were prepared at UB with the only difference of the time elapsed between *pin* deposition and TCO layer deposition. As it can be observed in Fig. 7.2, when the air exposure time of the *pin* structure increased, the resulting J-V curve showed an S-shape, i.e. a poor fill factor. The formation of a defective layer at the interface between the n-type and the TCO caused a carrier transport problem as reflected in the solar cell performance. The J-V characteristics depicted in Fig. 7.2 correspond to two cells deposited at UB. Both had a ZnO doped with 4 wt.% Ga_2O_3 and evaporated aluminium as the back contacts. The black curve corresponds to a BR deposited just after the *pin* deposition, whereas the red curve corresponds to a BR deposited on the following day. This curve shows the effect of oxidation occurred at the interface prior to the deposition of the BR as it happened with TS *pin* coupons.

In case of c-Si, the native oxide is easily removed by the dip in a diluted

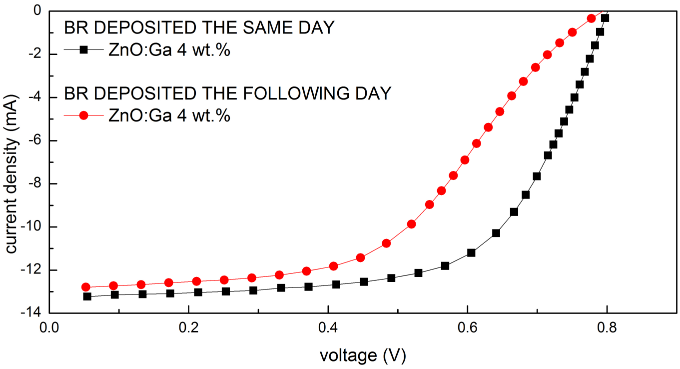

Figure 7.2: J-V curves of two *pin* a-Si:H solar cells deposited at UB in the same run. The black curve corresponds to a back reflector deposited the same day, after the silicon deposition whereas the red one corresponds to a back reflector deposited the following day (more than 12 hours after) using identical deposition conditions.

hydrofluoric acid (HF) solution which produces a silicon surface terminated by hydrogen bonded to silicon dangling bonds [188]. The thickness of the native oxide layer depends on the time of exposure and the conditions under which a clean surface is exposed [189]. Therefore, a chemical etching using dilute HF was performed onto oxidised a-Si:H *pin* coupons previous to the BR deposition. The resulting cells were not reproducible, and on many occasions, short circuited cells, or still S-shaped J-V curves, were found.

In order to determine the chemical state of the *pin* coupon surface before and after the aqueous cleaning, X-ray photoelectron spectroscopy was performed onto three differently treated *pin* coupon surfaces. The first analysis was performed onto an as-received *pin* coupon. The second and third coupons were dipped in a 1 % HF solution for 60 and 120 s and were immediately loaded into the XPS vacuum chamber for a straightaway analysis. The core levels of C, O, Si, and F were characterised, and results are presented below.

After the HF etching, samples showed a slight trace of fluorine. Since the samples were rinsed in deionised water after etching, the fluorine levels were significantly low. The F surface atomic content of the HF etched

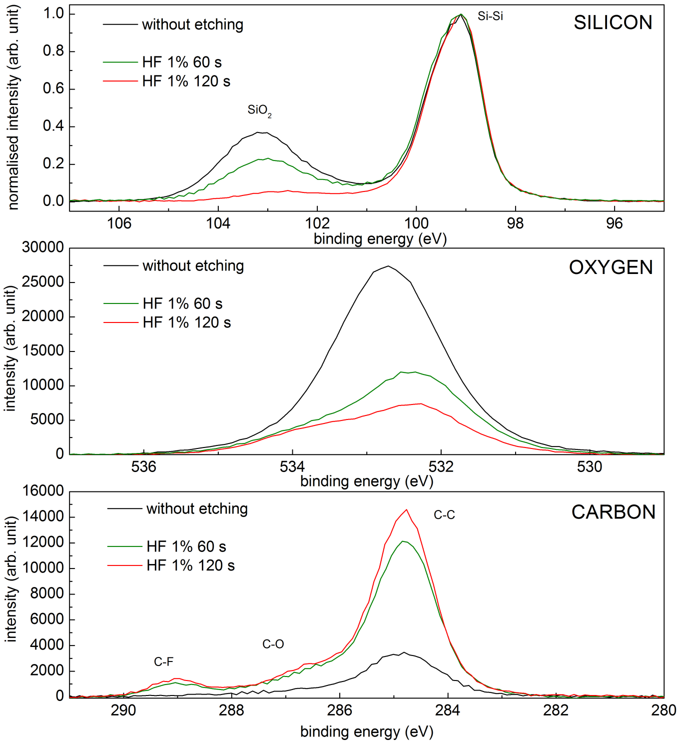

Figure 7.3: Core level photoemission spectra of the *pin* structures measured by XPS. The black curve corresponds to an as-received *pin* coupon and the green and red to chemically etched *pin* coupons in 1% HF for 60 and 120 s respectively. The top graph shows the Si $2p$ peak, the center graph shows the O $1s$ emission features and the bottom graph shows the C $1s$ spectra.

samples was found to be below 0.2%. Instead, the core levels of Si, O, and C presented a different profile depending on the aqueous cleaning step performed.

In Fig. 7.3, the top graph corresponds to the normalised silicon $2p$ peak profile. It presents a maximum at 99.1 eV, which is associated to Si-Si bonds. Moreover, a chemically shifted peak at around 103.1 eV corresponding to oxidised silicon [127] is also measured for as received and dipped 60 s in 1 % HF *pin* coupons. This peak is associated to SiO_2 by many authors [190, 191]. This result proved the existence of a native oxide layer. Dipping the cell into diluted HF reduced the silicon oxide peak intensity. After 120 s of chemical etching, the oxide peak was practically removed. It shows that HF etching could eliminate the native oxide from the *pin* coupon surface.

The central graph in Fig. 7.3 shows the shape and intensity of the O core level. In this case, it is remarkable how the O peak intensity decreased as HF etching was performed for longer duration. It implied a decrease in atomic oxygen concentration on the surface. The maximum of the O 1*s* peak for the as-received sample was located at around 532.7 eV. This peak is associated to SiO_2 [127]. Instead, after the HF treatment the O 1*s* peak consisted of two contributions at around 532.4 and 533.8 eV. Now, the O ls binding energies revealed a different oxygen environment. The low binding energy peak can be related to oxygen bonded to silicon although it is now located at a lower binding energy compared to the as-received sample. This shift is associated to a decrease in the oxide layer thickness [190]. The thinner oxide layer found after HF etching moved the peak towards lower binding energies owing to the more pronounced screening effects from the substrate [192]. The higher energy peak at 533.8 eV could have appeared owing to oxygen singly bounded to carbon [193].

The bottom graph in Fig. 7.3 shows the carbon core level. The peak was recorded in order to correct the spectra displacement that may appear owing to charging effects. Moreover, it gives an idea of the contamination present at the samples surface. The as-received *pin* coupons showed a C atomic surface content of 13%, whereas the etched surfaces had a C content of around 50%. Chemically etching the samples with HF yielded a surface with carbon being the most abundant impurity. This effect was also found by Zazzera *et. al* [190]. The performance of semiconductor devices can be altered by the presence of contamination during device fabrication. Moreover, C can also hinder the etching process by masking the surface from the etchant [194]. In Fig. 7.3 it can be seen how the C peak intensity rose dramatically after HF etching. The highest peak present in all the samples and located at 284.8 eV was associated to hydrocarbons, i.e. C bonded to C or to H. Moreover, the cleaned surfaces showed two peaks corresponding to C-O [190] and C-F bonds [195] at 286.5 and 289 eV respectively. The rising of the C peak with etching showed that regardless of the native oxide removal, the surface was even more contaminated. This contamination led to the formation of a defective layer and evidenced the reason of a non-proper working device.

The deionised water used to prepare or rinse the cells was free of ions but not of neutral species such as organic carbon contaminants. The water could be a source of C contamination. Beyer *et al.* [196] also ascribes the carbon contamination to deionised water. Moreover, carbon could be present at the glass surface of the cells or in the plastic vessels used during the etching process and it might have contributed to rise the concentration of C in the solution.

Chemical etching using dilute hydrofluoric or ammoniacal-hydrofluoric acid as well as plasma etching (RIE) using chlorine or fluoroform were tried, but the results were also not reproducible. Perhaps, a process combining an oxidising step with H_2SO_4:H_2O_2 which grows and densifies the native oxide layer plus a diluted HF process that would remove the complete layer saturating the surface with hydrides [197] would result in a clean surface. It should be noted that not only the native oxide layer and C contamination had to be removed but also the thin n-layer should not be affected to get a working device.

A defect-rich interface was formed owing to the existence of a native layer oxide or owing to the presence of C contamination after the aqueous cleaning. A defective interface could lead to the formation of an electrical barrier due to band bending or even to a band discontinuity [29]. Both effects enhanced the recombination because charge carriers could not pass the barrier and thus carriers recombined in the vicinity of the interface where they were accumulated [29]. This recombination loss was voltage dependent given that the height of the barrier might had been influenced by the applied voltage, which could assist the charge carriers to overcome the barrier. In the J-V curve measured under illumination, such a barrier could lead to a characteristic S-shape. Lower barriers resulted in a mere decrease in FF as a result of an increase in the series resistance and a decrease in the parallel resistance [29].

7.2.2 Transporting samples in inert gas atmosphere

Apart from the different chemical and physical procedures enumerated in the previous section, which led to non-reproducible results, an improved transport method was tried to at least minimise the growth of the native oxide layer and to avoid the absorption of surface contaminants. A solution

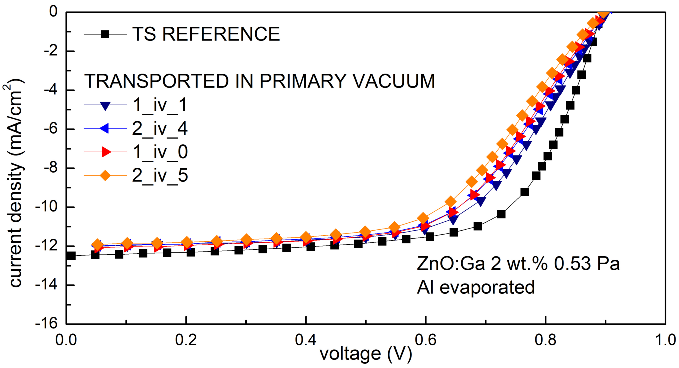

Figure 7.4: J-V characteristics of a set of cells received in primary vacuum. The black curve corresponds to the TS reference, the rest correspond to cells delivered in vacuum with a ZnO:Ga BR deposited at UB.

was to transport the solar cells in vacuum or nitrogen atmosphere. Therefore, a set of samples was quickly delivered in a controlled atmosphere for the BR deposition from TS to UB.

The first approach was to send the coupons in plastic boxes where nitrogen had been introduced and then pumped down leaving the samples sealed in primary vacuum. Samples were received at UB around 16 to 20 hours later, and back reflectors were quickly deposited during the following hours.

In general trends, samples still presented a damaged interface and slightly S-shaped J-V curves were measured (Fig. 7.4). The highest FF values found were between 0.58 and 0.64, whereas a state-of-the-art TS cell presents values as high as 0.72-0.74. Nevertheless, the results were repeatable as it can be observed in Fig. 7.4, where the J-V curves of different cells are shown. All of them present a diminished FF, but in all cases the reduction was similar.

The best result (FF=0.64) of this set of experiments was found for a deposition of 90 nm of 4 wt.% ZnO:Ga at 0.13 Pa. In comparison to previous experiments, the more controlled time and atmosphere made the results repeatable and nearer to standard TS solar cell performance. Nevertheless, it was still not possible to discard the formation of a native oxide layer. Although the samples were transported in primary vacuum, the residual oxygen present in the boxes could have caused the formation of a bad interface.

Another approach was to send the coupons in a nitrogen atmosphere following the same procedure as before, but without pumping the nitrogen away. The cells reached UB after 20 hours of transportation, and the experimental conditions which previously led to the best results were repeated.

A pressure of 0.13 Pa and a Ga_2O_3 doping concentration of 4 wt.% were used for the deposition of ZnO:Ga. Once again, the FF of the obtained cells was lower than the standard FF and the cell series resistances presented considerably higher values than TS standard cells suggesting that it was not possible to define a proper interface when the cell had been exposed to a residual air atmosphere for so long.

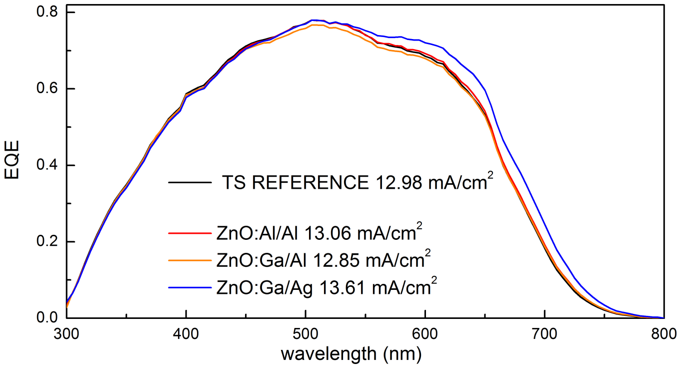

Figure 7.5: External quantum efficiency of a standard solar cell fabricated entirely at TS (black curve) compared to *pin* coupons from TS transported in nitrogen and finished at UB with ZnO:Ga and Aluminium (orange curve) and Silver (blue curve) as well as finished with ZnO:Al and Aluminium (red curve).

The external quantum efficiency of TS *pin* structures transported in nitrogen atmosphere finished with a layer of ZnO:Ga 4 wt.% and a metal layer (aluminium or silver) are compared to TS standard cell in Fig. 7.5. Although the FF of the cells finished with a BR prepared at UB was worse than the FF of cells fabricated at TS, the short circuit current achieved similar values and could be compared by means of the EQE. When ZnO:Ga was used as BR, no improvement could be observed on those cells, but

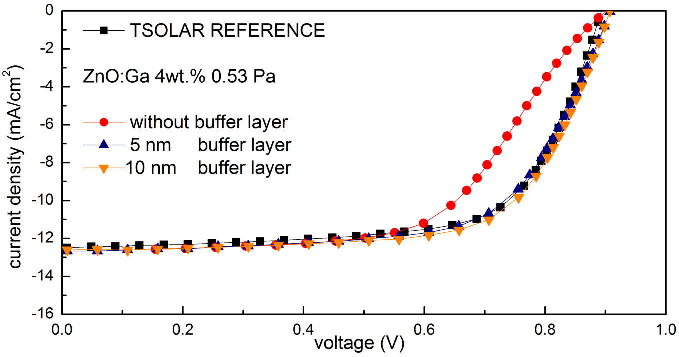

Figure 7.6: Comparison between a reference cell finished at TS (black) and three solar cells finished at UB. The green and orange curves correspond to *pin* coupons covered with 5 and 10 nm, respectively, of ZnO:Al protective layer at TS and finished with a ZnO:Ga 4 wt.% TCO at UB. The red curve has the same BR deposited at UB but it was not protected before being sent and, thus, showed an S-shape curve.

when silver was applied as a metal, instead of aluminium, an increase of 4.85 % in photocurrent was observed. Similar results were found for cells deposited at UB as well as in previously published works [20].

Moreover, in Fig. 7.5 we can compare the EQE of the cells with ZnO:Ga and ZnO:Al layers. On top of both layers, identical aluminium layers were thermally evaporated. ZnO:Al and ZnO:Ga were 90 nm thick and were deposited under identical sputtering conditions, i.e. pressure, power, target to substrate distance, temperature, etc. The results were similar in this case, despite that ZnO:Al showed a slightly better photocurrent. The lower sheet resistance which characterises the ZnO:Ga in comparison to ZnO:Al did not improve the cell performance.

7.2.3 Thin protective layer at the interface

An alternative to overcome the oxidation of the BR interface was to deposit a very thin protective layer of ZnO:Al at TS before sending the samples. Different set of samples with 5 and 10 nm of ZnO:Al were delivered to UB where different ZnO:Ga TCOs were deposited on top of the structure.

In this case, the S-shape of the J-V curve was not observed in any of the samples. Both the 5 and 10 nm protective layer of ZnO:Al deposited at TS were enough to avoid the oxidation of the interface. The device performance, as observed from J-V curves, was comparable to the TS reference (Fig. 7.6).

A set of ZnO:Ga layers with different Ga_2O_3 concentrations (2 and 4 wt.%) and different deposition conditions (pressure from 0.07 to 0.53 Pa, with and without oxygen flow) led to TCO layers with a sheet resistance ranging from 300 to 300000 $\Omega/\Box$ on glass. However, solar cells finished with layers as different as the aforementioned resulted in highly similar external quantum efficiencies. Except the layer deposited at 0.13 Pa and 4 wt.% Ga_2O_3 doping, which showed a slightly different EQE profile (Fig. 7.7), the rest were almost identical. The short circuit current density (J_{sc}) calculated from the spectral response showed a variation within the results below 0.6%. It suggests that once the interface was protected by a thin ZnO:Al layer deposited at TS, the posterior quality of the TCO was not relevant. Moreover, the existence of a seed layer of ZnO:Al makes the ZnO:Ga to grow similarly despite the variations in the deposition conditions. As argued in [198], the structural evolution of a ZnO film is strongly governed by the structure of the nucleation layer. In the experiments performed here, the protective layer deposited at TS acted as a seed layer for the further deposition of the back reflector and compromised the properties of the posterior layer. Given that all the *pin* structures were covered with the same thin ZnO:Al layer, the effect of the different doping amounts and deposition conditions used for these experiments could not be appraised in the resulting devices.

Although these results showed that it was possible to finish the device after transportation and after a long exposure to air, it also showed up that once the interface was created it was not possible to modify the device performance with the ZnO layers used here.

Given that it was not possible to study the influence of the different TCOs by depositing them onto the protective layer, the removal of this protective film by means of HCl was tried. Therefore, cells were entirely dipped into a diluted solution of HCl (0.5%) for a second and the protective layer was entirely removed owing to the easy etchability of ZnO in HCl. The deposition of the TCO layer was immediately carried out, and different deposition conditions were tried every time. In addition to those corresponding to optimised back reflectors, also milder deposition

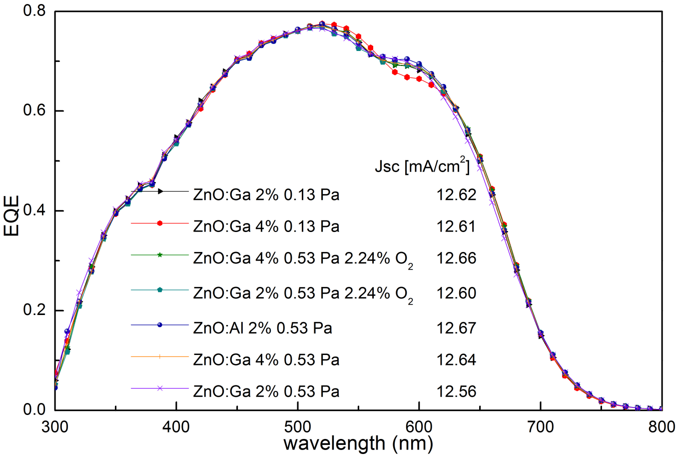

Figure 7.7: EQE of a set of *pin* coupons covered with a 10 nm protective layer and finished at UB with sputtered ZnO:Ga and ZnO:Al (for comparison) and evaporated silver. The values of the J_{sc} were calculated from the EQE. Samples were measured at Forschungszentrum Jülich.

conditions, which ensured a slow deposition at the beginning, were used to discard damage of the interface due to ion bombardment. In Fig. 7.8, several J-V curves corresponding to different deposition conditions of ZnO:Ga layers are shown. In all cases, the cells showed a bad J-V curve, where an S-shape behaviour was seen. The conclusion drawn after this experiment was that after dipping the cells in HCl, it was not possible to form a proper interface anymore. Dipping the cell in HCl removed the ZnO but probably left some C contamination on the surface as it happened after HF etching.

7.3 ZnO:Ga and ZnO:Al back reflectors onto freshly prepared *pin* structures

A set of *pin* amorphous silicon solar cells were fabricated, and different back reflectors were immediately deposited by magnetron sputtering. With this method, oxidation problems were directly avoided and the performance of ZnO:Ga based back reflectors could be assessed. Nevertheless, just a few trials could be performed.

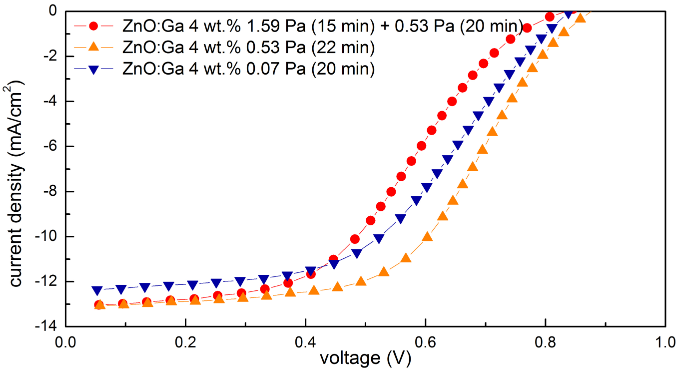

Figure 7.8: J-V curve measurement of the best solar cell of each experiment performed onto protected cells where the thin layer deposited at TS had been removed by HCl and a new ZnO:Ga was deposited at UB

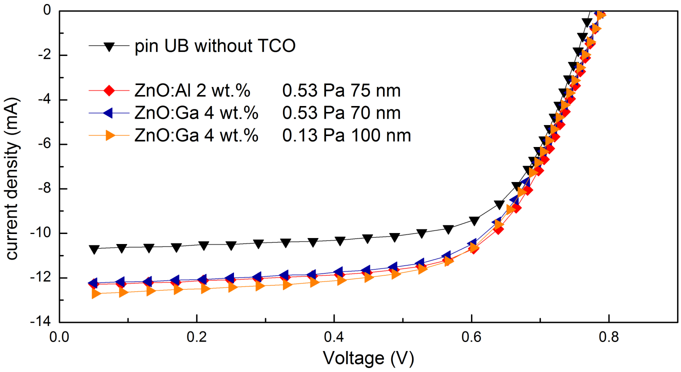

Figure 7.9: J-V curve measurement of solar cells fabricated at UB. The black curve corresponds to a *pin* solar cell finished just with aluminium as BR. The rest were finished with with ZnO:Al (red) and ZnO:Ga (blue and orange) plus aluminium.

As discussed in Chapter 5, the optimal doping level found for ZnO:Ga was of 4 wt.% Ga_2O_3. A pressure range between 0.07 and 0.53 Pa was tried obtaining Rs between 250 and 2000 Ω/□ which were lower than the Rs of the standard ZnO:Al layer used for comparison (30000 Ω/□).

The best J-V curves of some of the obtained cells can be observed in Fig. 7.9. The role of the TCO can be observed when comparing a device without it (black curve) to the one with either a ZnO:Al (red curve) or ZnO:Ga (blue and orange) layer placed between the metal and the *n*-layer. When a TCO was used, the current density of the device was increased around 12%. When comparing ZnO:Ga to ZnO:Al as back reflectors, in general, both behaved similarly as observed in Fig. 7.9. The lower sheet resistance which characterises the ZnO:Ga in comparison to ZnO:Al did not improve the cell performance. In both cases, the Rs was low enough and formed a good interface contact.

The lowest pressure used in the case of 4 wt.% ZnO:Ga made the short circuit current density to slightly overcome the higher pressure trials for both 2 wt.% ZnO:Al and 4 wt.%ZnO:Ga, but with a slightly reduced FF. Perhaps, the use of 0.13 Pa implied that high energetic species reaching the substrate might have slightly damaged the interface leading to a reduction in FF.

Solar cells entirely fabricated at UB showed no S-shape and a FF as high as 0.68 was obtained. This experiment proved the suitability of the back reflectors deposited at UB. However, the general performance of the devices was not yet at an optimal point since they were the first cells fabricated with a recently acquired equipment. The highest efficiency obtained in this first round of *pin* type solar cells fabricated entirely at UB was of 6.9%.

Conclusions

When the as-deposited *pin* structures of a-Si:H solar cells were exposed to ambient for long time, prior to the deposition of a back reflector, a thin layer of silicon oxide was formed on the surface. This oxidised layer was detrimental for the posterior deposition of the back reflector and led to a bad performance of the device.

Cleaning the surface with diluted HF removed the native oxide layer, but a carbon contamination layer was left on the surface, which was inferred from the XPS measurements. This contaminated interface led to the formation of an electrical barrier owing to band bending or a band discontinuity at the interface. The J-V characteristic under illumination showed an S-shape.

Once the effect was detected, proper packing and transportation methods, such as in nitrogen or vacuum boxes were tried. However, the devices still showed a poor performance with FF below 0.64. In this case, results were at least reproducible. The deposition of a thin ZnO:Al protective layer resulted in working devices but, given that the interface was already created and the posterior ZnO:Ga was growing on top of a seed layer, the resulting devices showed identical performance despite the different BR deposition conditions used.

The short circuit density values of the devices were estimated from the external quantum efficiency measurements. In general, ZnO:Al and ZnO:Ga back reflectors showed similar performance compared to the ones fabricated at TS. Only the cells whose metal back reflector was silver, showed an increase of around 5% in photocurrent. No important differences were found between the behaviour of ZnO:Al and ZnO:Ga suggesting that both materials behave similarly as back reflectors although the electrical properties of ZnO:Ga appeared to be remarkably better.

Finally, a set of ZnO:Ga layers were used as back reflectors for the cells fabricated at UB. When a TCO was used, the current density of the device was considerably increased. The use of Ga doped ZnO led to almost similar performance and no marginal advantage was observed with respect to Al doped ZnO.

8 Conclusions

The objective of the present work was to provide a better understanding of magnetron sputtered TCOs based on ZnO in order to apply them to thin film silicon solar cells at the Grup d'Energia Solar from UB. The properties of aluminium doped and gallium doped zinc oxide as well as the properties of the Zn-In-Sn-O multi-compound were studied. Moreover, ZnO based back reflectors were deposited on *pin* amorphous silicon solar cells.

To achieve a better understanding of the relation between the deposition conditions and the layer properties, ZnO:Al films were deposited at different substrate temperatures and discharge powers. Moreover, high-quality ZnO:Al layers were capped and annealed at high temperature to improve their properties. After the experiments, the following was concluded:

- The vertical grain size of the ZnO:Al layers increased for substrate temperatures higher than 300°C reaching the highest value of 50 nm at 420°C.

- The transmittance obtained in the range where thin film silicon solar cells respond (400-1100 nm) was not affected by substrate temperature. The highest integrated transmittance values of 86.2% in the VIS and 88.2% in the NIR range were found for the layer deposited at 420°C.

- A resistivity as low as $4.7\times10^{-4}\ \Omega\,\mathrm{cm}$ and a carrier concentration as high as 3.71×10^{20} cm^{-3} were obtained at 420°C for a 200 nm layer of ZnO:Al.

- A remarkable increase in mobility was found for temperatures above 300°C. The highest mobility was of 37.5 cm^{2}V^{-1}s^{-1} at a substrate temperature of 420°C.

- The higher carrier concentration obtained at higher temperatures pushed the band gap of the layers towards higher values owing to the Burstein-Moss effect. A band gap of 3.75 eV was obtained at 420°C.

- The most remarkable feature found with the increase in deposition power was the increase in deposition rate (from 0.9 to 9 $\mathrm{nm\,min^{-1}}$).

- The resistivity decreased with the increase in deposition power until it reached $1.2 \times 10^{-3}\ \Omega\,\mathrm{cm}$ at 250 W.

- The highest mobility of the ZnO:Al layers obtained varying the deposition power (19.0 $\mathrm{cm^2V^{-1}s^{-1}}$) was lower than the highest mobility obtained for the temperature series (37.5 $\mathrm{cm^2V^{-1}s^{-1}}$).

- Temperatures above 300°C and a power around 250 W led to the best electrical and optical properties.

- The annealing in vacuum or nitrogen at 650°C under different capping layers (a-Si:H and alumina) improved the mobility significantly leaving a similar carrier concentration. Values as high as 68.5 $\mathrm{cm^2V^{-1}s^{-1}}$ and 67 $\mathrm{cm^2V^{-1}s^{-1}}$ for ZnO:Al capped with *n*-type silicon and alumina were achieved respectively.

- It was observed that the minimum thickness of the alumina capping layer needed to achieve a higher mobility after annealing ZnO:Al was 25 nm.

- After annealing under capping layer, the transmittance was higher near the band gap and also in the long wavelength range.

Afterwards, gallium was tried as an alternative dopant to ZnO. A series of 200 nm ZnO:Ga layers deposited at different pressures, extrinsic doping concentrations, temperatures and oxygen concentrations in the sputter chamber were studied and the following was observed:

- In all the cases, 200 nm polycrystalline layers with the *c*-axis oriented perpendicular to the substrate were obtained.

- The lattice parameter c was found to be smaller in case of ZnO:Ga in comparison to ZnO:Al.

- The higher the doping concentration in the target, the higher the lattice compressive stress.

- The crystalline quality was improved (lower FWHM), and the lattice compressive stress was reduced (lower c) with the increase in substrate temperature.

- The highest gallium incorporation (9.2%) was found for a 4 wt.% ZnO:Ga at 75ºC.

- The optical transmittance in the range between 300 and 1100 nm was found to be above 83.7% for the whole set of gallium doped zinc oxide layers deposited during this thesis.

- The use of highly doped layers implied a reduction of the transmittance at wavelengths larger than 800 nm in comparison to using a 2 wt.% Ga_2O_3 doped target.

- Increasing the oxygen volume during deposition improved the transparency of the layers at wavelengths longer than 1100 nm but decreased the carrier concentration by filling of oxygen vacancies and by chemisorption of oxygen at the grain boundaries. Even a small amount of oxygen had an obvious influence on ZnO:Ga films.

- The mobility of the 2 wt.% layers was modified with deposition pressure achieving its highest value of 7.8 $cm^2V^{-1}s^{-1}$ at 0.13 Pa.

- 4 wt.% Ga_2O_3 doping concentration was optimal for the production of highly conductive ZnO:Ga layers with a high band gap energy (3.71 eV). A carrier concentration as high as 9×10^{20} cm^{-3}, with a mobility of 5.3 $cm^2V^{-1}s^{-1}$ was obtained for the layer with a 4 wt.% Ga_2O_3 doping concentration.

- At identical deposition conditions, a higher carrier concentration was measured in ZnO:Ga (above 10^{20} cm^{-3}) in comparison to ZnO:Al (6.2×10^{19} cm^{-3}). Instead, the ZnO:Al layer presented a higher mobility (22 $cm^2V^{-1}s^{-1}$) in comparison to the ZnO:Ga layer (2.5 $cm^2V^{-1}s^{-1}$). The transmittance of both layers was similar.

In order to reduce the indium content in ITO films, ZnO was co-sputtered with ITO and the resulting multi-compound was studied. Zinc indium tin oxide transparent conducting thin films with varying Zn concentration were investigated, and their structural, optical and electrical properties as well as their electronic band structure was discussed. A summary of the results can be found below:

- The ZITO layers resulted to be amorphous containing embedded nanocrystals.
- The resistivity of the as-deposited ZITO samples slightly decreased for a Zn content ratio of 17.1% reaching $6.6\times10^{-4}\ \Omega\,\mathrm{cm}$.
- Whereas the mobility of the layers remained almost constant with the increase in Zn cation content, the carrier concentration decreased with the introduction of Zn owing to the substitution of In^{3+} by Zn^{2+}, which compensated the Sn^{4+} dopants in ITO layers.
- As soon as Zn was introduced in the films, the optical transmittance was improved from 75 to 80% in the visible wavelength range due to the higher oxygen content into the layers.
- By means of X-ray and UV photoemission spectroscopy the electronic band structure was studied. The measurements showed that, with the increase in Zn concentration, the oxygen vacancy concentration of the surface increased resulting in a degenerately n-doped surface layer.
- The work function of the layers with Zn content ratio between 17.1 to 67.3% was found to vary from 4.7 to 4.3 eV.
- The experiments demonstrated that the work function of ZITO surfaces is reduced by about 0.5 eV during UPS measurements due to the photochemical hydroxilation of the surface.

The majority of this work was focussed on the relation between the deposition conditions and the properties of the resulting materials, whereas the final experiments were focussed on the application of ZnO layers to back reflectors of *pin* amorphous silicon solar cells.

- When *pin* structures were long exposed to air, a thin layer of silicon oxide was formed at the *n*-layer/TCO interface causing a bad performance of the device.

- Cleaning the surface of the *pin* structures with diluted HF removed the native oxide layer, but a carbon contamination layer arose on top of the *n*-layer.

- The transportation of the *pin* structures in nitrogen or primary vacuum atmosphere did not prevent the growth of an oxide layer.

- The deposition of a 5 to 10 nm ZnO:Al protective layer on top of the *pin* structure protected the device from oxidation but, given that the interface was already created and that the posterior ZnO was growing on top of a seed layer, the resulting devices showed identical performance despite the different BR deposition conditions used.

- When ZnO:Ga or ZnO:Al layers where used in back reflectors of a-Si:H cells entirely fabricated at UB, an improvement of 13% in cell efficiency was observed with respect to identical cells with only a metal layer as back reflector. Efficiencies up to 6.9% were achieved.

- ZnO:Ga and ZnO:Al were compared as back reflectors in a-Si:H solar cells and the devices showed a similar performance. It showed that the use of gallium as an alternative doping material to aluminium was possible.

Bibliography

[1] R. Vos, *World economic situation and prospects 2012*. United Nations, 2012.

[2] U.S. Census Bureau, "http://www.census.gov/population/international/ International data base," 2013.

[3] R. Pachauri and A. Reisinger, *Climate change 2007: synthesis report*. Intergovernmental Panel on Climate Change, 2007.

[4] A. Jäger-Waldau, *PV status report 2012*. Joint Research Centre, 2012.

[5] S. A. Kalogirou, "Solar thermal collectors and applications," *Progress in Energy and Combustion Science*, vol. 30, no. 3, p. 231, 2004.

[6] J. Zhao, A. Wang, M. A. Green, F. Ferrazza, and V. A. D. Andrea, "19.8% efficient honeycomb textured multicrystalline and 24.4% monocrystalline silicon solar cells," *Applied Physics Letters*, vol. 73, no. 14, p. 1991, 1998.

[7] M. A. Green, K. Emery, Y. Hishikawa, W. Warta, and E. D. Dunlop, "Solar cell efficiency tables (version 41)," *Progress in Photovoltaics: Research and Applications*, vol. 21, p. 1, 2013.

[8] A. Jäger-Waldau, "Thin film photovoltaics: markets and industry," *International Journal of Photoenergy*, vol. 2012, p. 768368, 2012.

[9] M. A. Green, "Recent developments in photovoltaics," *Solar Energy*, vol. 76, no. 1-3, p. 3, 2004.

[10] J. Bailat, V. Terrazzoni-Daudrix, J. Guillet, F. Freitas, X. Niquille, A. Shah, C. Ballif, T. Scharf, R. Morf, A. Hansen, D. Fischer, Y. Ziegler, and A. Closset, "Recent development of solar cells on low-cost plastic substrates," in *Proceedings of the 20th European Photovoltaic Solar Energy Conference*, p. 1529, 2005.

[11] O. Nos, *HWCVD technology development addressed to the high rate deposition of microcrystalline-Si:H*. PhD thesis, Universitat de Barcelona, 2012.

[12] R. Tscharner and A. Shah, "Performance of the roof integrated amorphous silicon plant IMT Neuchatel," *Proceedings of the 17th European Photovoltaic Solar Energy Conference*, vol. 3, p. 2526, 2002.

[13] S. Benagli, D. Borrello, E. Vallat-Sauvain, J. Meier, U. Kroll, J. Hötzel, J. Bailat, J. Steinhauser, M. Marmelo, G. Monteduro, and L. Castens, "High-efficiency amorphous silicon devices on LPCVD-ZnO TCO prepared in industrial KAI TM-M R&D reactor," *Proceedings of the 24th European Photovoltaic Solar Energy Conference*, p. 2293, 2009.

[14] D. S. Ginley, H. Hosono, and D. C. Paine, *Handbook of transparent conductors.* USA: Springer, 2010.

[15] J. Wager, D. Keszler, and R. Presley, *Transparent electronics.* USA: Springer, 2008.

[16] H. Wanka, E. Lotter, and M. Schubert, "Characterization and optimization of the TCO/a-Si:H(B) interface for solar cells by in-situ ellipsometry and SIMS/XPS depth profiling," in *MRS Proceedings*, p. 657, 1994.

[17] E. Johnson, P. Prod'homme, C. Boniface, K. Huet, T. Emeraud, and P. Roca i Cabarrocas, "Excimer laser annealing and chemical texturing of ZnO:Al sputtered at room temperature for photovoltaic applications," *Solar Energy Materials and Solar Cells*, vol. 95, no. 10, p. 2823, 2011.

[18] H. Cao, C. Sun, Z. Pei, A. Wang, L. Wen, R. Hong, and X. Jiang, "Properties of transparent conducting ZnO:Al oxide thin films and their application for molecular organic light-emitting diodes," *Journal of Materials Science: Materials in Electronics*, vol. 5, p. 169, 2004.

[19] S. Fernández, A. Martínez-Steele, J. J. Gandía, and F. B. Naranjo, "Radio frequency sputter deposition of high-quality conductive and transparent ZnO:Al films on polymer substrates for thin film solar cells applications," *Thin Solid Films*, vol. 517, no. 10, p. 3152, 2009.

[20] J. Müller, B. Rech, J. Springer, and M. Vanecek, "TCO and light trapping in silicon thin film solar cells," *Solar Energy*, vol. 77, no. 6, p. 917, 2004.

[21] M. Berginski, J. Hüpkes, A. Gordijn, W. Reetz, T. Wätjen, B. Rech, and M. Wuttig, "Experimental studies and limitations of the light trapping and optical losses in microcrystalline silicon solar cells," *Solar Energy Materials and Solar Cells*, vol. 92, no. 9, p. 1037, 2008.

[22] T. Minami, H. Sato, H. Nanto, and S. Takata, "Group III impurity doped zinc oxide thin films prepared by RF magnetron sputtering," *Japanese Journal of Applied Physics*, vol. 24, no. 10, p. L781, 1985.

[23] V. Assunçao, I. Ferreira, R. Martins, E. Fortunato, A. Marques, and H. Aguas, "Influence of the deposition pressure on the properties of transparent and conductive ZnO:Ga thin-film produced by rf sputtering at room temperature," *Thin Solid Films*, vol. 427, p. 401, 2003.

[24] D. Muñoz, C. Voz, I. Martin, A. Orpella, J. Puigdollers, R. Alcubilla, F. Villar, J. Bertomeu, J. Andreu, J. Damon-Lacoste, and P. Roca i Cabarrocas, "Progress in a-Si:H/c-Si heterojunction emitters obtained by Hot-Wire CVD at 200°C," *Thin Solid Films*, vol. 516, no. 5, p. 761, 2008.

[25] J. Xue, S. Uchida, B. P. Rand, and S. R. Forrest, "4.2% Efficient organic photovoltaic cells with low series resistances," *Applied Physics Letters*, vol. 84, no. 16, p. 3013, 2004.

[26] T. Minami, "Transparent conducting oxide semiconductors for transparent electrodes," *Semiconductor Science and Technology*, vol. 20, no. 4, p. S35, 2005.

[27] P. Thilakan and J. Kumar, "Investigations on the annealing effects on reactively deposited ITO thin films," *Physica Status Solidi A*, vol. 160, p. 97, 1997.

[28] T. Minami, T. Yamamoto, Y. Toda, and T. Miyata, "Transparent conducting zinc-co-doped ITO films prepared by magnetron sputtering," *Thin Solid Films*, vol. 373, no. 1-2, p. 189, 2000.

[29] J. Loeffler, *Transparent conductive oxides for thin-film silicon solar cells.* PhD thesis, Utrecht University, 2005.

[30] H. Ullal, "US PATENT A7668849 Amorphous silicon/polycrystalline thin film solar cells," 1991.

[31] "http://en.wikipedia.org/wiki/Abundance_of_elements_in_Earth's_crust Abundance of elements in Earth's crust," 2012.

[32] S. Major, S. Kumar, M. Bhatnagar, and K. L. Chopra, "Effect of hydrogen plasma treatment on transparent conducting oxides," *Applied Physics Letters*, vol. 49, no. 7, p. 394, 1986.

[33] Y. Igasaki and H. Saito, "Substrate temperature dependence of electrical properties of ZnO:Al epitaxial films on sapphire (1210)," *Journal of Applied Physics*, vol. 69, no. 4, p. 2190, 1991.

[34] A. Suzuki, T. Matsushita, N. Wada, Y. Sakamoto, and M. Okuda, "Transparent conducting Al-doped ZnO thin films prepared by pulsed laser deposition," *Japanese Journal of Applied Physics*, vol. 35, p. L56, 1996.

[35] M. Berginski, J. Hüpkes, W. Reetz, B. Rech, and M. Wuttig, "Recent development on surface-textured ZnO:Al films prepared by sputtering for thin-film solar cell application," *Thin Solid Films*, vol. 516, p. 5836, 2008.

[36] J. Steinhauser, *Low pressure chemical vapor deposited zinc oxide for silicon thin film solar cells. optical and electrical properties.* PhD thesis, Institute of Microtechnology. Univeristé de Neuchâtel, 2008.

[37] K. Ellmer, A. Klein, and B. Rech, *Transparent conductive zinc oxide. Basics and application in thin film solar cells.* Germany: Springer, 2008.

[38] H. McMurdie, M. Morris, E. Evans, B. Paretzkin, W. Wong-Ng, L. Ettlinger, and C. Hubbart, "ZnO reference for bragg peak position and net constants," *Powder Diffraction*, vol. 1, no. 2, p. 76, 1986.

[39] J. I. Owen, *Growth, etching and stability of sputtered ZnO:Al for thin film silicon solar cells.* PhD thesis, Forschungszentrum Jülich, 2011.

[40] S. Takata, T. Minami, and H. Nanto, "The stability of aluminium-doped ZnO transparent electrodes fabricated by sputtering," *Thin Solid Films*, vol. 135, p. 183, 1986.

[41] F. J. Haug, Z. S. Geller, H. Zogg, A. N. Tiwari, and C. Vignali, "Influence of deposition conditions on the thermal stability of ZnO:Al films grown by rf magnetron sputtering," *Journal of Vacuum Science & Technology A: Vacuum, Surfaces, and Films*, vol. 19, no. 1, p. 171, 2001.

[42] T. Tohsophon, J. Hüpkes, S. Calnan, W. Reetz, B. Rech, W. Beyer, and N. Sirikulrat, "Damp heat stability and annealing behavior of aluminum doped zinc oxide films prepared by magnetron sputtering," *Thin Solid Films*, vol. 511-512, p. 673, 2006.

[43] M. Wimmer, F. Ruske, S. Scherf, and B. Rech, "Improving the electrical and optical properties of DC-sputtered ZnO:Al by thermal post deposition treatments," *Thin Solid Films*, vol. 520, no. 12, p. 4203, 2011.

[44] Y. Mi, H. Odaka, and S. Iwata, "Electronic structures and optical properties of ZnO, SnO_2 and In_2O_3," *Japanese Journal of Applied Physics*, vol. 38, no. 6, p. 3453, 1999.

[45] I. A. Rauf, "Low resistivity and high mobility tin-doped indium oxide films," *Materials Letters*, vol. 18, no. 3, p. 123, 1993.

[46] H. E. Swanson, R. K. Fuyat, and G. M. Ugrinic, "Standard X-ray diffraction powder patterns," *National Bureau of Standards Circular*, vol. 539, no. 5, p. 26, 1955.

[47] M. Marezio, "Refinement of the crystal structure of In_2O_3 at two wavelengths," *Acta Crystallographica*, vol. 20, no. 6, p. 723, 1966.

[48] I. Hamberg and C. G. Granqvist, "Evaporated Sn-doped In_2O_3 films: Basic optical properties and applications to energy-efficient windows," *Journal of Applied Physics*, vol. 60, no. 11, p. R123, 1986.

[49] C. Guillen and J. Herrero, "Stability of sputtered ITO thin films to the damp-heat test," *Surface and Coatings Technology*, vol. 201, no. 1-2, p. 309, 2006.

[50] R. Sundaramoorthy, F. J. Pern, C. DeHart, T. Gennett, F. Y. Meng, M. Contreras, and T. Gessert, "Stability of TCO window layers for thin-film CIGS solar cells upon damp heat exposures - Part II," in *Proceedings of the SPIE*, vol. 7412, p. 74120J, 2009.

[51] J. A. Sans, A. Segura, J. Sánchez-Royo, V. Barber, M. Hernández-Fenollosa, and B. Marí, "Correlation between optical and transport properties of Ga-doped ZnO thin films prepared by pulsed laser deposition," *Superlattices and Microstructures*, vol. 39, no. 1-4, p. 282, 2006.

[52] K. Ellmer and R. Wendt, "DC and RF (reactive) magnetron sputtering of ZnO:Al films from metallic and ceramic targets: a comparative study," *Surface and Coatings Technology*, vol. 93, no. 1, p. 21, 1997.

[53] H. Gomez, A. Maldonado, M. L. Olvera, and D. R. Acosta, "Gallium-doped ZnO thin films deposited by chemical spray," *Solar Energy Materials and Solar Cells*, vol. 87, no. 1-4, p. 107, 2005.

[54] D. H. Lee, Y. J. Chang, G. S. Herman, and C. H. Chang, "A general route to printable high-mobility transparent amorphous oxide semiconductors," *Advanced Materials*, vol. 19, no. 6, p. 843, 2007.

[55] K. Ellmer, "Magnetron sputtering of transparent conductive zinc oxide: relation between the sputtering parameters and the electronic properties," *Journal of Physics D: Applied Physics*, vol. 33, p. R17, 2000.

[56] D. M. Mattox, "Particle bombardment effects on thin-film deposition: A review," *Journal of Vacuum Science & Technology A: Vacuum, Surfaces, and Films*, vol. 7, no. 3, p. 1105, 1989.

[57] M. Ohring, *The materials science of thin films.* USA: Academic Press, 1992.

[58] E. Fortunato, A. Gonçalves, V. Assunçao, A. Marques, H. Águas, L. Pereira, I. Ferreira, and R. Martins, "Growth of ZnO:Ga thin films at room temperature on polymeric substrates: thickness dependence," *Thin Solid Films*, vol. 442, p. 121, 2003.

[59] G. Carter, "Preferred orientation in thin film growth, the survival of the fastest model," *Vacuum*, vol. 56, p. 87, 2000.

[60] N. Fujimura, T. Nishihara, S. Goto, J. Xu, and T. Ito, "Control of preferred orientation for ZnO_x films: control of self-texture," *Journal of Crystal Growth*, vol. 130, p. 269, 1993.

[61] K. Jong-Wook, K. Hong-Bae, and K. K. Deok, "Effect of RF power on an Al-doped ZnO thin film deposited by RF magnetron sputtering," *Journal of the Korean Physical Society*, vol. 59, no. 3, p. 2349, 2011.

[62] M. Nisha, S. Anusha, A. Antony, R. Manoj, and M. Jayaraj, "Effect of substrate temperature on the growth of ITO thin films," *Applied Surface Science*, vol. 252, no. 5, p. 1430, 2005.

[63] C. G. Choi, K. No, W.-j. Lee, H.-g. Kim, S. O. Jungb, W. J. Leeb, W. S. Kim, S. J. Kim, and C. Yoon, "Effects of oxygen partial pressure on the microstructure and electrical properties of indium tin oxide film prepared by dc magnetron sputtering," *Thin Solid Films*, vol. 258, p. 274, 1995.

[64] Y. S. Song, J. K. Park, T. W. Kim, and C. W. Chung, "Influence of process parameters on the characteristics of indium zinc oxide thin films deposited by DC magnetron sputtering," *Thin Solid Films*, vol. 467, no. 1-2, p. 117, 2004.

[65] J. Lee, H. Jung, J. Lee, D. Lim, K. Yang, J. Yi, and W. Song, "Growth and characterization of indium tin oxide thin films deposited on PET substrates," *Thin Solid Films*, vol. 516, no. 7, p. 1634, 2008.

[66] L. Meng and M. P. Dos Santos, "Properties of indium tin oxide films prepared by rf reactive magnetron sputtering at different substrate temperature," *Thin Solid Films*, vol. 322, p. 56, 1998.

[67] J. A. Thornton, "High rate thick film growth," *Annual Review of Material Science*, vol. 7, p. 239, 1977.

[68] O. Kluth, G. Schöpe, J. Hüpkes, C. Agashe, J. Müller, and B. Rech, "Modified Thornton model for magnetron sputtered zinc oxide: film structure and etching behaviour," *Thin Solid Films*, vol. 442, no. 1-2, p. 80, 2003.

[69] H. Morkoç and U. Özgür, *Zinc oxide: fundamentals, materials and device technology*. Germany: Wiley-VCH, 2008.

[70] P. Drude, "Zur elektronentheorie der metalle," *Annalen der Physik*, vol. 306, p. 566, 1900.

[71] M. Fox, *Optical properties of solids*. Oxford University Press, 2nd ed., 2010.

[72] M. Wimmer, *Thermische Nachbehandlung von aluminiumdotiertem Zinkoxid und die Silizium/Zinkoxid-Grenzfläche*. PhD thesis, Technischen Universität Berlin, 2011.

[73] J. I. Pankove, *Optical processes in semiconductors*. USA: Dover Publications, 1971.

[74] E. Burstein, "Anomalous optical absorption limit in InSb," *Physical Review Letters*, vol. 93, p. 632, 1954.

[75] T. Moss, "The interpretation of the properties of indium antimonide," *Proceedings of the Physical Society. Section B*, vol. 67, p. 775, 1954.

[76] R. Swanepoel, "Determination of the thickness and optical constants of amorphous silicon," *Journal of Physics E: Scientific Instruments*, vol. 16, no. 12, p. 1214, 1983.

[77] F. Gervais, "Optical conductivity of oxides," *Materials Science and Engineering: R: Reports*, vol. 39, p. 29, 2002.

[78] T. Minami, H. Nanto, and S. Takata, "Highly conductive and transparent aluminum doped zinc oxide thin films prepared by RF magnetron sputtering," *Japanese Journal of Applied Physics*, vol. 23, no. 5, p. L280, 1984.

[79] P. Ágoston, P. Erhart, A. Klein, and K. Albe, "Geometry, electronic structure and thermodynamic stability of intrinsic point defects in indium oxide.," *Journal of Physics. Condensed Matter*, vol. 21, no. 45, p. 455801, 2009.

[80] K. Ellmer, "Resistivity of polycrystalline zinc oxide films: current status and physical limit," *Journal of Physics D: Applied Physics*, vol. 34, no. 21, p. 3097, 2001.

[81] A. Dagamseh, B. Vet, F. Tichelaar, P. Sutta, and M. Zeman, "ZnO:Al films prepared by rf magnetron sputtering applied as back reflectors in thin-film silicon solar cells," *Thin Solid Films*, vol. 516, no. 21, p. 7844, 2008.

[82] X. Yu, J. Ma, F. Ji, Y. Wang, X. Zhang, C. Cheng, and H. Ma, "Preparation and properties of ZnO:Ga films prepared by r.f. magnetron sputtering at low temperature," *Applied Surface Science*, vol. 239, no. 2, p. 222, 2005.

[83] L. Ding, M. Boccard, G. Bugnon, M. Benkhaira, M. Despeisse, F. Sculati-Meillaud, S. Nicolay, P. a. Losio, O. Kluth, P. Carroy, O. Caglar, and C. Ballif, "New generation transparent LPCVD ZnO electrodes for enhanced photocurrent in micromorph solar cells and modules," *IEEE Journal of Photovoltaics*, vol. 2, no. 2, p. 88, 2012.

[84] D. H. Kim, N. G. Cho, H. G. Kim, and W. Y. Choi, "Structural and electrical properties of indium doped ZnO thin films fabricated by RF magnetron sputtering," *Journal of The Electrochemical Society*, vol. 154, no. 11, p. H939, 2007.

[85] M. Bhatti, A. M. Rana, and A. F. Khan, "Characterization of rf-sputtered indium tin oxide thin films," *Materials Chemistry and Physics*, vol. 84, p. 126, 2004.

[86] C. G. Van De Walle, "Hydrogen as a cause of doping in zinc oxide," *Physical Review Letters*, vol. 85, no. 5, p. 1012, 2000.

[87] S. Limpijumnong, P. Reunchan, A. Janotti, and C. Van de Walle, "Hydrogen doping in indium oxide: An ab initio study," *Physical Review B*, vol. 80, no. 19, p. 193202, 2009.

[88] T. Koida, H. Fujiwara, and M. Kondo, "Hydrogen-doped In_2O_3 as high-mobility transparent conductive oxide," *Japanese Journal of Applied Physics*, vol. 46, no. No. 28, p. L685, 2007.

[89] N. F. Mott, "Metal-insulator transitions," *Contemporary Physics*, vol. 14, no. 5, p. 401, 1973.

[90] K. Ellmer and R. Mientus, "Carrier transport in polycrystalline ITO and ZnO:Al II: The influence of grain barriers and boundaries," *Thin Solid Films*, vol. 516, no. 14, p. 5829, 2008.

[91] S. M. Sze, *Physics of semiconductor devices.* USA: Wiley, 1981.

[92] J. Bellingham, W. Phillips, and C. Adkins, "Intrinsic performance limits in transparent conducting oxides," *Journal of Materials Science Lelters*, vol. 11, p. 263, 1992.

[93] T. Minami, "New n-type transparent conducting oxides," *MRS Bulletin*, vol. 25, p. 38, 2000.

[94] K. Ellmer and R. Mientus, "Carrier transport in polycrystalline transparent conductive oxides: A comparative study of zinc oxide and indium oxide," *Thin Solid Films*, vol. 516, no. 14, p. 4620, 2008.

[95] T. Pisarkiewicz, K. Zakrzewska, and E. Leja, "Scattering of charge carriers in transparent and conducting thin oxide films with a non-parabolic conduction band," *Thin Solid Films*, vol. 174, no. 1, p. 217, 1989.

[96] J. Seto, "The electrical properties of polycrystalline silicon films," *Journal of Applied Physics*, vol. 46, no. 12, p. 5247, 1975.

[97] S. Singh, T. Ganguli, R. Kumar, R. Srinivasa, and S. Major, "Substrate temperature dependence of growth mode, microstructure and optical properties of highly oriented zinc oxide films deposited by reactive sputtering," *Thin Solid Films*, vol. 517, no. 2, p. 661, 2008.

[98] T. Tsuji and M. Hirohashi, "Influence of oxygen partial pressure on transparency and conductivity of RF sputtered Al-doped ZnO thin films," *Applied Surface Science*, vol. 157, no. 1-2, p. 47, 2000.

[99] R. Hong, X. Jiang, B. Szyszka, V. Sittinger, S. Xu, W. Werner, and G. Heide, "Comparison of the ZnO:Al films deposited in static and dynamic modes by reactive mid-frequency magnetron sputtering," *Journal of Crystal Growth*, vol. 253, no. 1-4, p. 117, 2003.

[100] E. Fortunato, D. Ginley, H. Hosono, and D. C. Paine, "Transparent conducting oxides for photovoltaics," *MRS Bulletin*, vol. 32, p. 242, 2007.

[101] C. Klingshirn, "ZnO: from basics towards applications," *Physica Status Solidi B*, vol. 244, no. 9, p. 3027, 2007.

[102] A. Walsh, J. Da Silva, S. H. Wei, C. Körber, A. Klein, L. Piper, A. DeMasi, K. Smith, G. Panaccione, P. Torelli, D. Payne, A. Bourlange, and R. Egdell, "Nature of the band gap of In_2O_3 revealed by first-principles calculations and X-ray spectroscopy," *Physical Review Letters*, vol. 100, no. 16, p. 167402, 2008.

[103] H. Hosono, "Ionic amorphous oxide semiconductors: Material design, carrier transport, and device application," *Journal of Non-Crystalline Solids*, vol. 352, no. 9-20, p. 851, 2006.

[104] C. Huang, M. Wang, Z. Deng, Y. Cao, Q. Liu, Z. Huang, Y. Liu, W. Guo, and Q. Huang, "Low content indium-doped zinc oxide films with tunable work function fabricated through magnetron sputtering," *Semiconductor Science and Technology*, vol. 25, no. 4, p. 045008, 2010.

[105] Y. Park, V. Choong, Y. Gao, B. R. Hsieh, and C. W. Tang, "Work function of indium tin oxide transparent conductor measured by photoelectron spectroscopy," *Applied Physics Letters*, vol. 68, no. 19, p. 2699, 1996.

[106] M. A. Green, *Solar Cells: operating principles, technology and system applications.* Australia: Prentice-Hall, Inc., 1982.

[107] J. Steinhauser, S. Fay, N. Oliveira, E. Vallat-Sauvain, and C. Ballif, "Transition between grain boundary and intragrain scattering transport mechanisms in boron-doped zinc oxide thin films," *Applied Physics Letters*, vol. 90, no. 14, p. 142107, 2007.

[108] O. Kluth, B. Rech, L. Houben, S. Wieder, G. Schoepe, C. Beneking, H. Wagner, A. Loeffl, and H. W. Schock, "Texture etched ZnO: Al coated glass substrates for silicon based thin film solar cells," *Thin Solid Films*, vol. 351, pp. 247–253, 1999.

[109] K. Sato, Y. Gotoh, Y. Wakayama, Y. Hayashi, K. Adachi, and H. Nishimura, "Highly textured SnO_2:F TCO films for a-Si solar cells.," *Report of Research Laboratory. Asahi Glass Company Ltd.*, vol. 42, p. 129, 1992.

[110] D. Staebler and C. Wronski, "Reversible conductivity changes in discharg produced amorphous Si," *Applied Physics Letters*, vol. 31, no. 4, p. 292, 1977.

[111] J. Meier, S. Dubail, S. Golay, U. Kroll, and S. Fa, "Microcrystalline silicon and the impact on micromorph tandem solar cells," *Solar Energy Materials and Solar Cells*, vol. 74, p. 457, 2002.

[112] J. S. Colligon, "Energetic condensation: Processes, properties, and products," *Journal of Vacuum Science and Technology A: Vacuum, Surfaces, and Films*, vol. 13, no. 3, p. 1649, 1995.

[113] D. W. Hess, "Plasma material interactions," *Journal of Vacuum Science and Technology A: Vacuum, Surfaces, and Films*, vol. 8, no. 3, p. 1677, 1990.

[114] J. Chapin, "US PATENT 4166018 Sputtering process and apparatus," 1979.

[115] M. Berginski, J. Hüpkes, M. Schulte, G. Schöpe, H. Stiebig, B. Rech, and M. Wuttig, "The effect of front ZnO:Al surface texture and optical transparency on efficient light trapping in silicon thin-film solar cells," *Journal of Applied Physics*, vol. 101, p. 074903, 2007.

[116] R. Cebulla, R. Wendt, and K. Ellmer, "Al-doped zinc oxide films deposited by simultaneous rf and dc excitation of a magnetron plasma: relationships between plasma parameters and structural and electrical film properties," *Journal of Applied Physics*, vol. 83, no. 2, p. 1087, 1998.

[117] R. Schropp and M. Zeman, *Amorphous and microcrystalline silicon solar cells: modelling, materials and device technology.* USA: Kluwer academic, 1998.

[118] T. Repmann, *Stapelsolarzellen aus amorphem und mikrokristallinem Silizium.* PhD thesis, Rheinisch-Westfaehlische Technische Hochschule,, 2003.

[119] S. Sze and G. May, *Fundamentals of semiconductor fabrication.* USA: Wiley, 2003.

[120] C. R. Brundle, C. A. Evans, and S. Wilson, *Encyclopedia of materials characterization: surfaces, interfaces, thin films.* USA: Butterworth-Heinemann, 1992.

[121] R. Delhez, T. H. de Keijser, and E. J. Mittemeijer, "Determination of crystallite size and lattice distortions through X-ray diffraction line profile analysis," *Fresenius Zeitschrift für Analytische Chemie*, vol. 312, p. 1, 1982.

[122] E. J. Mittemeijer and U. Welzel, "The state of the art of the diffraction analysis of crystallite size and lattice strain," *Zeitschrift für Kristallographie*, vol. 223, no. 9, p. 552, 2008.

[123] T. Roisnel and J. Rodríquez-Carvajal, "WinPLOTR: A windows tool for powder diffraction pattern analysis," in *Materials Science Forum, Proceedings of the Seventh European Powder Diffraction Conference (EPDIC 7)*, p. 118, 2000.

[124] E. Fortunato, L. Raniero, L. Silva, A. Gonçalves, A. Pimentel, P. Barquinha, H. Aguas, L. Pereira, G. Goncalves, and I. Ferreira, "Highly stable transparent and conducting gallium-doped zinc oxide thin films for photovoltaic applications," *Solar Energy Materials and Solar Cells*, vol. 92, no. 12, p. 1605, 2008.

[125] Y. C. Lee, S. Y. Hu, W. Water, K. K. Tiong, Z. C. Feng, Y. T. Chen, J. C. Huang, J. W. Lee, C. C. Huang, J. L. Shen, and M. H. Cheng, "Rapid thermal annealing effects on the structural and optical properties of ZnO films deposited on Si substrates," *Journal of Luminescence*, vol. 129, no. 2, p. 148, 2009.

[126] R. F. Egerton, *Physical principles of electron microscopy.* USA: Springer, 2005.

[127] J. F. Moulder, W. F. Stickle, P. E. Sobol, and K. D. Bomben, *Handbook of X-ray photoelectron spectroscopy.* Minnesota: Physical Electronics, Inc., 1992.

[128] L. Van der Pauw, "A method of measuring the resistivity and hall coefficient on lamellae of arbitrary shape," *Philips Technical Review*, vol. 26, p. 220, 1958.

[129] R. Schlaf, *Tutorial on work function.* University of South Florida, 2012.

[130] M. Beerbom, B. Lagel, A. Cascio, B. Doran, and R. Schlaf, "Direct comparison of photoemission spectroscopy and in situ Kelvin probe work function measurements on indium tin oxide films," *Journal of Electron Spectroscopy and Related Phenomena*, vol. 152, p. 12, 2006.

[131] R. Schlaf, H. Murata, and Z. H. Kafafi, "Work function measurements on indium tin oxide films," *Journal of Electron Spectroscopy and Related Phenomena*, vol. 120, no. 1-3, p. 149, 2001.

[132] Y. Yi, J. E. Lyon, M. M. Beerbom, and R. Schlaf, "Characterization of indium tin oxide surfaces and interfaces using low intensity x-ray photoemission spectroscopy," *Journal of Applied Physics*, vol. 100, no. 9, p. 093719, 2006.

[133] S. Gutmann, M. A. Wolak, M. Conrad, M. M. Beerbom, and R. Schlaf, "Effect of ultraviolet and X-ray radiation on the work function of TiO_2 surfaces," *Journal of Applied Physics*, vol. 107, no. 10, p. 103705, 2010.

[134] J. Kohlscheen, Y. N. Emirov, M. M. Beerbom, J. T. Wolan, S. E. Saddow, G. Chung, M. F. MacMillan, and R. Schlaf, "Band line-up determination at p- and n-type Al/4H-SiC Schottky interfaces using photoemission spectroscopy," *Journal of Applied Physics*, vol. 94, no. 6, p. 3931, 2003.

[135] R. S. Reddy, A. S. Reddy, B. Radhakrishna, and S. Uthanna, "Sputter power and sputter pressure influenced structural and optical behaviour of RF sputtered nanocrystalline ZnO films," *Crystal Research and Technology*, vol. 47, no. 10, p. 1095, 2012.

[136] O. Kluth, G. Scho, B. Rech, R. Menner, M. Oertel, K. Orgassa, and H. W. Schock, "Comparative material study on RF and DC magnetron sputtered ZnO: Al films," *Thin Solid Films*, vol. 502, p. 311, 2006.

[137] E. Fortunato, A. Gonçalves, A. Pimentel, P. Barquinha, G. Gonçalves, L. Pereira, I. Ferreira, and R. Martins, "Zinc oxide, a multifunctional material: from material to device applications," *Applied Physics A*, vol. 96, no. 1, p. 197, 2009.

[138] A. Banerjee, C. Ghosh, K. Chattopadhyay, H. Minoura, A. K. Sarkar, A. Akiba, A. Kamiya, and T. Endo, "Low-temperature deposition of ZnO thin films on PET and glass substrates by DC-sputtering technique," *Thin Solid Films*, vol. 496, no. 1, p. 112, 2006.

[139] K. Wasa, M. Kitabatake, and H. Adachi, *Thin film materials technology: sputtering of compound materials.* Japan: Springer, 2004.

[140] S. Singh, R. Srinivasa, and S. Major, "Effect of substrate temperature on the structure and optical properties of ZnO thin films deposited by reactive rf magnetron sputtering," *Thin Solid Films*, vol. 515, no. 24, p. 8718, 2007.

[141] X. Yu, J. Ma, F. Ji, Y. Wang, C. Cheng, and H. Ma, "Thickness dependence of properties of ZnO:Ga films deposited by rf magnetron sputtering," *Applied Surface Science*, vol. 245, no. 1-4, p. 310, 2005.

[142] M. Ohring, "Plasma and ion beam processing of thin films," in *Materials Science of Thin Films*, ch. 5, p. 73, Academic Press, 2001.

[143] A. Antony, P. Carreras, T. Keitzl, R. Roldán, O. Nos, P. Frigeri, J. M. Asensi, and J. Bertomeu, "Influence of RF power on the properties of sputtered ZnO:Al thin films," *Physica Status Solidi A*, vol. 207, no. 7, p. 1577, 2010.

[144] K. Y. Lee, C. Becker, M. Muske, F. Ruske, S. Gall, B. Rech, M. Berginski, and J. Hüpkes, "Temperature stability of ZnO:Al film properties for poly-Si thin-film devices," *Applied Physics Letters*, vol. 91, no. 24, p. 241911, 2007.

[145] F. Ruske, M. Roczen, K. Lee, M. Wimmer, S. Gall, J. Hüpkes, D. Hrunski, and B. Rech, "Improved electrical transport in Al-doped zinc oxide by thermal treatment," *Journal of Applied Physics*, vol. 107, no. 1, p. 013708, 2010.

[146] M. Warzecha, J. I. Owen, M. Wimmer, F. Ruske, J. Hotovy, and J. Hüpkes, "High mobility annealing of transparent conductive oxides," *IOP Conference Series: Materials Science and Engineering*, vol. 34, p. 012004, 2012.

[147] T. Minami, H. Nanto, S. Shooji, and S. Takata, "The stability of zinc oxide transparent electrodes fabricated by RF magnetron sputtering," *Thin Solid Films*, vol. 111, p. 167, 1984.

[148] T. Minami, T. Miyata, and T. Yamamoto, "Stability of transparent conducting oxide films for use at high temperatures," *Journal of Vacuum Science and Technology A*, vol. 17, no. 4, p. 1822, 1999.

[149] R. Buitrago, G. Risso, M. Cutrera, M. Battioni, L. Debernardez, J. Schmidt, R. Arce, and R. Koropecki, "Polycrystalline silicon thin film solar cells prepared by PECVD-SPC," *International Journal of Hydrogen Energy*, vol. 33, no. 13, p. 3522, 2008.

[150] W. Beyer, "Diffusion and evolution of hydrogen in hydrogenated amorphous and microcrystalline silicon," *Solar Energy Materials and Solar Cells*, vol. 78, no. 1-4, p. 235, 2003.

[151] H. R. Shanks, "Formation of pin holes in hydrogenated amorphous silicon at high temperatures and the yield strength of a-Si:H.," *Journal of Applied Physics*, vol. 52, no. 2, p. 811, 1981.

[152] M. V. Ponomarev, K. Sharma, M. A. Verheijen, M. C. M. van de Sanden, and M. Creatore, "Improved conductivity of aluminum-doped ZnO: The effect of hydrogen diffusion from a hydrogenated amorphous silicon capping layer," *Journal of Applied Physics*, vol. 111, no. 6, p. 063715, 2012.

[153] N. H. Nickel, "Hydrogen migration in single crystal and polycrystalline zinc oxide," *Physical Review B*, vol. 73, no. 19, p. 195204, 2006.

[154] G. Dingemans and W. M. M. Kessels, "Status and prospects of Al_2O_3-based surface passivation schemes for silicon solar cells," *Journal of Vacuum Science & Technology A: Vacuum, Surfaces, and Films*, vol. 30, no. 4, p. 040802, 2012.

[155] U. Kroll, J. Meier, A. Shah, S. Mikhailov, and J. Weber, "Hydrogen in amorphous and microcrystalline silicon films prepared by hydrogen dilution," *Journal of Applied Physics*, vol. 80, no. 9, p. 4971, 1996.

[156] S. W. Shin, K. U. Sim, J.-H. Moon, and J. H. Kim, "The effect of processing parameters on the properties of Ga-doped ZnO thin films by RF magnetron sputtering," *Current Applied Physics*, vol. 10, no. 2, p. S274, 2010.

[157] H. E. Swanson, R. K. Fuyat, and G. M. Ugrinic, "Standard X-ray diffraction powder patterns," *National Bureau of Standards Circular*, vol. 539, no. 4, p. 25, 1955.

[158] R. Wang and A. W. Sleight, "High conductivity in gallium-doped zinc oxide powders," *Chemical Materials*, no. 8, p. 433, 1996.

[159] S. Kim, J. Seo, H. W. Jang, J. Bang, W. Lee, T. Lee, and J.-M. Myoung, "Effects of H_2 ambient annealing in fully 002-textured ZnO:Ga thin films grown on glass substrates using RF magnetron co-sputter deposition," *Applied Surface Science*, vol. 255, no. 8, p. 4616, 2009.

[160] M. N. Islam, T. Ghosh, K. Chopra, and H. Acharya, "XPS and X-ray diffraction studies of aluminum doped zinc oxide transparent conducting films," *Thin Solid Films*, vol. 280, no. 1-2, p. 20, 1996.

[161] M. Chen, X. Wang, Y. H. Yu, Z. L. Pei, X. D. Bai, C. Sun, R. F. Huang, and L. S. Wen, "X-ray photoelectron spectroscopy and auger electron spectroscopy studies of Al-doped ZnO films," *Applied Surface Science*, vol. 158, no. 1-2, p. 134, 2000.

[162] M. Chen, Z. L. Pei, C. Sun, L. S. Wen, and X. Wang, "Surface characterization of transparent conductive oxide Al-doped ZnO films," *Journal of Crystal Growth*, vol. 220, p. 254, 2000.

[163] H. Zhu, J. Hüpkes, E. Bunte, and S. Huang, "Oxygen influence on sputtered high rate ZnO:Al films from dual rotatable ceramic targets," *Applied Surface Science*, vol. 256, no. 14, p. 4601, 2010.

[164] K. Tominaga, K. Kuroda, and O. Tada, "Radiation effect due to energetic oxygen atoms on conductive Al-doped ZnO films," *Japanese Journal of Applied Physics*, vol. 27, no. 7, p. 1176, 1988.

[165] P. Carreras, A. Antony, R. Roldan, O. Nos, P. A. Frigeri, J. M. Asensi, and J. Bertomeu, "Transparent conducting thin films by co-sputtering of ZnO-ITO targets," *Physica Status Solidi C*, vol. 7, no. 3-4, p. 953, 2010.

[166] P. Carreras, S. Gutmann, A. Antony, J. Bertomeu, and R. Schlaf, "The electronic structure of co-sputtered zinc indium tin oxide thin films," *Journal of Applied Physics*, vol. 110, no. 7, p. 073711, 2011.

[167] P. Carreras, A. Antony, F. Rojas, and J. Bertomeu, "Electrical and optical properties of Zn-In-Sn-O transparent conducting thin films," *Thin Solid Films*, vol. 520, no. 4, p. 1223, 2011.

[168] W. F. Wu and B. S. Chiou, "Effect of oxygen concentration in the sputtering ambient on the microstructure, electrical and optical properties of radio-frequency magnetron-sputtered indium tin oxide films," *Semiconductor Science and Technology*, vol. 11, no. 2, p. 196, 1996.

[169] G. S. Heo, Y. Matsumoto, I. G. Gim, J. W. Park, K. Y. Kim, and T. W. Kim, "Fabrication of cosputtered Zn-In-Sn-O films and their applications to organic light-emitting diodes," *Solid State Communications*, vol. 149, no. 41-42, p. 1731, 2009.

[170] K. Saji and M. Jayaraj, "Optical and electrical properties of co sputtered amorphous transparent conducting zinc indium tin oxide thin films," *Thin Solid Films*, vol. 516, no. 18, p. 6002, 2008.

[171] D. Williams and C. Carter, *Transmission electron microscopy. A textbook for materials science.* USA: Springer, 1996.

[172] T. W. Kim, J. W. Shin, J. Y. Lee, J. H. Jung, J. W. Lee, W. K. Choi, and S. Jin, "Electron-beam-induced formation of Zn nanocrystal islands in a SiO_2 layer," *Applied Physics Letters*, vol. 90, no. 5, p. 051915, 2007.

[173] H. Hosono, N. Kikuchi, N. Ueda, and H. Kawazoe, "Working hypothesis to explore novel wide band gap electrically conducting amorphous oxides and examples," *Journal of Non Crystalline Solids*, vol. 198-200, p. 165, 1996.

[174] M. Orita, H. Ohta, and M. Hirano, "Amorphous transparent conductive oxide $InGaO_3(ZnO)_m$ ($m<4$): a Zn 4s conductor," *Philosophical Magazine Part B*, vol. 81, no. 5, p. 501, 2001.

[175] D. S. Liu, C. C. Wu, and C. T. Lee, "A transparent and conductive film prepared by RF magnetron cosputtering system at room temperature," *Japanese Journal of Applied Physics*, vol. 44, no. 7A, p. 5119, 2005.

[176] T. Sasabayashi, N. Ito, E. Nishimura, M. Kon, P. Song, K. Utsumi, A. Kaijo, and Y. Shigesato, "Comparative study on structure and internal stress in tin-doped indium oxide and indium-zinc oxide films deposited by r.f. magnetron sputtering," *Thin Solid Films*, vol. 445, no. 2, p. 219, 2003.

[177] S. Narushima, M. Orita, M. Hirano, and H. Hosono, "Electronic structure and transport properties in the transparent amorphous oxide semiconductor 2 $CdO \cdot GeO_2$," *Physical Review B*, vol. 66, no. 3, p. 035203, 2002.

[178] P. Erhart, A. Klein, R. Egdell, and K. Albe, "Band structure of indium oxide: Indirect versus direct band gap," *Physical Review B*, vol. 75, no. 15, p. 153205, 2007.

[179] Z. Dridi, B. Bouhafs, P. Ruterana, and B. Mar, "First-principles investigation of lattice constants and bowing parameters in wurtzite $Al_xGa_{1-x}N$, $In_xGa_{1-x}N$ and $In_xAl_{1-x}N$ alloys," *Semiconductor Science and Technology*, vol. 18, p. 850, 2003.

[180] J. Kim, B. Lagel, E. Moons, N. Johansson, I. Baikie, W. Salaneck, R. Friend, and F. Cacialli, "Kelvin probe and ultraviolet photoemission measurements of indium tin oxide work function: a comparison," *Synthetic Metals*, vol. 111-112, no. 1-2, p. 311, 2000.

[181] S. H. Chen, "Work-function changes of treated indium-tin-oxide films for organic light-emitting diodes investigated using scanning surface-potential microscopy," *Journal of Applied Physics*, vol. 97, no. 7, p. 073713, 2005.

[182] K. B. Sundaram, "Work function determination of zinc oxide films," *Journal of Vacuum Science and Technology A: Vacuum, Surfaces, and Films*, vol. 15, no. 2, p. 428, 1997.

[183] A. Klein, C. Koerber, A. Wachau, F. Saeuberlich, Y. Gassenbauer, R. Schafranek, S. Harvey, and T. Mason, "Surface potentials of magnetron sputtered transparent conducting oxides," *Thin Solid Films*, vol. 518, no. 4, p. 1197, 2009.

[184] F. J. Haug, T. Soderstrom, O. Cubero, V. Terrazzoni-Daudrix, and C. Ballif, "Influence of the ZnO buffer on the guided mode structure in Si/ZnO/Ag multilayers," *Journal of Applied Physics*, vol. 106, no. 4, p. 044502, 2009.

[185] F. J. Haug, T. Soderstrom, O. Cubero, V. Terrazzoni-Daudrix, and C. Ballif, "Plasmonic absorption in textured silver back reflectors of thin film solar cells," *Journal of Applied Physics*, vol. 104, no. 6, p. 064509, 2008.

[186] E. Moulin, U. W. Paetzold, H. Siekmann, J. Worbs, A. Bauer, and R. Carius, "Study of thin-film silicon solar cell back reflectors and potential of detached reflectors," *Energy Procedia. Proceedings of the EMRS Conference.*, vol. 10, p. 106, 2011.

[187] E. Moulin, U. Paetzold, K. Bittkau, M. Ermes, L. Ding, L. Fanni, S. Nicolay, J. Kirchhoff, D. Weigand, A. Bauer, A. Lambertz, C. Ballif, and R. Carius, "Thin-film silicon solar cells applying optically decoupled back reflectors," *Materials Science and Engineering: B. http://dx.doi.org/10.1016/j.mseb.2012.10.016.*

[188] D. B. Fenner, D. K. Biegelsen, and R. D. Bringans, "Silicon surface passivation by hydrogen termination: A comparative study of preparation methods," *Journal of Applied Physics*, vol. 66, no. 1, p. 419, 1989.

[189] A. H. Al-Bayati, K. G. Orrman-Rossiter, J. A. Van den Berg, and D. Armour, "Composition and structure of the native Si oxide by high depth resolution medium energy ion scattering," *Surface Science Letters*, vol. 241, p. 91, 1991.

[190] L. A. Zazzera and J. Moulder, "XPS and SIMS study of anhydrous HF and UV/Ozone-modified silicon (100) surfaces," *Journal of The Electrochemical Society*, vol. 136, no. 2, p. 484, 1989.

[191] F. J. Himpsel, F. R. McFeely, A. Taleb-Ibrahimi, and J. A. Yaramoff, "Microscopic structure of the SiO_2/Si interface," *Physical Review B*, vol. 38, no. 9, p. 6084, 1988.

[192] G. Hollinger, J. Morar, F. Himpsel, G. Hughes, and J. Jordan, "Si(111) surface oxidation: O 1s core-level study using synchrotron radiation," *Surface Science*, vol. 168, no. 1-3, p. 609, 1986.

[193] E. Pamula and P. G. Rouxhet, "Bulk and surface chemical functionalities of type III PAN-based carbon fibres," *Carbon*, vol. 41, p. 1905, 2003.

[194] C. Anandan and R. H. Williams, "Investigation of HF etched hydrogenated amorphous silicon surfaces by X-ray photoelectron spectroscopy," *Semiconductor Science and Technology*, vol. 5, p. 265, 1990.

[195] T. L. Cheeks, "The effect of fluorine atoms on silicon and fluorocarbon etching in reactive ion beam etching," *Journal of Vacuum Science & Technology A: Vacuum, Surfaces, and Films*, vol. 5, no. 4, p. 1917, 1987.

[196] K. Beyer and R. Kastl, "US PATENT 4264374 Cleaning process for p-type silicon surface," 1981.

[197] M. Burrows, R. Opila, K. Demirkan, and M. Lu, "Evaluation of HF treated amorphous silicon for photoemission determined electronic levels," *Proceedings of the 22nd European Photovoltaic Solar Energy Conference*, p. 1290, 2007.

[198] D. Köhl, M. Luysberg, and M. Wuttig, “Structural improvement of zinc oxide films produced by ion beam assisted reactive sputtering,” *Journal of Physics D: Applied Physics*, vol. 43, no. 20, p. 205301, 2010.

List of Figures

List of Tables

List of symbols, acronyms and abbreviations

List of symbols

Latin alphabet

A	Absorptance
a	Lattice parameter
B	Magnetic field
a_0	Effective Bohr radius
$a-Si:H$	Hydrogenated amorphous silicon
c	Lattice parameter; speed of light
$^{\mathrm{o}}C$	Degrees Celsius
d	Layer thickness
d_{hkl}	Distance between (hkl) lattice planes
D	Grain size
e	Microstrain
E_b	Potential barrier at the grain boundary
E_g	Band gap energy
h	Planck's constant

I	Electric current
$i - type$	intrinsic (not doped)
J	Current density
J_0	Saturation current density
J_{mp}	Maximum power current density
J_{sc}	Short circuit current density
k_B	Boltzmann constant
m^*	Effective mass
m_e	Electrons mass
n	Carrier concentration; refractive index
n_i	Ideality factor
n_x	Diffraction order
$n - type$	Negatively doped
p	Pressure
$p - type$	Positively doped
q_e	Fundamental electrical charge
R	Reflectance
r_d	Deposition rate
R_p	Parallel resistance
R_s	Sheet resistance

R_{sr}	Series resistance
T	Transmittance; temperature
T_m	Materials melting point temperature
V	Voltage
V_{mp}	Maximum power voltage
V_{oc}	Open circuit voltage
W	Watt

Greek alphabet

α	Absorption coefficient
β	Breadth
β_G	Gaussian breadth
β_L	Lorentzian breadth
ΔE_{BM}	Burstein-Moss band gap broadening
ε_0	Vacuum permittivity
ε_r	Relative permittivity
ε_∞	High frequency permittivity
η	Energy conversion efficiency
θ	Angle
λ	Wavelenght
μ	Mobility

μ_{gb}	Grain boundary limited mobility
μ_{ii}	Ionised impurity scattering limited mobility
$\mu c - Si : H$	Hydrogenated Microcrystalline Silicon
ν	Frequency
ρ	Resistivity
σ	Conductivity
ϕ	photon flux
Φ	Work function
τ	Lifetime
ω	Angular frequency
ω_p	Plasma frequency

List of acronyms

$AM1.5$	Solar spectrum at an air mass of 1.5
ALD	Atomic Layer Deposition
BE	Binding Energy
BR	Back Reflector
CBM	Conduction Band Minima
dc	Direct Current
EQE	External Quantum Efficiency
FF	Fill Factor

$FWHM$	Full Width at Half Maximum
FTO	Fluorine doped Tin oxide
FZJ	Forschungszentrum Jülich
GES	Grup d'Energia Solar
$HRTEM$	High Resolution Transmission Electron Microscopy
$HWCVD$	Hot Wire Chemical Vapour Deposition
ITO	Indium Tin Oxide (In_2O_3:SnO_2)
IZO	Indium Zinc Oxide (In_2O_3:ZnO)
$J-V$	Current-voltage characteristics
KE	Kinetic Energy
$LIXPS$	Low Intensity X-ray Photoelectron spectroscopy
$LPCVD$	Low Pressure Chemical Vapour Deposition
NIR	Near InfraRed
$PECVD$	Plasma-Enhanced Chemical Vapour Deposition
RIE	Reactive Ion Etching
rf	Radio Frequency
SR	Spectral Response
TCO	Transparent Conducting Oxide
TEM	Transmission Electron Microscopy
TS	T-Solar Global S.A.

UB	Universitat de Barcelona
USF	University of South Florida
UPS	Ultraviolet Photon Spectroscopy
UV	UltraViolet
VBM	Valence Band Maximum
VIS	Visible
WF	Work function
XPS	X-ray Photoelectron Spectroscopy
XRD	X-ray Diffraction
ZITO	Zinc Indium Tin Oxide (ZnO:In_2O_3:SnO_2)

List of abbreviations

at.	Atomic
et al.	From latin, *et alii* (and others)
Eq	Equation
Fig	Figure
i.e.	From latin, *id est* (that is)
min	Minutes
Sec	Section
vol.	Volume
wt.	Weight

Personal Data

Name: **Paz Carreras Seguí**
Date of Birth: January 24, 1985 (Maó, Menorca)
Nationality: Spain
e-mail: pazcarreras@gmail.com

Academic Background

2003-2008	**BSC Physics** (Universitat de Barcelona). Course 2006-2007. Exchange student in Physics at Technische Universität München (TUM) Munich, Germany. Grant: Socrates/Erasmus.
2007-2008	**Master's Degree in Renewable Energies** (Universitat de Barcelona i Universitat Politècnica de Catalunya): Master project on photovoltaic: *Optimització del procés de textura de silici cristal·li amb KOH per la millora del confinament òptic en cèl·lules solars.*
2008-2013	**Physics Ph.D.** (Solar Energy Group, Universitat de Barcelona): *Doped and multi-compound ZnO-based transparent conducting oxides for silicon thin film solar cells.* Directed by Joan Bertomeu and Aldrin Antony. Fellowship: FI2009, Generalitat de Catalunya Internship at the University of South Florida (Tampa, Florida, USA) *Work function measurements of transparent conductive oxides by photoelectron spectroscopy.* Supervised by Rudy Schlaf. Fellowship: BE2010, Generalitat de Catalunya Internship at Forschungszentrum Jülich (Jülich, Germany) *High mobility annealing of ZnO:Al and back reflector etching.* Supervised by Jürgen Hüpkes. Fellowship: BE2011, Generalitat de Catalunya

Professional Background

2009-2011	**Assistant Professor** (UB): Basics on Electromagnetism and Optics, Laboratory of Electromagnetism and Laboratory of Electromagnetism and Optics.

Experimental Skills

- Vacuum Technology: Working experience with Ultra-High Vacuum thin film deposition equipment in Clean Room environment (sputtering, thermal evaporation)
- Optical and Structural Characterisation: UV/VIS/NIR Spectrophotometer, SEM, TEM, XRD, AFM, XPS, UPS, LIXPS, and PDS.
- Electrical Characterisation: Hall effect measurements, Four point probe, solar cells characterisation.

Language Skills

- Catalan: Native language.
- Spanish: Native language.
- English: Fluent.
- German: Fluent.

Scientific publications

1 J. Puigdollers, A. Marsal, S. Galindo, P. Carreras, C. Voz, J. Bertomeu, and R. Alcubilla, "Determination of the density of states on N-type Ptcdi-c13 organic thin-film semiconductor", *Proceedings of the Materials Research Society, Symposium J*, vol. 1435, 2012 http://dx.doi.org/10.1557/opl.2012.169

2 M. Vetter, J. Andreu, J. P. Borrajo, M. Fonrodona, P. Otero, J. A. Rodríguez, O. Agustsson, J. Schotsaert, K. Bittkau, R. Carius, A. Gordijn, J. Hüpkes, G. Jost, O. MintMoustapha, J. P. Rath, R. E. I. Schropp, A. Antony, J. Bertomeu, P. Carreras and F. Kail, "Optimization of the solar cell structure for the industrial implementation in very large area a-Si:H PV modules" *Proceedings of the 27th European Photovoltaic Solar Energy Conference*, p. 2594, 2012.

3 P. Carreras, S. Gutmann, A. Antony, J. Bertomeu, and R. Schlaf, "The electronic structure of co-sputtered zinc indium tin oxide thin films" *Journal of Applied Physics* vol. 110, no. 7, p. 073711, 2011.

4 P. Carreras, A. Antony, F. Rojas, and J. Bertomeu, "Electrical and optical properties of Zn-In-Sn-O transparent conducting thin films" *Thin Solid Films*, vol. 520, no. 4, p. 1223, 2011.

5 O. Jambois, P. Carreras, A. Antony, J. Bertomeu, and C. Martínez-Boubeta, "Resistance switching in transparent magnetic MgO films", *Solid State Communications* vol. 151, no. 24, p. 1856, 2011.

6 A. Antony, P. Carreras, T. Keitzl, R. Roldán, O. Nos, P. A. Frigeri, J. M. Asensi and J. Bertomeu, "Influence of RF power on the properties of sputtered ZnO:Al thin films", *Physica Status Solidi A*, vol. 207, no. 7, p. 1577, 2010.

7 P.A. Frigeri, O. Nos, J.D. Calvo, P. Carreras, R. Roldan, A. Antony, J.M. Asensi and J. Bertomeu, "Uniformity study of amorphous and microcrystalline silicon thin films deposited on 10 cm x 10 cm glass substrate using hot wire CVD technique", *Physica Status Solidi C*, vol. 7, no. 3-4, p. 588, 2010.

8 P. Carreras, A. Antony, R. Roldán, O. Nos, P. A. Frigeri, J. M. Asensi, and J. Bertomeu, "Transparent conducting thin films by co-sputtering of ZnO-ITO targets", *Physica Status Solidi C*, vol. 7, no. 3-4, p. 953, 2010.

9 D. Muñoz, P. Carreras, J. Escarré, D. Ibarz, S. Martín de Nicolás, C. Voz, J. M. Asensi, and J. Bertomeu, "Optimization of KOH etching process to obtain textured substrates suitable for heterojunction solar cells fabricated by HWCVD," *Thin Solid Films*, vol. 517, no. 12, p. 3578, 2009.

Patents

1 J. Escarré, J. Bertomeu, A. Antony, J. Andreu, P. Carreras
Thin film solar cells with combined textures,
(2008) ES Patent No. 63367. Universitat de Barcelona.

Presentations at conferences

1 24th International Conference on Amorphous and Nanocrystalline Semiconductors, Nara, Japan. Oral presentation: *Work function measurements on transparent conductive oxides for thin film solar cells*, (2011).

2 XXVII Trobades científiques de la mediterrània. Renewable energies and energy storage, Maó, Menorca. Oral presentation: *Zn-In-Sn-O Transparent conductive oxides and its application to organic solar cells*, (2011).

3 3rd International symposium on transparent conducting materials, Analiplsi, Hersonissos, Crete, Greece. Oral presentation: *Electrical and optical properties of Zn-In-Sn-O amorphous transparent conducting thin films*, (2010).

4 23rd International Conference on Amorphous and Nanocrystalline Semiconductors, Utrecht, The Netherlands. Poster presentation: *Transparent conducting thin films by the co-sputtering of ZnO-ITO targets*, (2009).

5 E-MRS Spring meeting, Strasburg, France. Poster presentation: *Optimization of ZnO:Al layers for the back reflector application in Si thin film solar cells*, (2009).

6 E-MRS Spring meeting, Strasburg, France. Poster presentation: *Influence of RF power on the properties of sputtered ZnO:Al thin films*, (2009).

7 5th International Conference on HWCVD (Cat-CVD), Cambridge (MA), USA. Poster presentation: *Optimization of KOH etching process to obtain textured substrates suitable for heterojunction solar cells fabricated by HWCVD*, (2008).

Other Publications

1 P. Carreras, and J. M. Vidal Hernández, *El gabinet de física del Seminari Conciliar de Menorca* Institut Menorquí d´Estudis, Maó, ISBN: 9788495718846, p.119, 2010.

Acknowledgements

Aquesta tesi és el resultat de quatre anys llargs de treball i no hauria estat possible sense l'ajut i el suport que m'han donat totes les persones que enumero.

En primer lloc voldria donar les gràcies al Dr. Joan Bertomeu per haver-me donat la oportunitat de fer el doctorat sota la seva supervisió. He d'agrair molt sincerament la seva confiança, la disponibilitat i el suport que m'ha donat en tot moment. Vull fer també extensius els agraïments als dos directors del departament durant aquests anys i a la resta dels professors de Física Aplicada i Òptica.

I would also like to thank Dr. Aldrin Antony for supervising my thesis and showing me how to operate on the equipment used throughout this thesis. I also want to acknowledge him all the time he spent on corrections.

Voldria donar les gràcies a la Delfina Muñoz i al Jordi Escarré per haver-me iniciat al mon de la recerca i per haver-se llegit la meva tesi tant curosament i a la Marta Fonrodona pels consells i per les valuoses correccions que m'ha fet. També vull donar les gràcies als altres dos membres del tribunal, al Julio Cárabe i a l'Arturo Lousa. Sobretot a aquest darrer per tot el temps que ha invertit en ajudar-me a entendre moltes coses al llarg de la tesi.

També vull donar les gràcies a tots els meus companys de grup i de departament. Tots ells m'han recolzat en moments complicats i m'han donat una mà sempre que ho he necessitat. Especialment als meus grans companys de cafè i dinar per haver compartit tants moments bons i tantes converses memorables. A la meva estimada companya de despatx Martins, a l'Oriol, Jofre, Luigi (bambi!), Álvaro, Rubén, Leyre i Paolo. També a totes aquelles persones que en un moment o altre han passat pel grup o pel departament com el Dani, Fredy, Sílvia, Sarina, Thomas, Fatiha...

Aquesta feina no hagués estat possible sense la col·laboració de l'equip de secretaria, Dolors, Maite, Teresa i Jordi, que sempre han estat a punt per donar-me una mà, ni tampoc sense tot el personal dels Serveis Científico-

Tècnics de la UB. En especial voldria agrair la disponibilitat del Lorenzo Calvo de XPS i del Xavier Alcobé de XRD.

Part of this thesis was developed at the University of South Florida under the supervision of Dr. Rudy Schlaf to whom I am sincerely grateful. Thanks to him I got the opportunity to learn a lot. My colleges working there at that time made me feel like at home. I would like to specially acknowledge Sebastian, Gregor, Daniel, Jan, Wenfeng and all the colleges I met there.

I would also like to acknowledge Jürgen Hüpkes for giving me the opportunity to join the TCO group at the Forschungszentrum Jülich for a research internship. He arranged my arrival, supervised my work, and gave me worthwhile advice and support during my stay at the IEK5. I would also like to specially thank my colleagues at IEK5 Nicolas and Ting for their constant help during my experiments. Also to Marek, Etienne, Hilde, Oliver, Markus, Tsevelina, Joachim, Jan-Philip, Max, Juraj and many others for their enormous help and valuable discussion during my stay. All of them made a wonderful and very kind atmosphere.

I would also like to thank all the colleagues I have met at conferences and workshops. We did an awesome networking!! They have been a valuable support and I had the opportunity to learn a lot from them: Jan Willem, Jerôme, Laura, Ben, Ellie, Michael..

També vull donar les gràcies a totes les persones que m'han acompanyat i recolzat durant aquest període fora de la Universitat. Especialment a tot l'equip Fdez-Hidalgo (Jorge, Claudia i les seves ballarines!) per les infinites hores boníssimes que m'han fet passar, a la Muñiz, Adri, Anna B, Meri, Sofia, Elisa, Yola (mi coach!), Anna R, Alba, Alicia, Txell... A tots els companys de pis de Muntaner per aguantar-me en els moments més baixos (especialment a l'Anna, Eli, Andreu i Andratx), als meus amics i amigues de Física (Xexi, Marta, Núr, Cris, Miquel...), a les meves amigues menorquines i en especial a n'Aina, dissenyadora de la portada. Vull aprofitar per agrair molt especialment el suport incondicional i els consells que m'han donat es meus pares, germans, cunyats, nebodes i en Paco. Sou tots uns amors!

Per últim, voldria dedicar aquesta tesi a en Josep Miquel Vidal Hernández, que de ben segur estaria molt orgullós de veure-la acabada. Moltes gràcies per tot.